POLITECNICO DI MILANO

Scuola di ingegneria Industriale e dell'Informazione

Corso di Laurea Magistrale in Ingegneria Chimica

POLITECNICO
MILANO 1863

On the intensification of heat transfer in Fischer-Tropsch tubular reactors through the adoption of packed-metal foams

Relatore: Prof. Enrico Tronconi

Co-relatori: Dr. Ing. Laura Fratalocchi, PhD

Prof. Gianpiero Groppi

Prof. Luca Lietti

Prof. Carlo Giorgio Visconti

Tesi di Laurea Magistrale di:

Matteo Bramini Matr. n. 863363

Anno Accademico 2016/2017

Acknowledgment

The project leading to this Thesis has received funding from the European Research Council under Grant Agreement no. 694910 (INTENT).

Index

Preface

In a worldwide scenario characterized by a constant increase in energy demand, the interest in XtL (X to Liquids) processes is considerably growing. These processes convert natural gas (GtL), coal (CtL) or biomasses (BtL) into high molecular weight hydrocarbons

The Fischer–Tropsch synthesis (FTS) is the key technology in providing synthetic hydrocarbon fuels and chemicals from coal, natural gas, and biomass. Virtually, any source of (hydro)carbon feedstock can be converted into a mixture of synthesis gas (CO and H_2). The FTS is the reaction from synthesis gas to predominantly straight-chain hydrocarbons, such as paraffins (from CH_4 to waxes, C_nH_{2n+2} with n=1,…,100), olefins (from ethylene to longer molecules, C_nH_{2n} with n>2)).

The low temperature Fischer-Tropsch (LTFT) synthesis is the key technology of the GtL processes and is the subject of this thesis. GtL fuels offer significant environmental benefits over the fuels derived from crude oil. In fact, they are free of nitrogen, sulphur, aromatics and metals. This low-emission, premium-grade fuel can be used either “pure” or as a fuel additive in diesel engines. Furthermore, GtL diesel can be used in existing vehicles and fuel delivery systems without modifications. GtL fuels have boosted performances (high cetane number).

The low-temperature Fischer-Tropsch synthesis is a strongly exothermic process wherein the temperature control is a crucial issue. In this thesis work, we demonstrate experimentally the adoption of a Fischer-Tropsch tubular reactor loaded with a highly conductive open-cell Al foam packed with catalysts pellets to enhance heat exchange. Accordingly, the performances of a highly active $Co/Pt/Al_2O_3$ catalyst packed into the metallic structure are assessed at process conditions relevant to industrial Fischer-Tropsch operation and compared with those obtained in a conventional randomly packed fixed-bed reactor. The structured catalyst reaches

outstanding performances (CO conversion > 65%) with a remarkable temperature control. Indeed, almost flat axial temperature profiles are found along the catalytic bed even under the most severe process conditions (i.e., high CO conversions ≈ high reaction duties), showing the excellent ability of this reactor concept to manage the strong exothermicity of the reaction. In contrast, when the same experiment is carried out over the same Co/Pt/Al2O3 catalyst just randomly packed in the reactor, an abrupt increase of the catalyst temperature occurs already at low temperature, eventually leading to thermal runaway. The results herein collected prove the potential of metal foams as enhanced catalyst supports for the intensification of strongly exothermic processes in nonadiabatic tubular reactor. Furthermore, the effectiveness of the "packed-foam" configuration also demonstrates the possibility to overcome the inherently limited catalyst inventory of the washcoated conductive structured reactors proposed so far, thus boosting the productivity per reactor volume.

This manuscript is divided into six chapters:

- Chapter 1: A brief introduction to the world energy scenario is presented, followed by a general overview of the Gas to Liquids process.
- Chapter 2: It deals with the description of the FT process in its fundamental aspects: reaction mechanisms, catalysts selection and reactor technology. A further study is dedicated to the distribution of the FT products.
- Chapter 3: An accurate description of the continuously operating laboratory plant used to conduct the experimental tests described in this work is presented. Furthermore, all the procedures used for the management of the plant and the methods for analyzing the reaction products are described.
- Chapter 4: A brief overview of the catalyst preparation and its characterization is discussed here. The packed-foam reactors and the packed-bed reactor are described in detail, as well as the catalytic tests. Eventually, the obtained results are discussed.

Chapter 1

Introduction

1.1 Energy scenario

Until the last decades of the XIX century, coal used to be the most important worldwide source of energy. It was used for both domestic and industrial purposes and as a fuel for the civil and military industry.

From the beginning of the XX century, oil has gradually replaced coal as the primary source of energy. Expansion and development in the transportation sector combined with industrial growth and increasing urbanization have created the need for an energy source characterized by a high specific energy content and a better environmental compatibility with respect to coal: liquid fuels. Today approximately 85% of the energy demand still comes from fossil fuels.

Due to multiple factors such as technological progress, population growth and middle-class expansion, energy demand is expected to significantly increase in the coming years thus creating more issues related to sources, efficiency and delivery of energy. Furthermore, this century has seen tremendous advances in energy technology, including those that unlocked North America's vast resources of unconventional oil and gas, thereby ushering an era of energy abundance and diversity. Along with these matters, other issues regard the environmental problems, with CO_2 emissions that will probably peak around 2030.

Therefore, how to provide additional energy and to deliver it in a global market with both economic and environmental sustainability is one of the most crucial challenges of this century. Since a lot of this depends on scientific development and technological skills as well as social and political matters, it is a question of interest for everyone on this planet.

In order to have better knowledge of the energy challenge, it is essential to understand ongoing scenarios and to predict, as closely as possible, future trends with an outlook on the next decades.

The period going from now to 2040 is expected to reflect a dramatic expansion of the world's population and the global middle class. Improvement in living conditions will give millions of people access to electricity and global demand is expected to rise by 25%: an equivalent increase to the total energy used in North America and Latin America today. It would have been far higher (exceeding 110%) if we had not foreseen significant improvements in energy efficiency across all sectors. Demand growth is expected to increase by 45 % in non-OECD (Office of Economic Cooperation and Development) countries while demand in OECD countries will remain essentially the same [1]. As growth is strongly asymmetric, it implies considerable changes in market structure as well as in international policies.

By 2040 world population is expected to increase up to 9 billion and global GDP (Gross Domestic Product) more than double. Furthermore, in most regions, those aged under-14 will decrease in number due to declining birth rates and the over- 65 population will increase, due to a rise in life expectancy. To keep pace with demand, the world will need to pursue all economic energy sources due to new technologies that will require policies to promote innovation, investment and free commerce [2].

The most important sectors in terms of energy demand are transportation, residential/commercial and industrial. Global energy demand for transportation is forecast to increase by about 30% from 2014 to 2040, essentially due to the contribution of non-OECD

countries. Nowadays, there are about 1 billion light-duty vehicles (LDV) in the world, expected to rise to 1.8 billion in the next 25 years, with about 90% of this growth outside the 32 OECD countries. As a result of improved fuel economy, the energy demand for LDVs is expected to peak around 2020 and then decline to nearly 10% in the following 20 years along with the increase of hybrid car market share [2].

Even with an increase in efficiency, combined demand of residential and commercial energy is expected to rise by nearly 25% from 2014 to 2040. A high rise of households in Asia and other developing regions will drive such demand and, as incomes increase, so will the purchase of appliances and air conditioners. For instance, while in 1985 one out of fifty Chinese homes had refrigerators, today more than 80% do.

Globally, industrial activity accounts for 30% of primary energy and 50% of electricity demand and it is forecast to rise mostly in two sectors: heavy industry and chemicals, due to rising standards in developing countries. In particular, the production of chemicals is the fastest growing use of energy in the industrial sector.

Oil, natural gas and coal are expected to cover almost 80% of the world's energy demand throughout the next 25 years due to their reliability, affordability, versatility, transportability and due to their capability of providing a lot of energy with a relatively low volume. Among them, oil will remain the most used fuel with gas moving into second place ahead of coal. The latter, currently the second-largest fossil fuel resource, is expected to see global demand peak around 2025 and then begin to decline, owing to improved energy efficiency and environmental sustainability in the power generation sector and a switch to fuels with lower CO2 emissions. By 2040, coal will account for 20% of the global energy demand, down from about 25% in 2014. Natural gas, on the other hand, is expected to rise to 50% and meet around 40% of the global demand in the same period [2].

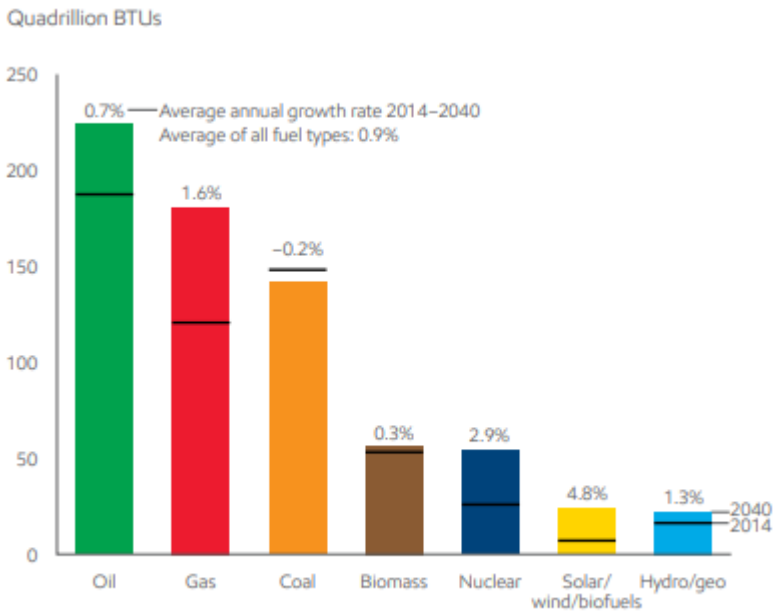

Figure 1.1: Global fuel demand in 2040 – projections [2]

Nuclear energy is a pillar of the electricity production in many countries and accounts for about 10% of today's world electricity. As nuclear plants provide electricity with low CO_2 emissions and expanding nuclear capacity would enable nations to diversify their energy supplies, the nuclear sector will see strong gains in the coming decades. The figures have more than doubled since 2014 with China accounting for nearly half of this growth. Modern renewable energy sources - wind, solar and biofuels – are also growing rapidly and will more than triple from now to 2040. The largest volume growth will come from wind, which by 2040 is expected to supply about 2% of the world's energy and around 10% of electricity. Together nuclear and renewables are likely to account for almost 40% of the growth in the global energy demand up to 2025 [2].

1.1.1 Oil

Oil is composed of a very complex mixture of various hydrocarbons, with some traces of oxygenated compounds and sulphur substances. As shown in Figure 1.2, global proved oil reserves in 2017 increased by 15 billion barrels (0.9%) to 1707 billion barrels, which would be sufficient to meet 50.6 years of global production at 2016 levels. The increase came largely from Iraq (10 billion barrels) and Russia (7 billion barrels), with small declines (<1 billion barrels) spread across a number of countries and regions. OPEC countries currently hold 71.5% of global proved reserves. [3].

World oil production grew by only 0.4 million b/d in 2016, the slowest growth since 2013. Production in the Middle East is increased by 1.7 million b/d, driven by Iran, Iraq and Saudi Arabia, but this was largely offset by declines in North America, Africa, Asia Pacific and South & Central America. Global oil consumption growth averaged 1.6 million b/d, above the 10-year average of 1 million b/d for the second successive year as a result of stronger growth in the OECD. However, China (400,000 b/d) and India (330,000 b/d) still provided the largest contributions to growth (Figure 1.2).

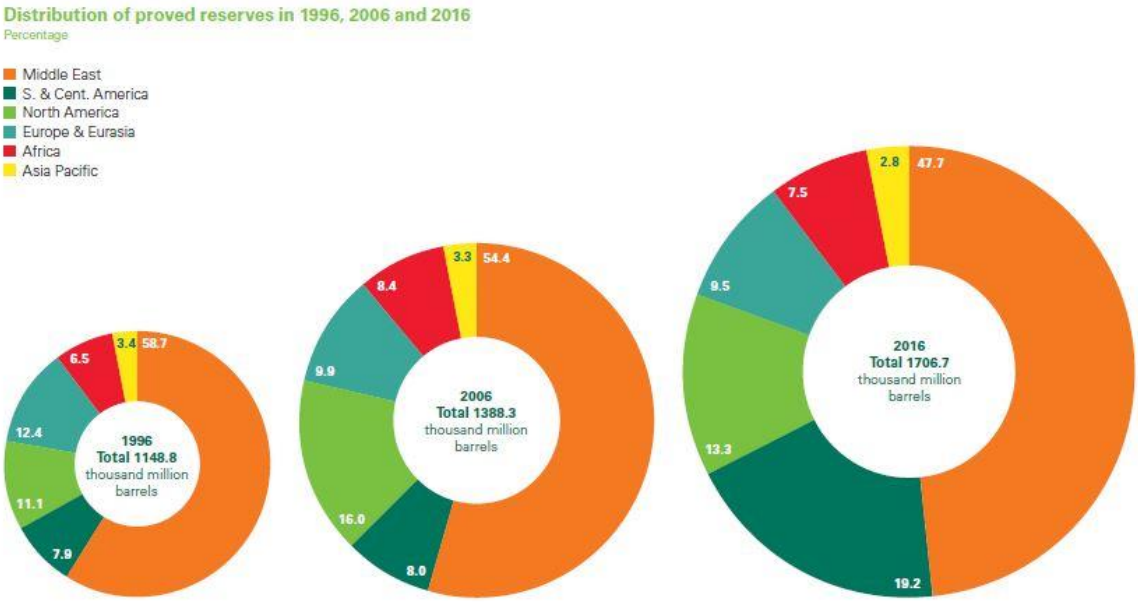

Figure 1.2: Worldwide distribution of oil reserves [3].

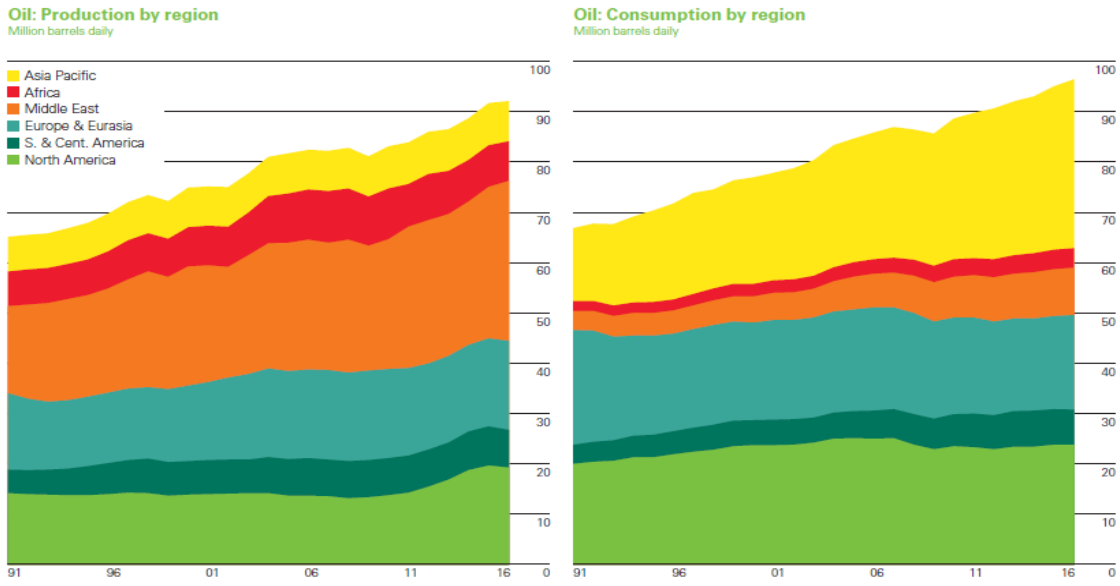

Figure 1.3: Worldwide oil production vs consumption [3].

1.1.2 Coal

Coal is a fossil fuel extracted from the earth in underground or open-cast mines; it is a ready-to-use fuel, formed by sedimentary rocks, black or dark brown, which has the property of combining with atmospheric oxygen and developing a strongly exothermic reaction. It is composed of more than 50% of carbonaceous materials (including some compounds). Coal is the result of the carbonization of plant remains that have been compressed, hardened, chemically altered and transformed, by heat and pressure, during geological times. In practice, carbonization occurs by transforming the original organic substances (wood or other plants) according to a process that is initially microbiological and which then continues, over millennia, through complex transformations with the decisive intervention of physical factors, such as pressure and the temperature, in the absence of the oxidizing action of the air.

There are many types of fossil coal, characterized by particular physical and chemical properties, which are of great importance for their practical use. The best known are peat, lignite, litantrace (the "coal" par excellence) and anthracite (the most qualitatively valuable variety). Fossil coal has been used since ancient times as a fuel. Numerous archaeological evidence testifies its use since the Bronze Age, but it has been since the nineteenth century that its large-scale exploitation gave a decisive acceleration to industrial progress. Exploration techniques are based on the drilling of soil samples at various depths and their subsequent analysis. Extraction, on the other hand, can be carried out in open-cast mines by means of giant excavators, if the carboniferous strand is only a few meters deep underground; or in underground mines, operating with special augers, if the reservoir is located at greater depths.

World proved coal reserves are currently sufficient to meet 153 years of global production, roughly three times the R/P ratio for oil and gas (Figure 1.4). By region, Asia Pacific holds the most proved reserves (46.5% of total), with China accounting for 21.4% of the global total. The US remains the largest reserve holder (22.1% of total) [3].

World coal production fell by 6.2%, or 231 million tonnes of oil equivalent (mtoe) in 2016, the largest decline on record (Figure 1.5). China's production fell by 7.9% or 140 mtoe – also a record decline – while US production fell by 19% or 85 mtoe. Global coal consumption fell by 1.7%, the second successive decline. The largest decreases were seen in the US (-33 mtoe, an 8.8% fall), China (-26 mtoe, -1.6%) and the United Kingdom (-12 mtoe, -52.5%).

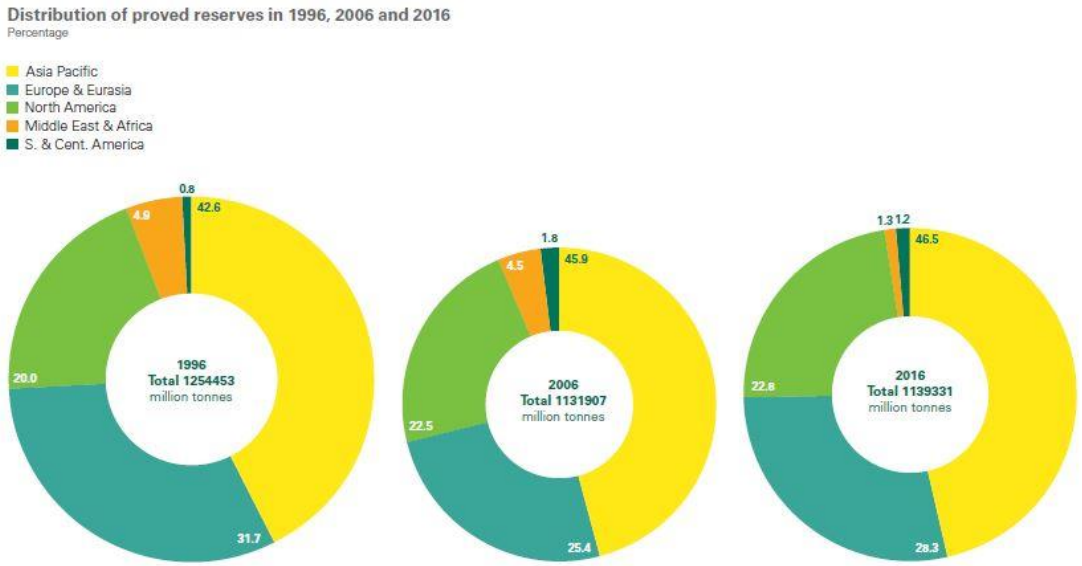

Figure 1.4: Worldwide distribution of Coal reserves [3].

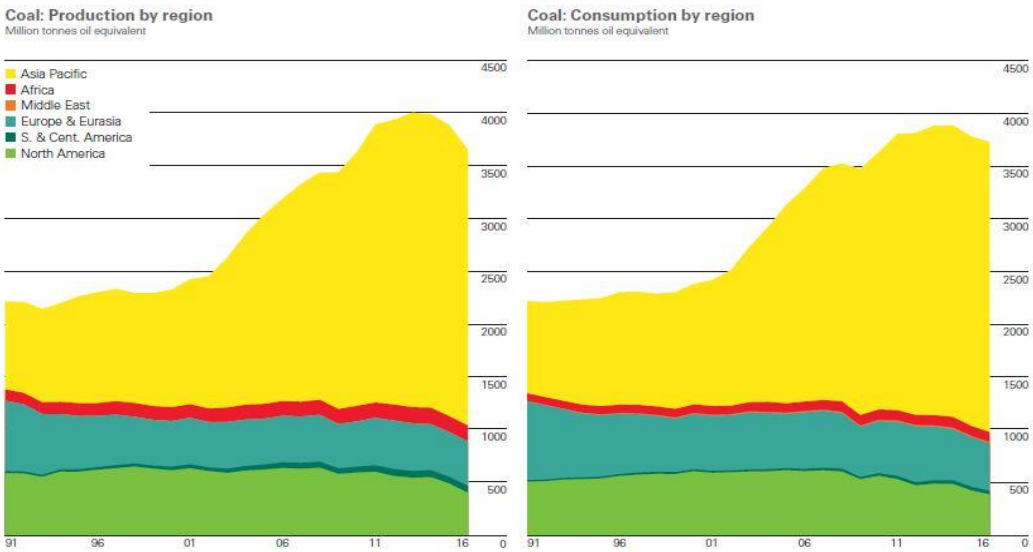

Figure 1.5: Worldwide Coal production vs consumption [3].

The advantages of coal appear to have taken a decisive break from the past. At the heart of this shift are structural, long-term, factors: the increasing availability and competitiveness of natural gas and renewable energy; combined with mounting government and societal pressure to shift away from coal towards cleaner, lower-carbon fuels. These long-term forces in turn have given rise to policy responses that have often added even greater momentum.

This was particularly the case in China in the last year, which, at the beginning of 2016, introduced a series of measures to reduce the scale of excess capacity in the domestic coal sector and improve the productivity and profitability of the remaining mines. These measures were focused on reducing capacity amongst the smallest, least productive mines and encouraging greater consolidation. In addition, the government further constrained production by restricting coal mines to operate for a maximum of 276 days, down from 330 days.

A particularly extreme example of this long-run movement away from coal was seen in the UK, where the rise in global coal prices added to the pressure from the recent increase in the UK's Carbon Price Floor. As a result, the UK's relationship with coal almost completed an entire cycle: with the UK's last three underground coal mines closing, consumption falling back to where it was almost 200 years ago around the time of Industrial Revolution, and the UK power sector recording its first-ever coal-free day in April of this year [3].

1.1.3 Natural Gas

Natural gas is a naturally occurring hydrocarbon gas mixture consisting primarily of methane, but commonly including varying amounts of other higher alkanes, and sometimes a small percentage of carbon dioxide, nitrogen, hydrogen sulfide, or helium. It is formed when layers of decomposing plant and animal matter are exposed to intense heat and pressure under the surface of the Earth over millions of years. Natural gas is found in deep underground rock formations or associated with other hydrocarbon reservoirs in coal beds and as methane

clathrates. Natural gas is also found in submarine reservoirs; its extraction therefore requires drilling, carried out with special drills capable of descending at high depths. From production to consumption, natural gas travels through methane pipelines or tankers, with transport costs that often have a significant impact on the final price.

Natural gas is one of the most important energy sources, sharing with the oil products various possibilities of use. It is widely used, in fact, as fuel for the generation of electricity, for space heating or as fuel for motor vehicles. Currently, just under 25% of the world's primary energy demand depends by natural gas, which, according to experts, is also the primary energy source destined to have the greatest growth in the coming decades.

Global proved gas reserves in 2017 is increased by 1.2 trillion cubic metres (tcm) or 0.6% to 186.6 tcm. As oil, this is sufficient to meet more than 50 years of current production (52.5 years). Myanmar (+0.7 tcm) and China (+0.6 tcm) were the main contributors to growth. By region, the Middle East hold the largest proved reserves (79.4 tcm, 42.5% of the global total). Iran is the largest reserve holder (33.5 tcm, 18% of total) (Figure 1.6).

Global natural gas production is increased by only 0.3%, or 21 billion cubic metres (bcm) to 3552 bcm. Declining production in North America (-21 bcm) partially offset the strong growth in Australia (19 bcm) and Iran (13 bcm). Gas consumption increased by 63 bcm or 1.5% – slower than the 10-year average (2.3%). EU gas consumption rose sharply by 30 bcm, or 7.1% – the fastest growth since 2010. Russia saw the largest drop in consumption of any country (-12 bcm).

Nearly half of the growth in global gas demand through 2040 is expected to be met through interregional trade, most using LNG (Liquefied Natural Gas) technology (Figure 1.7). Until the first LNG shipping and receiving terminals opened in 1964, inter-regional gas trading was confined to areas connected by pipeline. With LNG technology, natural gas can be super-cooled to liquid and safely shipped via tanker to receiving terminals anywhere in the world.

LNG exports are expected to triple in the next years and most of which will go to competitive markets in Asia Pacific, followed by United States, East Africa and Australia. Today, around 70% of NG consumption is delivered through pipelines operating at pressures around 80 [MPa] and flow rates of 106 [Nm3 h-1]; shipping becomes convenient when distances make the pipeline costs higher than that of liquefaction, transportation and regasification.

One further solution to the problem of complete exploitation of NG resources and related transportation is the so-called GTL (Gas-to-Liquids) technology. Particularly suitable for small gas reserves, GTL consists of a chemical liquefaction of natural gas which significantly upgrades the economic value of the latter and eases its access to the transportation fuels market. Additionally, it could mitigate some environmental concerns by displacing higher-sulfur fuels, obtained from crude

oil, with essentially sulfur-free fuels. Additionally, GTL technology could allow refineries to convert some of their gaseous waste products (flare gas) into valuable transportation fuels and lubricants.

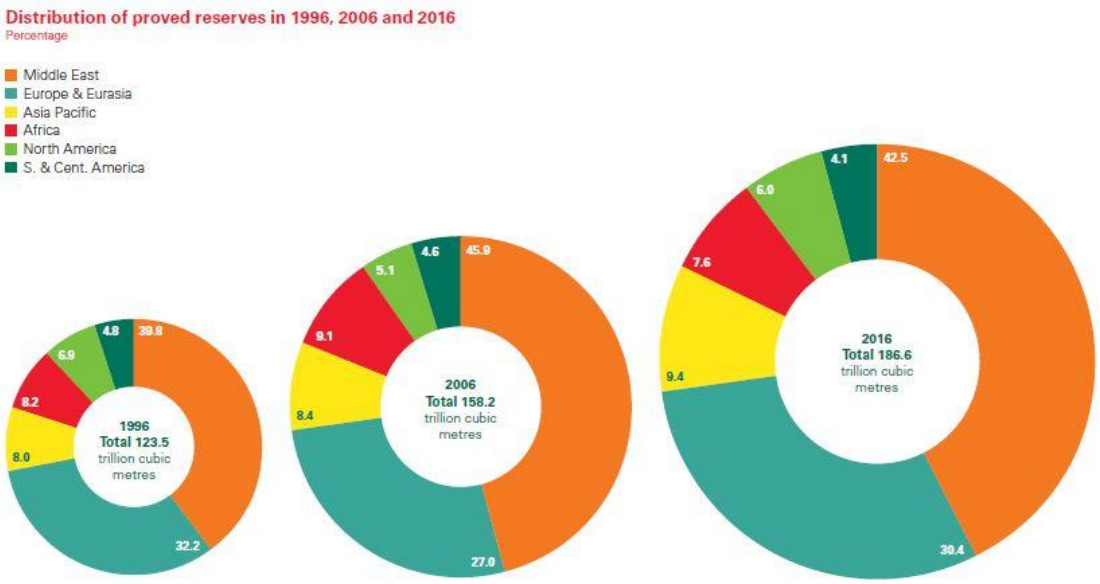

Figure 1.6: Worldwide distribution of Natural gas reserves [3].

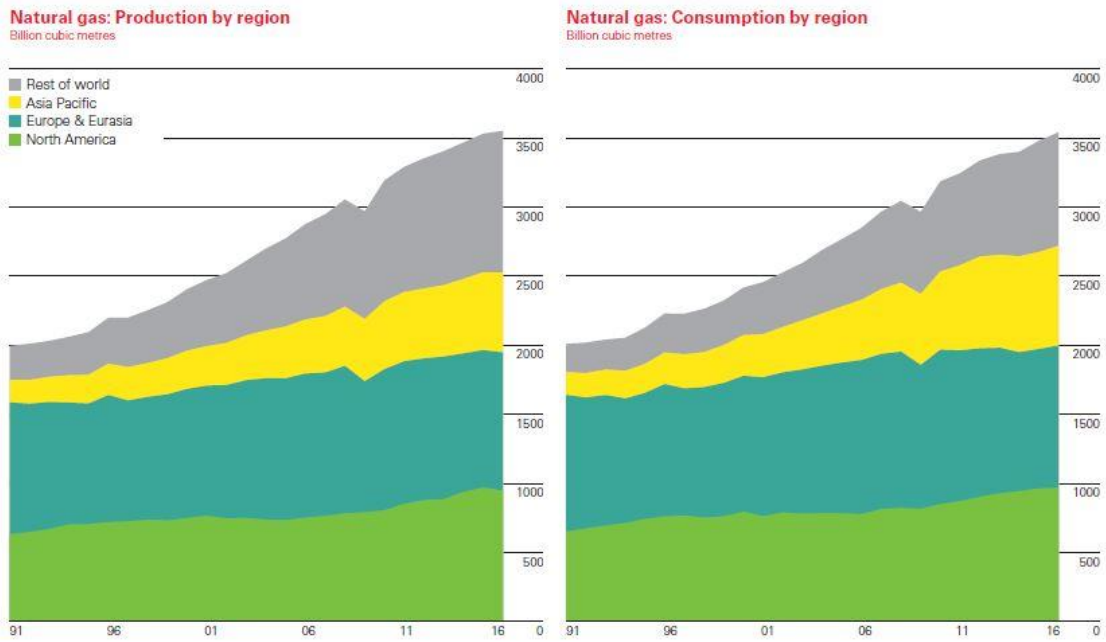

Figure 1.7: Worldwide NG production vs consumption [3].

1.2 Gas-To-Liquid technology

The interest in the gas-to-liquids technology is not only a result of the abundant supply of natural gas, but also of a market demand for cleaner fuels. In this regard, the GtL fuels offer significant environmental benefits over the fuels derived from crude oil. In fact, they are free of nitrogen, sulphur, aromatics and metals. This low-emission, premium-grade fuel can be used either “pure” or as a fuel additive in diesel engines. Furthermore, GtL diesel can be used in existing vehicles and fuel delivery systems without modifications.

There are three technologies for converting natural gas into liquid products: the "gas-to-methanol" process, the "gas-to-dimethyl ether" process and the "gas-to-hydrocarbons" technology.

Concerning the conversion of natural gas into methanol, beyond its use as raw material for the organic chemical industry, methanol is part of the family of automotive fuels with reduced environmental impact. In fact, like all oxygenated fuels, methanol also guarantees a high environmental friendliness thanks to the greater efficiency of combustion ensured by the presence of oxygen inside the molecule. The diffusion of methanol as a propellant for motor vehicles, however, has a limit linked to its toxicity and its low calorific value compared to diesel and petrol.

From this point of view, the dimethyl ether (DME) seems to be also an excellent candidate, given the reduced toxicity and the versatility of its uses. It could be used as fuel in power stations for combined cycle gas turbines, as a substitute / complement for LPG for domestic use (given the similar volatility of LPG and DME), as automotive fuel for diesel engines (high number of cetane) or, finally, also as a hydrogen carrier in fuel cells.

Nonetheless, to date the way that seems easier to produce excellent fuels for motor vehicles and chemicals, is constituted by the "gas-to-hydrocarbons" process. It provides the conversion of gas through three consecutive steps (see figure 1.8):

1. Production of synthesis gas (mixture H_2 / CO)
2. The synthesis of Fischer-Tropsch;
3. Hydrocracking / upgrading of heavy products.

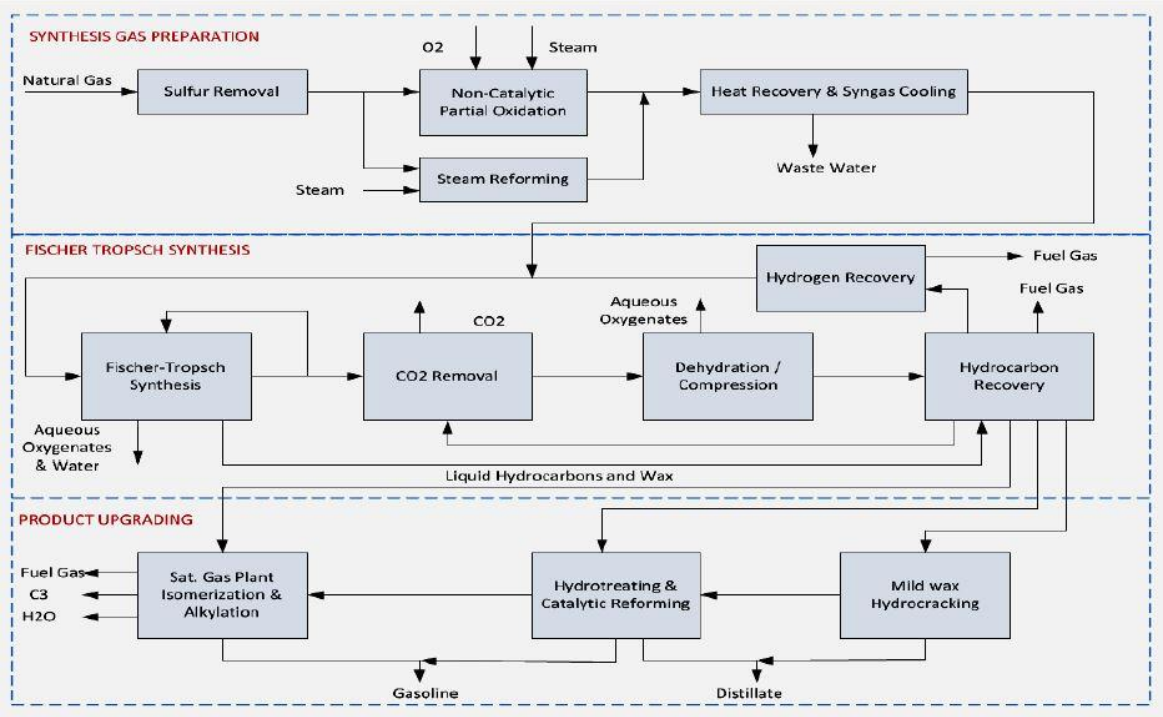

Figure 1.8: Stages of the gas-to-hydrocarbons conversion process.

1.2.1 Synthesis gas production

Syngas can be produced from many sources, including natural gas, coal, biomass, or virtually any hydrocarbon feedstock, by reaction with steam or oxygen. Syngas is a crucial intermediate resource for production of hydrogen, ammonia, methanol, and synthetic hydrocarbon fuels.

The formation of syngas is strongly endothermic and requires high temperatures. Steam reforming of natural gas (or shale gas) proceeds in tubular reactors that are heated externally. The process uses nickel catalyst on a special support that is resistant against the harsh process conditions. Waste heat from the oven section is used to preheat gases and to produce steam. This plant generates syngas with H_2/CO ratios in the range of 3-4, and is suitable for hydrogen production.

Partial oxidation of methane (or hydrocarbons) is a non-catalytic, large-scale process to make syngas and yields syngas with H2/CO ratio of about 2. This is an optimal ratio for gas-to-

liquids plants. A catalytic version of partial oxidation (CPO), based on short-contact time conversion of methane, hydrocarbons or biomass on e.g. rhodium catalysts, is suitable for small-scale applications.

Autothermal reforming (ATR) is a hybrid, which combines methane steam reforming and oxidation in one process. The heat needed for reforming is generated inside the reactor by oxidation of the feed gas. As POX, ATR is also suitable for large-scale production of syngas for gas-to-liquids or large-scale methanol synthesis processes.

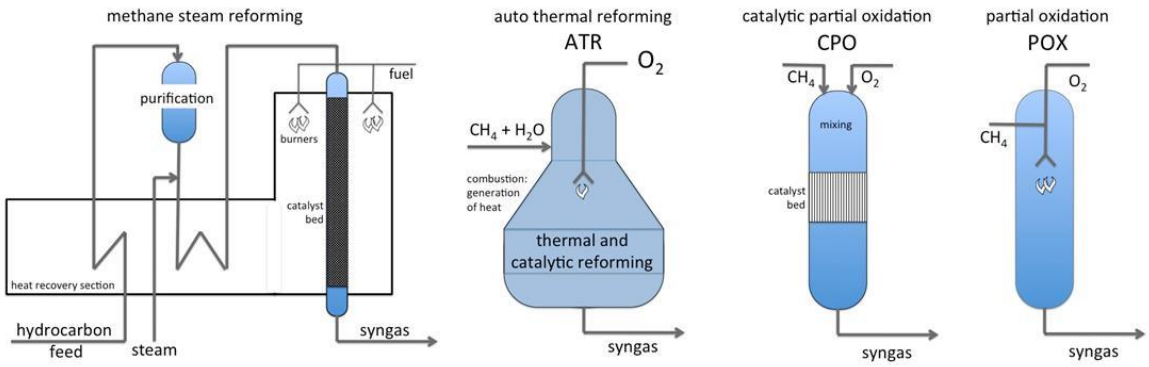

Figure 1.9: Reactors and process layout for syngas production from natural gas and shale gas.

1.2.2 The Fischer-Tropsch synthesis

The Fischer-Tropsch Synthesis (FTS) converts syngas into hydrocarbons which form the basis for gasoline, diesel, jet fuel, and chemicals such as olefins and waxes. It forms the heart of the Gas-to-Liquids (GTL) and Coal-to-Liquids (CTL) plants in South Africa, Qatar, Malaysia and China. The product distribution is broader than liquids hydrocarbons alone, and includes methane and alkanes, C_nH_{2n+2} (with n from 1 → 100), alkenes or olefins (C_nH_{2n}; $n \geq 2$), and to a lesser extent oxygenated products such as alcohols. Catalysts for the Fischer-

Tropsch Synthesis are either based on cobalt or the much cheaper iron. The FTS is the subject of this thesis work and it will be described in detail in Chapter 2.

1.2.3 Products upgrading

A hydrocracker is the mainly catalytic process needed to convert heavy FT reactor products into distillate fuels. FT wax is an ideal feed to hydrocrack because it is extremely paraffinic. An FT wax hydrocracker operates at less than half the pressure, twice the space velocity, requires about one-third the hydrogen, and displays better catalytic stability compared to hydrocracking petroleum vacuum gas oil (VGO). A FT wax hydrocracker has a lower estimated erected cost (EEC) than a petroleum VGO hydrocracker, primarily due to the lower pressure, higher space velocity operation.

It is easier to convert FT wax into distillate fuels than to convert FT naphtha into gasoline. A typical petroleum refinery converts raw naphtha into gasoline using two catalytic processes in series, hydrotreating and reforming. SASOL uses the same sequence to upgrade FT naphtha into high-octane gasoline. Raw FT naphtha is more olefinic, has fewer ring compounds (naphthenes and aromatics), and has more oxygenates than a petroleum naphtha. Removal of sulfur and nitrogen compounds is of primary importance with petroleum naphthas, whereas FT naphtha is virtually sulfur and nitrogen free.

Despite the absence of sulfur and nitrogen, hydrotreating FT naphtha is still challenging. Oxygenates and olefins deactivate reforming catalyst, so they must be removed by the hydrotreater. Oxygenate removal requires temperatures and pressures that would polymerize olefins and rapidly coke-up the hydrotreating catalyst. Therefore, the hydrotreater design must accommodate the saturation of olefins at low temperature and then convert oxygenates at higher temperature, after the olefin content is reduced. The hydrotreated FT naphtha is even

more paraffinic than the raw naphtha because olefins and oxygenates are converted to paraffins.

The paraffinic nature of FT products is an advantage for the hydrocracker, but a disadvantage for the reformer. Reformers are designed to maximize aromatics yield, and this objective becomes increasingly difficult as the paraffinicity of the naphtha increases. The lean naphtha by petroleum standards is a rich naphtha by FT standards. Compared to traditional reforming pressure (860 kPa or greater), low pressure reforming (345 kPa) can greatly increase the liquid product yield for a paraffinic feedstock. However, the fact remains that upgrading FT naphtha into high-octane gasoline presents a greater technological challenge (higher costs) than converting heavy FT products into distillate fuels.

As shown in Table 1.1, the characteristics of the "GtL" diesel are better that obtained from oil, due to the higher performances in diesel-cycle engines (high cetane number) and for the reduced environmental impact (low levels of aromatics and sulfur in the exhaust fumes). Figure 1.10 shows the products obtained from the oil barrel according to an average refinery processing scheme (a) and the composition of an equal volume (barrel) of products obtainable with the Fischer-Tropsch process (b).

Table 1.1: Characteristics of a refinery diesel and a GtL [19].

Characteristic	**Refinery Diesel**	**GtL Diesel**
Cetane number	51 (min)	>70
Sulphur (ppm)	50 (max)	<10
Aromatics (vol.%)	Not established	0
Relative density to H_2O	0,815 – 0,875	0,77 – 0,80

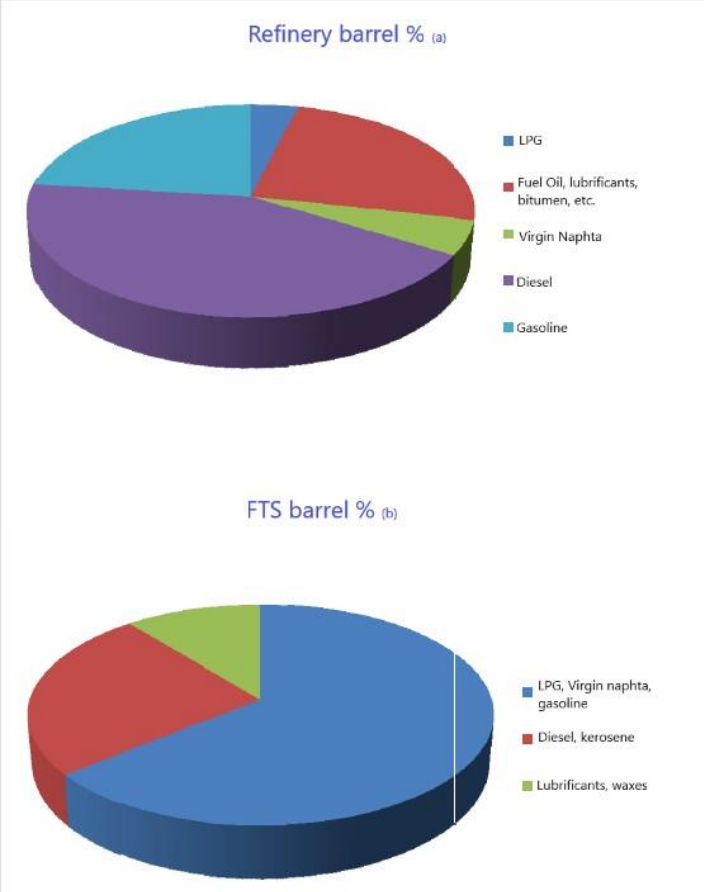

Figure 1.10: Products composition from Refinery vs FTS.

1.3 References

[1] Organization for Economic Co-operation and Development - Wikipedia, the free encyclopedia.

[2] Exxon Mobil, The 2016 outlook for energy: a view to 2040, 2016.

[3] BP Statistical Review of World Energy 2017.

Chapter 2

Reactors and catalytic aspects of the Fischer-Tropsch synthesis

2.1 Introduction

This chapter introduces the Fischer-Tropsch synthesis as a catalytic process, analyzing its state of the art and showing its historical evolution. To this end, the catalyst usually used, the FT reaction mechanism and the distribution of the FT products, as well as the reactor currently adopted at the industrial scale will be described.

2.2 Historical evolution

It has been more than 100 years since Sabatier and Sendersen [1] reported that methane could be formed by CO hydrogenation over nickel catalysts (1902). In 1913 and 1914 Badische Anilin and Soda Fabrik (BASF) [2] were awarded patents for the production of hydrocarbons and mainly oxygenate derivatives (Synthol) from syngas, by using alkali promoted osmium and cobalt catalysts at high pressure. In 1923, Franz Fischer and Hans Tropsch [3] synthetized a product similar to Synthol over alkalized iron catalysts. Two years later, the same scientists announced the synthesis of high molecular weight hydrocarbons at atmospheric pressure over cobalt and nickel catalysts [4]. This is traditionally considered the date of birth of the Fischer-

Tropsch synthesis. However, the "modern process", i.e., the CO hydrogenation under pressure, is reported a decade later: in 1936 with cobalt-based catalyst [5], in 1937 with iron [6] and in 1938 with ruthenium [7]. In 1933, Ruhrchemie AG constructed the first FT plant using a nickel based catalyst working at atmospheric pressure. By 1938, there were nine operating FT plants in Germany using cobalt based catalysts at 10 bar. FT plants were also operated in Japan, Manchuria and France. After the Second World War, all these plants were shut down, as they were uneconomical. Two commercial plants were also built in USA during the 1950s by Carthage-Hydrocol and Fuelco. The first one operated only for two years while the latter was dismantled in 1996 after more than 40 years. In the same years (1955), the first Sasol plant (Sasol I) in South Africa came on stream and two units were added in 1980 (Sasol II) and 1982 (Sasol III), respectively. In 1991, the PetroSA (Mössgas) plant came on stream in South Africa [8].

To date, South Africa remains a world leader in FT technology, and Sasol and PetroSA operate four FT plants in the country, so that 35% of the liquid fuels consumed in the country comes from synthetic fuels. Sasol also operates the Oryx plant, which was started up in Qatar in 2007, as the result of a joint venture with Qatar Petroleum.

Another key player in the FT industry is Shell, which began developing GtL technology in the 1970s. Shell operates FT plants in Malaysia (Bintulu GtL since 1993) and in Qatar (Pearl GtL since 2011) [8].

In September 2016, Velocys plc (VLS.L) company announced that construction of the ENVIA Energy's GtL plant in Oklahoma City was complete. The project, which is based on the compact/modular GtL technology, comes from a joint venture between Waste Management, NRG Energy, Ventech and Velocys (ENVIA Energy) [9].

2.3 Catalysts candidates for the FTS

The metals considered for FTS applications are: nickel, cobalt, iron and ruthenium. This is due to their level of activity. Depending on the application, the criteria to select the most suitable catalyst are the price of the active metal, the desired final products and the carbon source for synthesis gas production. Ruthenium is not present in commercial usage because, despite the fact it is the most active metal in the FTS, it has low availability and high cost. Due to its excessive hydrogenation activity, nickel produces too much methane for viable operations [10]. In addition, when exposed to typical FTS pressures, nickel forms volatile nickel carbonyls. This results in loss of catalyst from the reactor and deactivation. This leaves cobalt and iron as the most promising candidates for industrial operations.

Cobalt is the catalyst preferred for operations between 200 and 240°C, (Low Temperature Fischer-Tropsch synthesis, LTFT), which favors the formation of heavier hydrocarbons (e.g., waxes) that can be upgraded to the diesel and jet fuel range. For the production of gasoline and high-value α-alkenes, iron catalysts operating at temperatures between 300 and 350°C (High Temperature Fischer-Tropsch, HTFT) are deemed the best options. Iron-based catalysts have high water-gas-shift (WGS) activity. This makes them suitable for synthesis gas with low H_2/CO ratios, i.e., from coal or biomasses feedstock, where the ratio is considerably lower than the consumption ratio of the FT reaction (H_2/CO= 2.15). The WGS activity of Co-based catalysts, instead, is low. Therefore, these catalysts are used when the synthesis gas is produced from natural gas, which gives H_2/CO ratios close to the stoichiometric value of 2.15 [11].

Notably, LTFT has several advantages with respect to HTFT. In this regard, LTFT produces hydrocarbon products that are less energy intensive to upgrade and premium quality fuels with high cetane number (up to 75) related to ignition delay time in diesel engines. Furthermore, the greenhouse gas emissions are quite low (lower C_1-C_4). In contrast, HTFT to

target gasoline range fuels results in hydrocarbons with poor octane rating and, due to the lower chain growth probability factor, significantly more methane and other light gases are produced.

The LTFT synthesis carried out over cobalt based catalysts is the focus of this thesis.

2.3.1 Cobalt-based catalysts

The currently used cobalt-based catalysts are made of promoted cobalt dispersed on an oxide support, and thus similar to the ones prepared by Fischer and Tropsch. The FTS occurs on the surface cobalt metal centers (Co^0). Cobalt is an expensive material and thus it is important to obtain a suitable dispersion on the catalytic support. From the particle size, catalyst morphology, extent of reduction, and particle stability depends on the number of Co^0 surface sites [12]. After the catalyst activation step, the extent of reduction should be greater than 60%, even though the cobalt may undergo further reduction during the FTS reaction. An optimum cobalt particle size of around 8–10 nm is preferred as particles below this range have a lower turnover frequency (TOF) [12]. Furthermore, very small particles (4–6 nm) are prone to deactivation and are also difficult to reduce due to the increased metal-support interaction [12]. The two most common phases of metallic cobalt in supported cobalt FTS catalysts are face-centered cubic (fcc) and hexagonally close-packed (hcp), which often coexist. It is reported that for cobalt particles less than 40 nm, the predominant phase should be fcc [12]. The relative amounts of these phases may be influenced by the activation procedure, the addition of promoters, and the type of support used [13].

Catalysts are often promoted with a second metal (i.e., noble metals) which leads to the improvement of the reducibility of the cobalt oxide particles formed after the calcination step involved in the catalyst synthesis procedure [12]. This results in an increase in the number of

active sites available for the FTS, thus resulting in higher CO conversion per gram of catalyst compared to unpromoted catalysts. The more facile cobalt reduction is attributed to faster hydrogen activation in the presence of promoter metals and subsequent spillover of hydrogen to cobalt oxides and reduction of cobalt species [13]. Often, the promotion with noble metals plays a key role to achieve small average size of either cobalt oxide or cobalt metal particles. Structural promoters, such as Zr and La, are usually also added to improve the stability of Co.

Two are the main functions of the catalyst support: the cobalt dispersion and the production of stable cobalt metal particles in the catalysts after reduction. Mechanical strength and thermal stability to the catalyst are also provided by the support. Robustness is also an important characteristic of the support. Accordingly, resistance to attrition is required under FTS conditions, especially in a slurry bubble-column environment. The most used supports for FTS catalysts are silica, alumina and titania. These oxide supports are characterized by a high surface area. When Al_2O_3 is used, the interaction between the support and cobalt may take place. As a consequence, mixed compounds inactive in the FTS, such as cobalt-aluminate, can be formed. In contrast with titania and silica these interactions are weaker. In particular, Co-TiO_2 interactions can occur depending on the catalyst formulation [21].

Cobalt-based FT-catalysts are usually prepared via impregnation or co-precipitation. The impregnation technique is the preferred one [13]. It consists in depositing a solution containing dissolved cobalt precursor on a dry support. One impregnation procedure is the incipient wetness impregnation (IWI) method. In the IWI method the impregnating solution containing the cobalt salt, typically cobalt nitrate, is contacted with a dry porous support. After being contacted, the solution penetrates into the pores of the support by capillary action. The condition for the incipient wetness to occur is that the pores of the support are all filled with the liquid and there is no excess of moisture. Another impregnation technique used to deposit cobalt onto the support is the slurry (wet) impregnation, which uses an excess of

liquid in the pores of the supports [13]. The support is usually added to the impregnating solution heated at 60-120°C, to yield a slurry, which is constantly stirred. The slurry impregnation method is often preferred in industry over incipient wetness impregnation because the distribution of cobalt particles results more uniform at high cobalt loadings (e.g., 20-25% by weight cobalt) [14].

The co-precipitation method is predominant in the preparation of iron FT catalysts, while it is not common for cobalt-supported catalysts [13]. The catalyst preparation based on co-precipitation is performed by following four steps: precipitation, washing, drying, and shaping. Chemical precipitation of the cobalt, promoter, and support by a precipitation agent (i.e., Na_2CO_3 or KOH) can be done batchwise or continuously at constant pH. Temperature, precipitation agent, precursor salts, structure directing or organic hydrolysis reagents, aging time, and reaction atmosphere control the crystallite size and composition of the precipitate. Filtration and washing of the precipitate are made to ensure that excess chemicals are removed [12]. The last step of the co-precipitation, the shaping of the catalyst precursor, differs with the reactor application.

Drying and calcination are usually carried out after the impregnation or co-precipitation step. During these thermal treatments it is important that the cobalt distribution achieved by impregnation or precipitation is preserved. In order to do that, the cobalt mobility must be hindered. For catalysts obtained by impregnation from cobalt nitrate solutions, more attention has to be payed during the calcination process. An exact calibration of the heating rate, temperature and air flow should be made to remove the water and NO_x immediately.

2.3.2 Composition of industrial Co-based catalysts

At the industrial scale, Co-based catalysts are employed by Sasol and Shell for the Slurry Phase Distillate (SPD) process and Shell Middle Distillate Synthesis (SMDS) process. The composition of these catalysts is shown in Table 1.

The new generation Shell catalyst is supported on TiO_2 pellets, while the previous catalyst was supported on SiO_2 modified with some Zr and possibly other rare earth oxides [15-19]. Two methods are used for the preparation of the patented Shell catalysts: the kneading or incipient wetness impregnation (IWI) methods. However, the kneading is the preferred method. It consists in mixing the support with the aqueous solution containing Co-nitrate salt and in applying an intensive mechanical treatment such as pressing, squeezing or wringing, to form a paste. This paste is then dried and calcined in air at 500°C.

When the impregnation procedure is adopted, it is repeated several times until the desired Co loading is obtained. After each impregnation step, the material is dried and calcined in air at 500°C. The impregnating solution containing the cobalt precursor salt is usually aqueous. However, it is modified with the addition of "delaminating" agents, i.e., citric acid, in one example shown in the Shell patent of 2010 [18]. The inventors reported that the function of the citric acid was the improvement of the cobalt dispersion on the support.

The Sasol catalyst is said to be Pt-Co/Al_2O_3 [19-24]. Cobalt catalysts patented by Sasol are supported on alumina modified with silica. In addition to cobalt, the catalyst components include platinum as promoters. The preferred catalysts preparation method is the slurry impregnation, which involves the impregnation of the support with an excess volume of impregnating solution containing both Co and Pt-precursors. The impregnation step is repeated twice. Each impregnation step is followed by drying and calcination under a controlled air stream at maximum 250°C.

Table 2.1: Composition of commercial Co-based FT catalysts [15-24].

	Shell SMDS	***Sasol SPD***
Active metal	Co	Co
Support	TiO_2 (new), SiO_2 (old)	γ-Al_2O_3
Reduction promoter	-	Pt
Rare earth oxides	Mn (new) Zr, Ti, Cr (old)	SiO_2
Co loading	10-30g per 100g of support	10-30g per 100g of support
Reduction promoter loading	-	Pt:Co molar ratio <1:100

Numerous patents, probably more than 100 U.S and foreign patents, are also assigned to Exxon for FT Co-based catalysts formulations [25]. Most of the catalysts developed by Exxon are composed of cobalt dispersed on TiO_2 support and additives that function as structural (metal oxides) or activity (noble metals) promoters. The support contains primarily TiO_2, which, in many cases, is doped with a low content of silica or alumina.

Recently, Velocys patented a new cobalt based FT catalyst to use in structured microchannel reactor systems [26]. The catalyst is supported on silica modified with 16wt.% of TiO_2 and is comprised of 42wt.% of Co, 0.2wt.% of Re and 0.03wt.% of Pt. The preparation method refers to the patent of Oxford Catalysts Group [26] and it is based on the addition of the support in a warm solution containing: (i) the Co-nitrates precursor salt, (ii) the precursors of the promoter, (iii) a low content of water and (iv) an organic compound, such as urea, citric acid or acetic acid [26]. Then, the obtained material is heated in an oxygen-containing atmosphere to 100°C and 250°C for 5 and 3 h, respectively (heating rate of 2°C/min). In the example cited in the Velocys patent [26], the catalyst is prepared by following four impregnation steps of a solution containing Co and Re precursors. Each impregnation is

followed by drying and calcination. Citric acid is chosen among the proposed organic compounds and it is added in the impregnating solution in the last three-impregnation steps. A further impregnation step is carried out on the obtained material to deposit Pt on the catalyst [26].

2.4 Reaction mechanisms

The Fischer-Tropsch synthesis consists of a set of reactions that, starting from CO and H_2, lead to the formation of a wide spectrum of products, among which the main ones are linear paraffinic hydrocarbons. However, the formation of α-olefins, of internal olefins and oxygenated products (alcohols) is observed.

Understanding the reaction mechanism is of fundamental importance both for the development of new, more active and / or selective catalysts, and for the formulation of a reliable kinetic model that accounts for the formation of the products depending on the process conditions adopted.

There is more than one theory that attempts to explain the mechanism of the reactive species through which the reactants are converted. It is known that the synthesis proceeds through a mechanism of addition of successive monomeric carbon units, which are appropriately coordinated by the active site. The mechanism can, indeed, be simplified as a polymerization scheme.

From the point of view of the reactions scheme the system can be described by the following main reactions [27]:

$(2n + 1)\ H_2 + n\ CO \rightarrow C_nH_{2n+2} + n\ H2$ [2.1]

$2n\ H_2 + n\ CO \rightarrow C_nH_{2n} + n\ H_2O$ [2.2]

$2n\ H_2 + n\ CO \rightarrow C_nH_{2n+1}OH + (n - 1)\ H_2O$ [2.3]

which respectively describe the formation of paraffins (eq. 2.1), olefins (eq. 2.2) and linear alcohols (eq. 2.3).

Undesired secondary reactions may also occur [28], such as the water gas shift reaction (eq. 2.4), the Boudouard reaction (eq. 2.5), and the methanation reaction (eq. 2.6):

$CO + H_2O \rightarrow CO_2 + H_2$ [2.4]

$2\ CO \rightarrow CO_2 + C$ [2.5]

$CO + 3\ H_2 \rightarrow CH_4 + H_2O$ [2.6]

The reaction proceeds with the formation of the growth monomeric unit and then with successive kinetic steps listed below [29-32], thus generating a reaction heat equal to about 165 kJ/mole of CO converted.

I. Reagent adsorption

$H_2 + 2* \leftrightarrow 2\ H*$

$CO + * \leftrightarrow CO*$

II. In situ formation of the monomer

$CO* + a\ H* \rightarrow C_l* +$ oxygenated species

III. Chain initiation

$C_l* \rightarrow R_l*$

IV. Chain growth

$R_l* + C_l* \rightarrow R_{n+1}* + *$

V. Chain termination

$R_n^* \rightarrow$ product A_n^*

VI. Product desorption

product $A_n^* \rightarrow$ product $A_n + *$

VII. Product reabsorption and secondary processes:

product $A_n + * \rightarrow$ product A_n^*

product $A_n^* \rightarrow$ product B_n^*

The reaction chain begins with the dissociative adsorption of hydrogen and the molecular adsorption of carbon monoxide (I). The atomic hydrogen, together with the molecular CO, reacts to give an adsorbed monomer unit (II), generically indicated as Cl*, which evolves by successive additions to give species with a high number of carbon atoms (III-IV) . The hydrocarbon products so formed can desorb (VI) after termination of the growth reaction (V) or resorb and give secondary reactions (VII)., The paraffinic products and the olefins with carbon atoms are indicated with An and Bn, respectively, and the corresponding species adsorbed with An* and Bn*, respectively. Regarding the second stage, various theories are presented that hypothesize the formation, starting from the synthesis gas, of different monomers [30, 33]; all theories agree that the atomic hydrogen and CO (molecular or dissociated) react and cause, on the catalytic surface, the formation of a monomer with a single carbon atom (C_l*). The theories proposed in the literature diversify for the structure of the adsorbed monomeric species and thus for the structure of the growing hydrocarbon chain.

According to the **oxymethylene** theory, proposed by Eiidus [34], which follows the observation that alcohols are present in the FT products distribution, the monomeric unit is

the adsorbed hydroxycarbons (also called enol). It is formed by partial hydrogenation of carbon monoxide molecularly adsorbed on the surface, according to the following reactions:

$$CO + * \rightarrow CO* \quad [2.7]$$

$$CO* + H_2 \rightarrow HCOH* \quad [2.8]$$

Chain growth occurs by successive addition of these units (eq. 2.9), with the consequent removal of water:

$$HCOH* + R_nCOH* + H_2 \rightarrow Rn_{+1}COH* + H_2O + * \quad [2.9]$$

This mechanism can explain the formation of all the species present in the FTS products.

The theory of **direct insertion** provides the insertion of the molecule of adsorbed CO between the catalytic active site of the catalyst and the carbon atom of the adsorbed alkyl species, according to the reaction (eq. 2.10). This theory was proposed by Pichler [1] in 1970 and resumed later by Sternberg and Wender [6].

The formed RnCO* acyl group is subsequently hydrogenated to form an adsorbed hydrocarbon unit (alkyl) having an additional methylene unit, as indicated below (eq. 2.11):

$$R_n* + CO* \rightarrow R_n(CO)* + * \quad [2.10]$$

$$R_n(CO)* + 2\ H_2 \rightarrow R_{n+1}* + H_2O \quad [2.11]$$

As for the enol theory, also in the direct insertion theory it is possible to explain both the formation of hydrocarbons and oxygenated species.

The **carbide** theory was proposed in 1926 by Fischer and Tropsch and it is still largely recognized by different scientists [29-32, 35-37]. It provides the formation of the monomeric species CH_2*, according to the following reactions:

$$CO(g) + * \rightarrow CO* \quad [2.12]$$

$$CO* + * \rightarrow C* + O* \quad [2.13]$$

$$C* + H_2 \rightarrow CH_2* \quad [2.14]$$

$$O* + H_2 \rightarrow H_2O + * \quad [2.15]$$

This unit is then inserted into the growing hydrocarbons chain (eq. 2.16) forming an adsorbed hydrocarbon species containing an extra carbon atom and releasing an active site:

$$R_n* + CH_2* \rightarrow R_{n+1}* + * \quad [2.16]$$

Currently, this theory is the most accredited to describe the formation of linear paraffins and olefins. The formation of such products can be schematized as illustrated in Figure 2.1.

The carbide theory, in contrast to the other two theories, does not explain the formation of oxygenated species other than water.

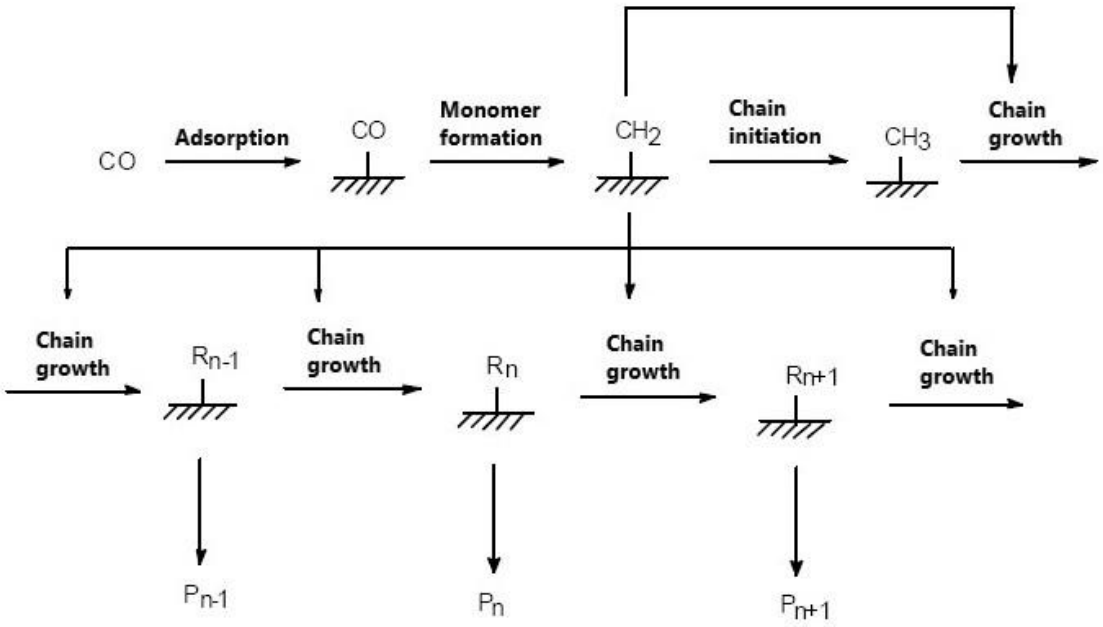

Figure 2.1: Chain growth mechanism according to the carbide theory.

In order to explain the formation of oxygenated species, Dry [38, 39, 34] proposed a complementary mechanism that leads to the formation of aldehydes (eq. 2.19), alcohols (eq. 2.20) and carboxylic acids (eq. 2.21):

$$2\ CH_2{*} \rightarrow CH_3CH{*} \quad [2.17]$$

$$RCH{*} + CO + {*} \rightarrow RCHC{*}O{*} \quad [2.18]$$

$$RCHC{*}O{*} + H_2 \rightarrow RCH_2CHO + 2{*} \quad [2.19]$$

$$RCHC{*}O{*} + 2\ H_2 \rightarrow RCH_2CH_2OH + 2{*} \quad [2.20]$$

$$RCHC{*}O{*} + H_2O \rightarrow RCH_2COOH + 2{*} \quad [2.21]$$

The inability of the three mechanistic theories mentioned above to completely describe the wide spectrum of products formed in the Fischer-Tropsch synthesis suggest that the real mechanism of FTS includes more than one key intermediate [34;40]. A further reaction mechanism for FTS [41] is proposed by Iglesia [41] (Figure 2.2).

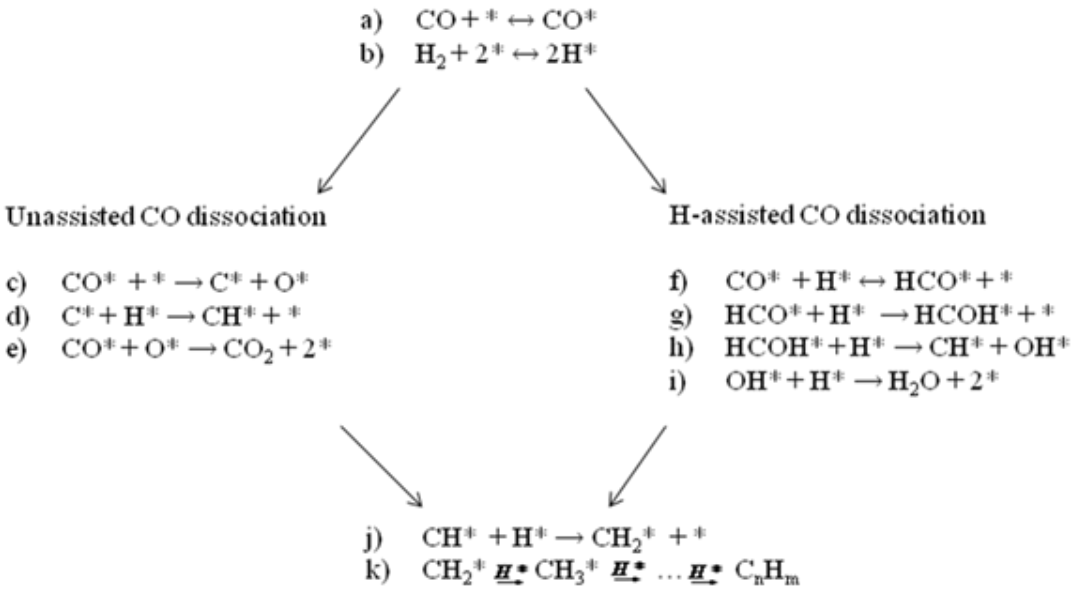

Figure 2.2: Chain growth mechanism according to Iglesia [41].

As shown in figure 2.2 the CO adsorbed on the surface of the catalyst can dissociate according to two different mechanisms: (i) the unassisted dissociation mechanism provides the formation of C* and O* starting from CO*. The subsequent reactions of C* with H* forming the monomer CH_2*. The O* formed is removed by reacting with CO* to form CO_2; (ii) The H-assisted dissociation mechanism which involves the formation of formyl (HCO*) as reaction intermediate and subsequently, through further hydrogenation, the formation of hydroxymethylene as intermediate. The dissociation of this species leads to the CH* species which it is the chain initiator, and to the OH* species that hydrogenating leads to the formation of H_2O. Through kinetic and theoretical studies, Iglesia found that for iron-based catalysts, the mechanism with the lowest activation energy is that based on the unassisted CO dissociation, which explains the high CO_2 concentration. On the contrary, the predominant mechanism found for cobalt-based catalysts is the H-assisted dissociation.

2.5 Products distribution

2.5.1 ASF distribution

Although the chemistry of the Fischer-Tropsch synthesis is complex, the fundamental aspects can be described by a few generalized equations (eq. 2.1-2.3). Irrespective of operating conditions and catalysts, the FT synthesis always produces a wide range of olefins, paraffins and oxygenated products (alcohols, aldehydes, acids and ketones). The variables that influence the product distribution are temperature, feed gas composition, pressure and catalyst choice. The FT products are formed through a sort of surface polymerization reaction, which involves the following steps: (i) reactant adsorption and dissociation, (ii) chain initiation, (iii) chain growth, (iv) product desorption and (v) readsorption of certain products with further reactions. The competition between chain growth and chain termination is determined by the probability of growth, called the α-value. A higher α-value will result in longer hydrocarbons and thus in a heavier product distribution (Figure 2.3).

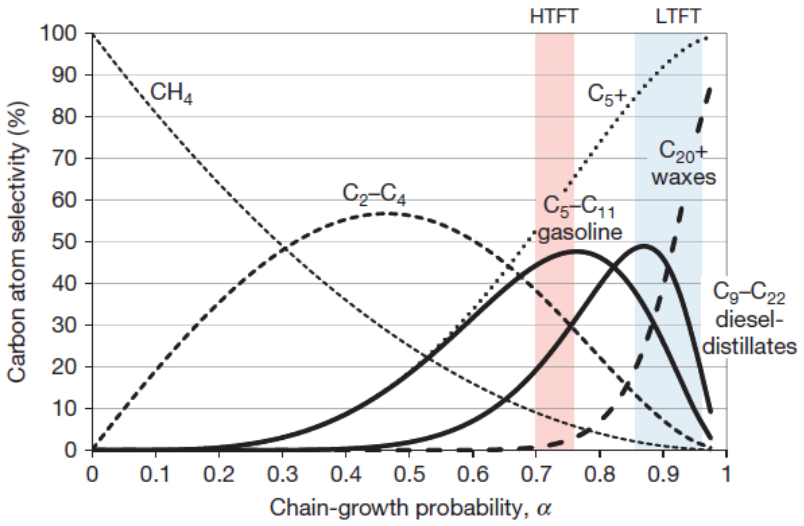

Figure 2.3: Hydrocarbon product distribution during FTS as a function of the chain growth probability factor α (High-temperature FT technology (HTFT) corresponds approximately to $0.70<\alpha<0.75$, and low-temperature FT (LTFT) to about $0.85<\alpha<0.95$.

If α is independent of carbon number, the total amount of carbon contained in products with n carbon atoms (namely C_n) can be formulated on a relative basis:

$$C_1 = 1(1-\alpha) \quad [2.22]$$

$$C_2 = 2(1-\alpha)\alpha \quad [2.23]$$

$$C_3 = 3(1-\alpha)\alpha^2 \quad [2.24]$$

$$C_n = n(1-\alpha)\alpha^{n-1} \quad [2.25]$$

The total amount of carbon in the product spectrum then forms a convergent infinite sum with an analytical solution:

$$\sum_1^\infty C_n = \sum_1^\infty n(1-\alpha)\alpha^{n-1} = \frac{1}{1-\alpha} \quad [2.26]$$

This means that the selectivity toward products with n carbon atoms on a carbon atom basis, namely S_n, can be expressed as follows:

$$S_n = \frac{C_n}{\sum_1^\infty C_n} = n\,(1-\alpha)^2\alpha^{n-1} \quad [2.27]$$

After converting this equation to the logarithmic domain and rearranging, it is found that:

$$\ln\left(\frac{S_n}{n}\right) = nln\alpha + \ln\frac{(1-\alpha)^2}{\alpha} \quad [2.28]$$

As a result, a plot of $\ln(S_n/n)$ versus the carbon number (n) gives a straight line with a slope equal to $\ln(\alpha)$ (Figure 2.4). However, deviations in the actual FT product spectrum from the

ideal Anderson–Schulz–Flory distribution are usually observed [12]. These include a higher methane and a lower C_2 selectivity than the value predicted by the equation (Figure 2.4). There is also an increase in the chain growth probability factor and a concomitant decrease in the olefin/paraffin ratio with hydrocarbon chain length. In addition to linear alkanes and 1-alkenes, a variety of other products are also formed, including branched aliphatic compounds, alcohols, aldehydes, ketones, acids, and (at sufficiently high operating temperatures) even aromatics. This shows the complexity of the reaction and explains why many issues regarding the reaction mechanism still remains unresolved.

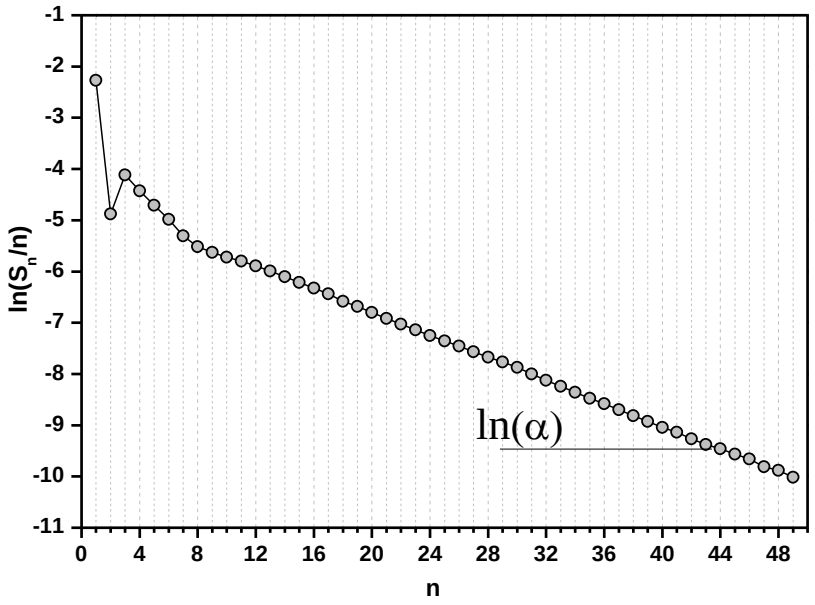

Figure 2.4: ASF distribution plot

2.5.2 The deviation for methane and ethylene

The high productivity of methane, compared to the theoretical prediction of the ASF model, can be explained by assuming the existence of different catalytic sites able to activate the methanation reaction [33].

Moreover, the VIII group metals, used as catalysts for the Fischer-Tropsch synthesis, are able to activate the hydrogenolysis reaction of the paraffins and the olefins produced [42]. The hydrogenolysis reaction is substantially a demethylation and, therefore, could explain the greater productivity of methane (eq. 2.29):

$$C_nH_{2n+1}* + H* \rightarrow C_{n-1}H_{2n+1}* + CH_3* \qquad [2.29]$$

The hydrogenolysis reaction was studied by Kuipers and collaborators using cobalt based catalysts. From these studies he derived that the hydrogenolysis is a reaction that is negligible at temperatures below 275 ° C and in the presence of high water and carbon monoxide partial pressures [43].

The deviation of methane can be also related to mass transport phenomena, which alter the H_2/CO ratio at the catalytic surface and favor the hydrogenation reactions [34].

The presence of hot spots along the catalyst bed, related to the heat transfer issue, may involve a local overheating of the catalyst and hence contribute to the increase of the methane productivity.

According to Wojciechowski [30] the overestimation of the ethylene productivity with respect to theoretical predictions can be explained by assuming a high surface mobility and reactivity of the precursor of this species.

The presence of secondary reactions is considered a further reason of this overestimation. Indeed, it is generally recognized that ethylene is reintroduced into the hydrocarbon chain growth process.

A further hypothesis is the greater sensitivity of ethylene with respect to the hydrogenolysis reaction.

2.5.3 Double chain growth probability

Instead of a linear trend in the ASF-plot, the products distribution shows a double chain growth probability in correspondence of the hydrocarbon with carbon number equals to 8.

The cause of this deviation is a disputed topic [44,15,45]. It is attributed to the existence of multiple chain growth mechanisms or multiple different active sites on the catalyst or assuming an effect of the olefins readsorption and consecutive incorporation into the chain growth. Concerning the latter explanation, it is observed that the olefin to paraffin ratio decreases with the increase of the number of carbon atoms: the trend of this ratio is well represented by eq. 2.30, which links the decrease in the ratio with the exponential of N:

$$\frac{O_N}{P_N} \propto e^{-C \cdot N} \qquad [2.30]$$

where O_N and P_N are, respectively, the molar fractions of olefin and paraffin with N carbon atoms in the products and C is a constant.

Kuipers et al. explained this trend considering the secondary reactions of the olefins species: (i) hydrogenation, (ii) reinsertion, (iii) hydrogenolysis and (iv) isomerization [46]. In contrast to paraffins, in fact, experimental evidences show that olefins can be readsorbed on the catalytic sites, and reinserted to the chain growth mechanism or hydrogenated to the corresponding paraffin (with the same carbon number).

Kuipers et al. [46] identified three possible routes of the olefins species:

- the olefins diffusion inside the liquid hydrocarbons which fill the pores of the catalyst;
- the solubility of olefins in the liquid hydrocarbons that fill the pores of the catalyst;
- the strength of the physical adsorption of olefins at the catalytic surface.

In order to better clarify the situation, in figure 2.5 it is reported a schematization of the concentration profile of olefins as a function of the distance from the catalytic surface.

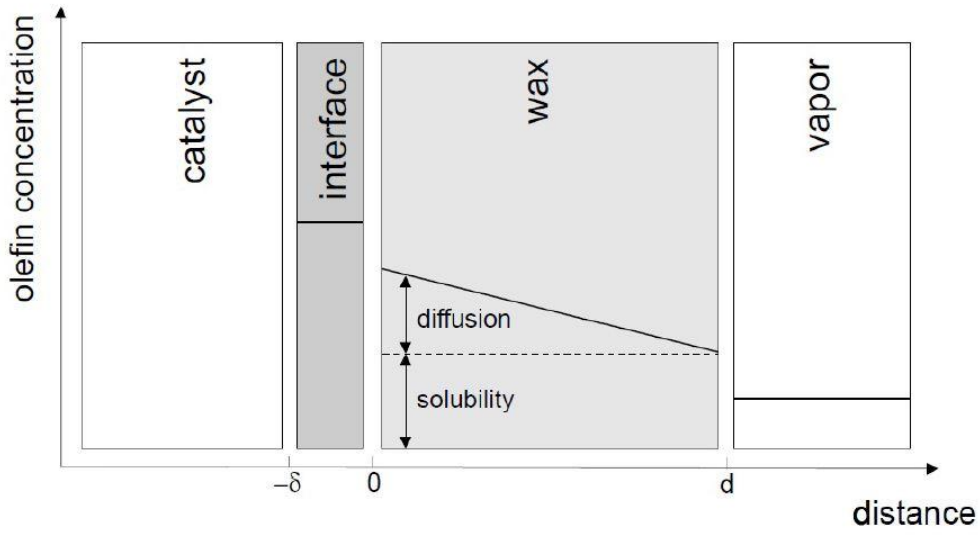

Figure 2.5: Schematization of the concentration profile of olefins according to the distance from the catalytic surface.

The concentration of the olefins dissolved in the hydrocarbon phase for x = d can be related, using balance considerations, to the corresponding bulk concentration of the vapor phase. Within the hydrocarbon film covering the catalytic surface (0 <x <d) a concentration gradient of the olefins is established on the basis of the speed of the formation of this product, the thickness of the film and the diffusivity.

The diffusion D_N of olefins (m^2 / s) varies with N according to the following exponential relationship, proposed by Kuipers et al. [46]:

$$D_N = D_0 e^{-0.6 \cdot N} \qquad [2.31]$$

where D_0 represents the reference diffusion coefficient.

The same relationship was proposed by Iglesia et al. [47], using an exponential coefficient of - 0.3 instead of - 0.6. In correspondence of the catalytic surface (x = - δ) the physisorption of

olefins takes place, a phenomenon that is considered dependent on the length of the olefin chain. Iglesia et al. [47] interpreted the decrease of O_N / P_N based on the diffusive limitations. The equation 2.31 is representative of the decrease in diffusivity with the increase of N. In other words, by increasing N, the mobility of olefins within the hydrocarbon film decreases. This causes an increase of the contact time of these species and, therefore, of the probability of readsorption [46].

However, the authors didn't to explain the rapid decrease in the O_N / P_N ratio with N solely on the basis of diffusion phenomena. The diffusive limitations are predominant, in fact, only when the thickness of the hydrocarbon film covering the catalyst is consistent, or for low contact times. However, even under these conditions, the role of diffusive limitations is only important for low carbon number olefins ($N < 7$). The dependence of the O_N / P_N ratio with the olefinic chain length must therefore be explained by assuming the importance of the role of solubility and physical adsorption, which are phenomena favored by the growth of N. The solubility of olefins increases exponentially with N and, consequently, the rate of resorption of long-chain species is favored with respect to short-chain species.

Moreover, the hydrocarbon phase covering the catalyst consists of paraffins with a composition dictated by the thermodynamic equilibrium and, therefore, by the conditions under which the system operates. Generally, the predominant species in the liquid hydrocarbon phase are those with N between twenty-three and thirty. As a consequence, the solubilization of heavier olefins is more favored since they are more similar to the hydrocarbon solvent. Also the phenomena of physical adsorption can influence the dependence of the secondary reactions of the olefins from N. Typically, in fact, the logarithm of the adsorption equilibrium constant increases linearly with N. Keldsen et al., measuring the adsorbent enthalpies (kJ / mol) of the paraffins,

found that the adsorbent - adsorbed interactions grow with N with the following equation [46]:

$$-\Delta H_{ads} = 12{,}6 + 8{,}7 \cdot N \qquad [2.32]$$

It follows an enrichment in long-chain species of the area in direct contact with the catalytic surface.

2.6 Reactors for the Fischer-Tropsch synthesis

The heat released per mole of CO converted or CH_2 formed is about 165 kJ, which makes the FTS one of the most exothermic processes in industrial chemistry. Because of this, it is important to have an efficient heat transfer from the catalyst particles to the surrounding. Otherwise, the particle temperature would increase resulting in an increase in the selectivity to light hydrocarbons, especially methane, and a loss of activity due to sintering and fouling.

Multi-tubular fixed bed (Figure 2.6) and slurry bed reactors (Figure 2.7) are used for the LTFT synthesis. Tubular reactors are simpler to operate and, since the liquid wax trickles down the catalyst bed, there is no need for a wax-catalyst separation unit. The latter, instead, is essential for slurry bed reactors as the small catalyst particles used are suspended in the liquid wax medium. On the large scale, slurry reactors are often preferred to fixed bed because of several advantages: lower construction costs, lower pressure drops over the reactor, more isothermal beds and longer reactors runs because on-line removal of used catalyst and the addition of fresh catalyst can be applied. However, critical points for slurry reactors are the catalyst/liquid products separation and the mechanical resistance of the catalyst particles. Industrially, Sasol I, Shell-SMDS and Pearl GTL plants are based on multi-tubular fixed bed technology, while the Oryx plant is based on slurry bed technology.

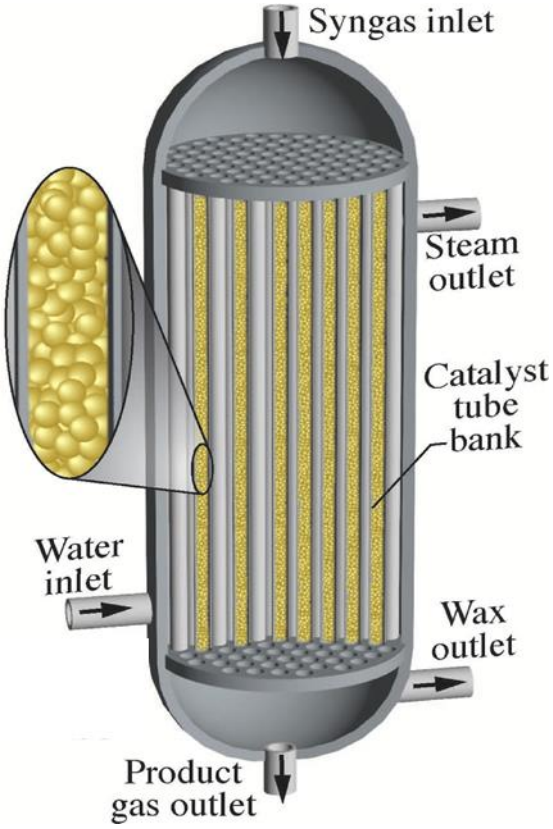

Figure 2.6: Illustration of packed-bed Low-Temperature Fischer–Tropsch (LTFT) reactor.

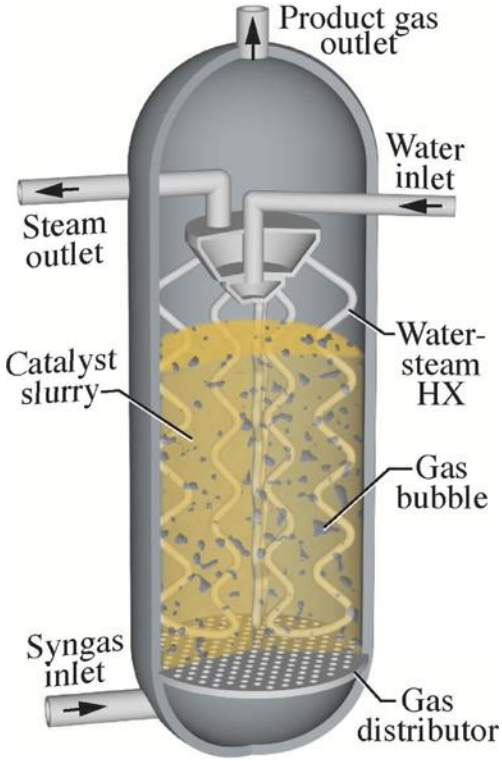

Figure 2.7: Illustration of slurry Low-Temperature Fischer–Tropsch (LTFT) reactor.

Two phase fluidized bed reactors are used with iron based catalysts for the HTFT synthesis. Conditions resulting in the production of waxes should be avoided in this case, as the presence of liquid wax on the outside of the catalyst particles will result in defluidization of the catalyst bed. Because of the turbulent nature of fluidized bed reactors at the gas space velocities used, the rate of heat exchange from the catalyst to the heat exchanger tubes is very high, resulting in nearly isothermal catalyst bed. An important advantage of using fluidized bed reactors at high temperature, where the rates of catalyst deactivation are inevitability high, is that the deactivated catalyst can be removed and fresh catalyst added on-line, which means long continuous runs can be achieved. Industrially, Sasol II, Sasol III and the PetroSA plant are based on fluidized bed technology.

2.6.1 Compact reactors

In conventional GTL applications, the Fischer-Tropsch (FT) process is carried out in huge fixed bed or slurry reactors. They require a capital investment of $ 3 billion, thus constituting a solution economically valid for plants with a production of at least of 30000 barrels per day (Bpd). Only about 6% of the gas fields in the world are large enough to support a GTL plant of this size.

Recently, the concept of “smaller-scale GtL” is taking off as an important opportunity to unlock up to 50% of the stranded gas fields that conventional GtL cannot exploit economically. The compact GtL system is based on the modularization of GtL technology. This feature allows the GTL plants to be constructed in remote locations with significant amounts of cheap gas and demand for liquid fuels.

Velocys FT technology

Velocys Inc. based in Columbus, Ohio, USA, recently (2013) launched on the market a new technology for the exploitation of remote and stranded natural gas. The success of the small GTL Velocys technology [48] is the combination of microchannels reactors and the use of highly active catalysts. In this reactor (Figure 2.8), the catalyst is housed within wave-like fin structures that promote heat transfer from the catalyst bed. Syngas enters from the top and flows downward through the catalyst bed, with Fischer–Tropsch products exiting at the bottom. The reaction heat is removed by the pressurized-water coolant within cross-flow microchannels. The fin spacing and coolant channels are on the order of a millimeter. The highly efficient heat transfer associated with microchannels delivers a compact, high-performance reactor.

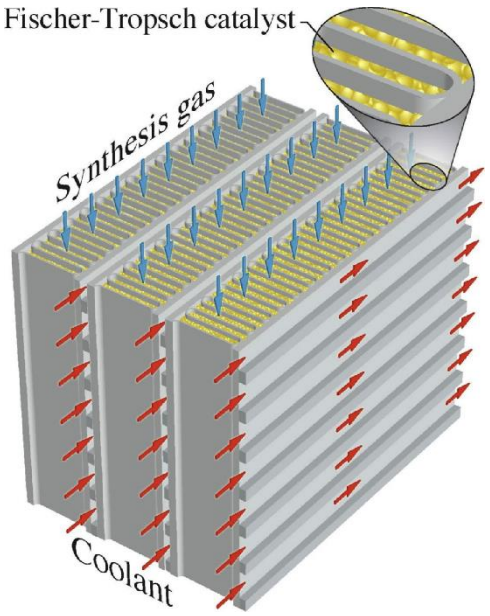

Figure 2.8: Velocys microchannel reactor.

Figure 2.9 illustrates the packaging of three microchannel Fischer–Tropsch reactors within a pressure vessel. Each of the reactors have overall dimensions on the order of a meter. Syngas enters the reactors' catalyst sections from above via a gas-distribution manifold. The Fischer–

Tropsch products are collected through manifolds at the bottom of the reactors. Pressurized cooling water enters through manifolds that feed the microchannel arrays, with the water-steam exhaust mixture leaving the reactors into the outer pressure-vessel housing. Water vapor exhausts at the top of the pressure vessel and condensed water drains through the bottom.

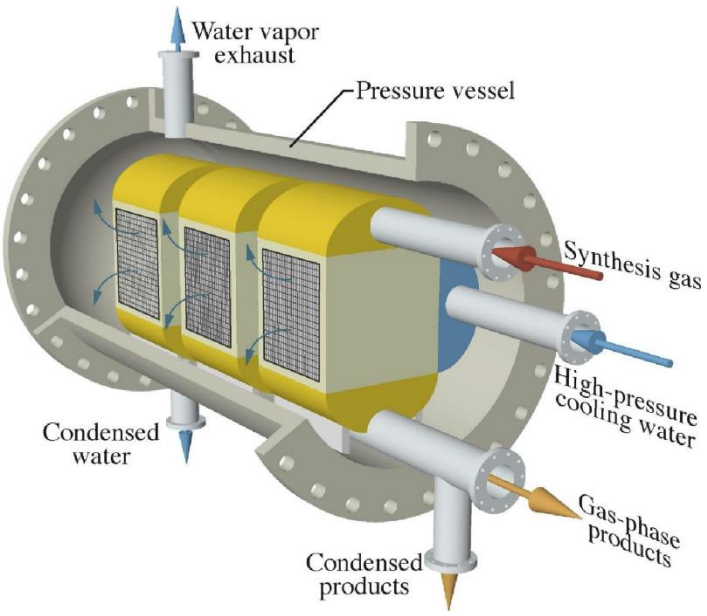

Figure 2.9: Three microchannel Fischer–Tropsch reactors within a pressure vessel.

Velocys microchannels technology is commercially feasible for capacity of production starting from 1500 barrels per day, which makes it a valid alternative for small-scale applications in the processes of GTL and BTL. The June 25, 2014 Velocys announces the acquisition of Pinto Energy LLC ("Pinto Energy") and the Ashtabula GTL project [49]. Pinto Energy is one of the largest developers of small scale GTL projects in North America. Pinto Energy is developing a first plant with a production capacity of approx. 2800 barrels per day (bpd). The site stands in an industrial area of 80 hectares near the port of Ashtabula, Ohio, United States of America.

CompactGTL FT technology

CompactGTL industry based in the United Kingdom, developed a compact GTL technology. The technology involves the use of property catalysts and reactors whose design derives from the production techniques of plate heat exchangers (plate-fin). The modular plant, incorporates several reactors in parallel, providing a flexible solution to cope with variations in gas supply and decrease in flow during the life of the reservoir. At the heart of the process there are two sets of modular reactor blocks. The use of advanced technology, derived from plate heat exchangers production techniques, allows these reactors to have a precise control of heat and gas flow to the metal catalyst supported and structured, arranged in a regular series of thousands of close channels. The first reactor uses methane from steam reforming (SMR) to convert natural gas into syngas. The syngas is fed into the second reactor where it is converted by the Fischer-Tropsch process into synthetic crude, water and a tail gas composed of hydrogen, carbon monoxide and light hydrocarbon gases.

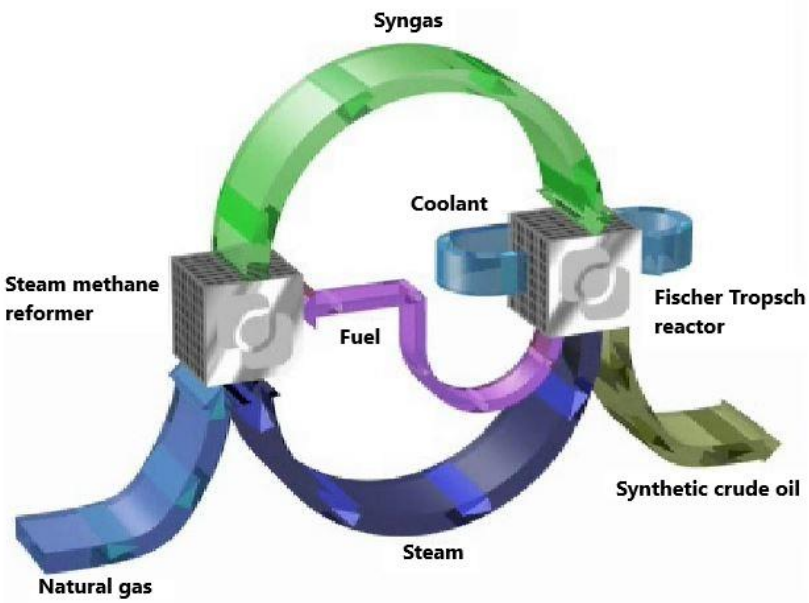

Figure 2.10: CompactGTL process scheme.

The close interaction between the two reactors in the CompactGTL process is a crucial element in the efficient management of the overall system. The two reactions are coupled to work together, maximizing the efficiency. The water produced in the Fischer-Tropsch reaction can be treated to remove impurities and recycled in the steam reforming process. The reactor technology, proprietary CompactGTL, allows the design of a highly autonomous plant that does not require an oxygen supply. The process involves only small volumes of fluids, this makes it proof of the phenomenon of "wave motion" present in offshore installations.

2.7 References

[1] P. Sabatier, J. D. Senderens, Comptes Rendus Hebdomadaires des Séances de l'Académie des Sciences 134 (1902) 514-516

[2] Badische Anilin und Soda Fabrik, German Patent 293787

[3] F. Fischer, H. Tropsch, Brennstoff-Chemie, 4 (1923) 276-285

[4] F. Fischer, H. Tropsch, German Patent 484337

[5] F. Fischer, H. Pichler, German Patent 731295

[6] F. Fischer, H. Pichler, Gesammelte Abhandlungen zur Kenntnis der Kohle 13 (1937) 407

[7] H. Pichler, H. Buffleb, Brennstoff-Chemie 19 (1938) 226

[8] A. P. Steynberg, M. E. Dry, B. H. Davis, B. B. Breman, Fischer-Tropsch technology. Studies in Surface Science and Catalysis, vol. 152. A. P. Steynberg, M. E. Dry, Editors 2004, Elsevier, Amsterdam, pp. 406-481

[9] Velocys. Construction complete at ENVIA's GTL plant, September 2016,

[10] J. W. A. De Swart, R. Krishna, S. T. Sie, Studies in Surface Science and Catalysis 107 (1997) 213-218

[11] M. Dry, in: G. Ertl, H. Knozinger, F. Schuth, J. Weitkamp (Eds.), Handbook of Heterogeneous catalysis, Wiley-VCH, Weinheim, 2008, pp. 2965-2994

[12] J. van de Loosdrecht, F.G. Botes, I.M. Ciobica, A. Ferreira, P. Gibson, D.J. Moodley, A.M. Saib, J.L. Visagie, Reference Module in Chemistry, Molecular Sciences and Chemical Engineering Comprehensive Inorganic Chemistry II (Second Edition), From Elements to Applications, 2013, Pages 525–557, Volume 7: Surface Inorganic Chemistry and Heterogeneous Catalysis

[13] A.Y. Khodakov, W. Chu, P. Fongarland, Chemical Review 107 (2007) 1692

[14] R. L. Espinoza, J. L. Visagie, P. J. Van Berge, F. H. Bolder, US5733839A

[15] E. J. Creyghton, C. M. A. M. Mesters, M. J. Reynhout, G. L. M. M. Verbist, US 2008/0171655A1

[16] A. Hoek, A. H. Joustra, J. K. Minderhoud, M. F. M. Post, EP 0104672 B1

[17] S. A. Posthuma, H. M. H Wechem, H. Heetveld, U.S 5486542

[18] R. J. Dogterom, R. M. van Hardeveld, M. J. Reynhout, B. A. van de Werff, US 7790648 B2

[19] J. L. Visagie, H. M. Veltman, WO 2006075216 A1

[20] P. J. van Berge, S. Barradas, US 7365040 B2

[21] P. J. van Berge, J. van De Loosdrecht, S. Barradas, WO 2003012008 A2

[22] P. J. van Berge, J. van De Loosdrecht, L. Jacobus, US 5053574

[23] P. J. van Berge, J. van De Loosdrecht, L. Jacobus, US 5718844

[24] S. Barradas, E. A. Caricato, B. H. Sigwebela, J. P. van Berge, J. van De Loosdrecht, US 4568663

[25] R. Oukaci, A. H. Singleton, J. G. Goodwin Jr, Applied Catalysis A: General 186 (1999) 129-144

[26] S. C. Leviness, F. Daly, L. A. Richard, S. Rugmini, US9359271 B2

[27] D. Pinna, Modelli cinetici per la sintesi di Fischer-Tropsch, Tesi di dottorato, Università degli studi di Milano-Polimi, 2002.

[28] R. C. Brady et al., Mechanism of the Fischer-Tropsch reaction. The chain propagation step, Journal of American Chemical Society, vol. 103(5) (1981), pagg. 1287-1289.

[29] H. Schultz, Short History and Present Trends of Fischer-Tropsch Synthesis, Appl. Cat. A: General 186 (1999), pagg 3-12.

[30] B. Sarup, W. Wojciechowski, Studies of the Fischer-Tropsch Synthesis on a Cobalt Catalyst. I. Evaluation of Product Distribution Parameters from Experimental Data, Catal. Rev. – Sci. Eng., (1988) 30, pag. 629.

[31] H. Schultz, Major and Minor Reactions in Fischer-Tropsch Synthesis on Cobalt Catalysts, Topics in Catalysis, vol. 26 (2003), pagg. 73-85.

[32] E. Van Steen, H. Schulz, Polymerisation Kinetics of the Fischer-Tropsch CO Hydrogenation using Iron and Cobalt Based Catalysts, Appl. Catal. A: General 186 (1999), pagg. 309-320.

[33] H. Schulz et al., Kinetic modelling of Fischer-Tropsch product distribution, Applied Catalysis A: General, vol. 186 (1999), pagg. 91-107.

[34] M. E. Dry, Practical and Theoretical Aspects of the Catalytic Fischer-Tropsch Process, Applied Catalysis A: General, vol. 138 (1996), pag. 319.

[35] D. J. Duvenhage, T. Shingles, Synthol Reactor Technology Development, Catalysis Today 71 (2002), pagg. 301-305.

[36] J. Patzlaff, Y. Liu, C. Graffmann, J. Gaube, Studies on Product Distributions of Iron and Cobalt Catalyzed Fischer-Tropsch Synthesis, Applied Catalysis A: General 186 (1999), pagg. 109-119.

[37] R. C. Brady et al., Mechanism of the Fischer-Tropsch reaction. The chain propagation step, Journal of American Chemical Society, vol. 103(5) (1981)

[38] P. Winslow et al., Application of transient response techniques for quantitative determination of adsorbed carbon monoxide and carbon present on the surface of Ruthenium catalyst during Fischer-Tropsch synthesis, Journal of Catalysis, vol. 86 (1984) pagg. 158-172.

[39] X. Zhou et al., CO hydrogenation on Ru/Al_2O_3; selectivity under transient conditions, Journal of Catalysis, vol. 105 (1987), pagg. 499-510.

[40] A. A. Adesina, Hydrocarbon synthesis via Fischer-Tropsch reaction: travails and triumphs, Applied Catalisys A: General, vol. 138 (1996), pagg. 345-367.

[41] Ojeda, M., Nabar, R., Iglesia, E., "CO activation pathways and the mechanism of Fischer-Tropsch synthesis", journal of catalysis 272 (2010) 287-297.

[42] S. Morselli, Effect of cobalt Fischer-Tropsch catalyst design on activity, selectivity and reaction kinetic, Scuola normale superiore di Pisa, Tesi di dottorato.

[43] J. Patzlaff et al., Interpretation and kinetic modeling of product distributions of cobalt catalyzed Fischer-Tropsch synthesis, Catalysis Today, vol. 71 (2002), pagg. 381-394.

[44] R. Oukaci, A. H. Singleton, J. G. Goodwin Jr, Applied Catalysis A: General 186 (1999) 129-144

[45] J. T. Kummer, H. H. Podgurski, W. B. Spencer, P. H. Emmett, Journal of the American Chemical Society 73 (1951) 564-569

[46] P. Gerard et al., Kinetics and Selectivity of the Fischer-Tropsch Synthesis: A Literature Review, Catalysis Reviews – Science and Engineeing, vol. 41 (1999), pagg. 255-318.

[47] E. Iglesia, Transport enhanced α-olefin readsorption pathways in Ru-catalyzed hydrocarbon synthesis, Journal of Catalysis, vol. 129 (1991), pagg. 238-256.

[48] Steve LeViness. *Velocys Fischer-Tropsch Synthesis Technology - Comparison to Conventional FT-Technologies*.April2013.url:http://www.velocys.com/arcv/press/ppt/AIChE%202013%20-Presentation%2004-30-13%20- %20LeViness%20v1_rev1.pdf

[49] Velocys. Acquisition of Pinto Energy and Ashtabula GTL Project. 25 June 2014, url: http//www.velocys.com/financial/nr/nr140625.php

Chapter 3

Plant and experimental procedures

3.1 Introduction

The following chapter describes the lab-scale apparatus (named FBR-PoliMi) used for the collection of the experimental data. The FBR-PoliMi is located at the laboratories of the Energy Department in Politecnico di Milano.

3.2 FBR – PoliMi

The P&ID of the FBR-PoliMi plant is reported in Appendix (B). The lab-scale plant can be divided in five different sections:

1. Reagents feed zone;
2. Reaction zone;
3. Area for collecting condensable products;
4. Zone of depressurization;
5. On-line analysis area for uncondensable products.

The first zone consists of three independent lines through which the reagent gases are fed to the reactor. These gas lines fed respectively the synthesis gas ("syngas"), which is the mixture of hydrogen and carbon monoxide in molar ratio of 2, pure hydrogen and nitrogen. The gases are stored in 50 L (syngas) and 40 L (pure gases) tanks. The three gas lines are mainly constituted by a flow regulator (mass flow controller, Brooks Instrument model 5850S) and high-pressure gauges. Solenoid valves are also present in each line. On the syngas feeding line, there is a ferrocarbonyls trap kept at 180°C and two traps filled of activated carbons and molecular sieves, respectively. These traps are useful to remove any catalyst poisons present in the tank. An oxygen trap is also present on the nitrogen feeding line.

The reaction zone comprises the fixed-bed reactor (Figure 3.1), which is a stainless steel tube with an outer diameter of 33.4 mm, 5.6 mm thick and 86 cm long. Before flowing into the reactor, the reagents are preheated at 115°C.

The reactor is inserted in a vertical electric oven (Carbolite), in which three heating zones are present so to ensure a very good temperature homogeneity. Accordingly, it allows an isothermal length of the reactor of around 20 cm.

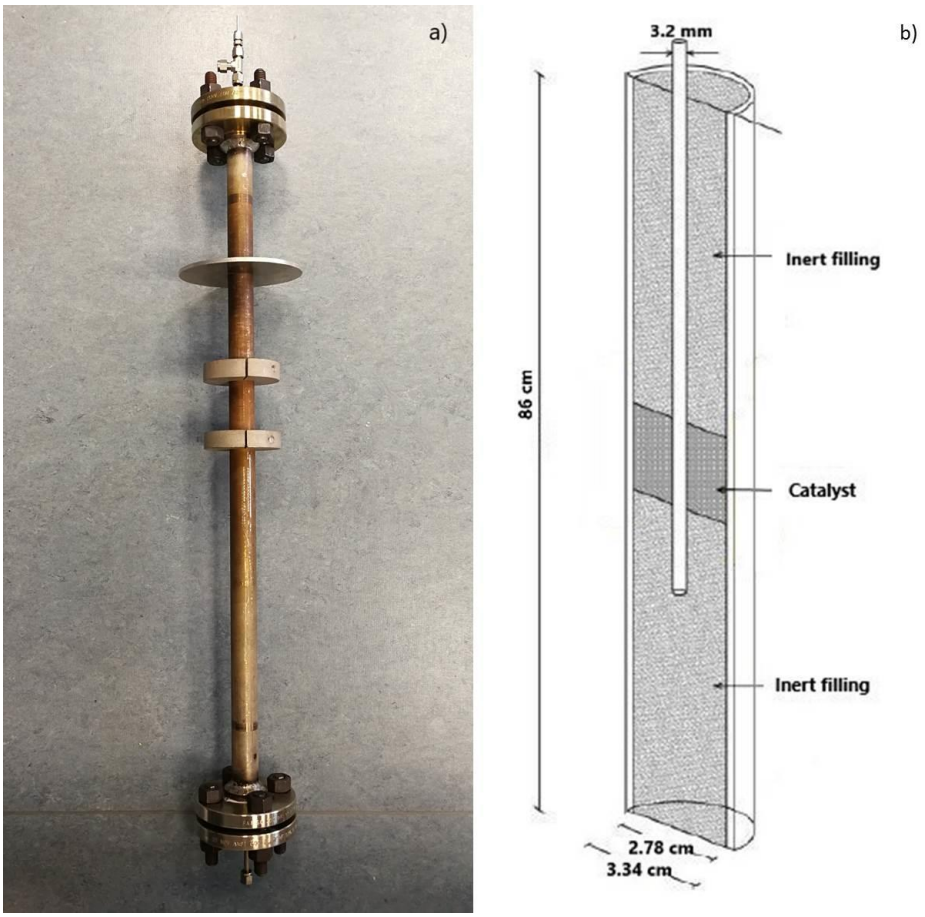

Figure 3.1: (a) image of the FBR-PoliMi reactor; (b) scheme of the reactor.

The third zone is the products collection area. The outgoing line from the reactor kept at 150°C is connected with two parallel lines, named the primary and secondary lines, by means of a three-way solenoid valve . On the primary line, which is kept at 120 °C, two tanks are mounted for the storage and tapping of the products. The heaviest hydrocarbons (waxes) are collected in the first tank kept at 150 °C. The aqueous phase and the light hydrocarbons (mainly diesel) are condensed in the second tank kept at 0°C. The secondary line is useful to isolate the primary line from the rest of the plant, for example during the sampling of the products. Also the secondary line is equipped with a tank kept at room temperature.

The reaction products in the gas phase go beyond the tanks and are depressurized thanks to the backpressure (Brooks Mod. 5866), which is an electronic pressure controller and regulator. The backpressure allows keeping the plant at the desired pressure and to bring all

the outgoing gas from the reactor to atmospheric pressure. In order to guarantee the safety of the system in conditions of power failure, a further line parallel to the previous one connected with the electronic backpressure is activated with a solenoid valve. In this line, the regulation of the pressure is guaranteed by a manual regulation valve. After the pressure regulator, the gas is intercepted by a three-way valve that allows to send the entire flow alternately to the on-line analysis gas chromatograph or directly to the flow totalizer (Flow Gas Meter, Ritter Mod. TG05-5).

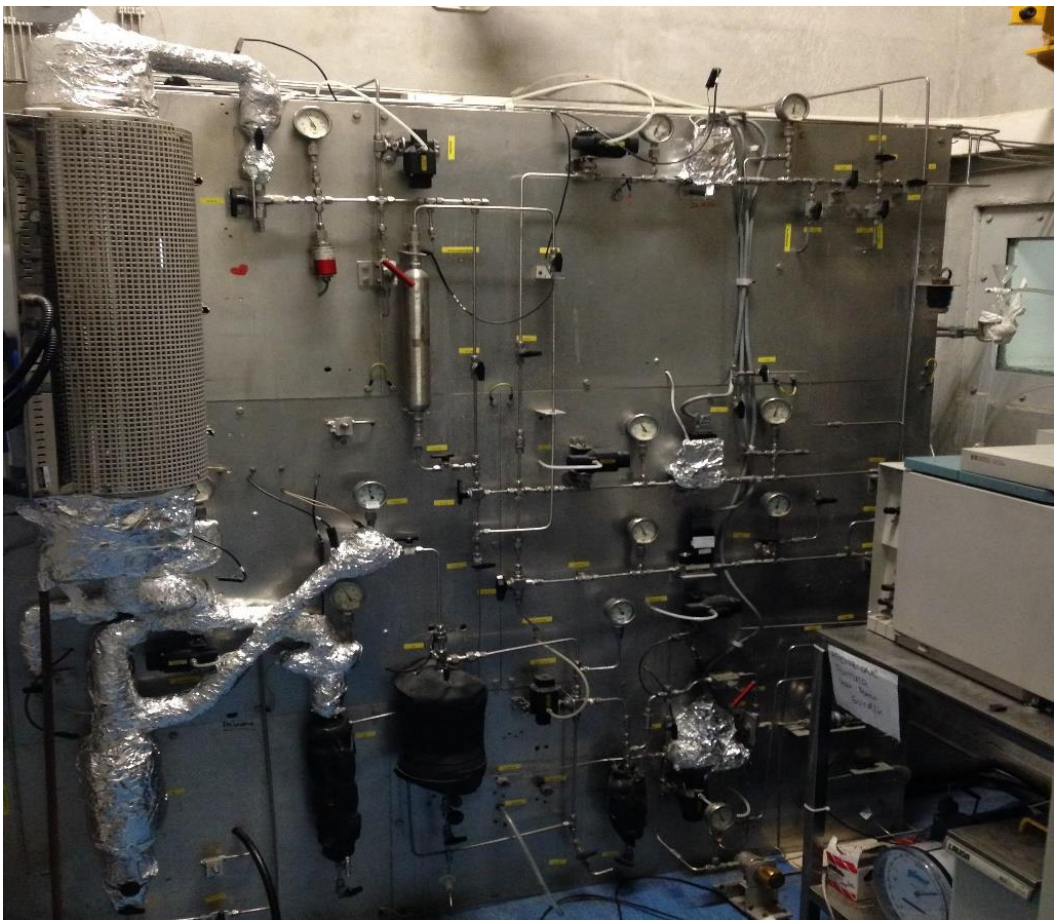

Figure 3.2: FBR-PoliMi plant.

3.3 Control and data acquisition system

The plant is equipped with a special control and data acquisition system able to monitor all the process variables (Temperature, Pressure, Flows etc.) continuously (24/24 h).

3.3.1 Control system

The control of all the process variables is performed thanks to four programmable multi-loop PLCs (PLC) controller (Ascon, AC20 model). The controllers are interfaced with each other through a local LAN-type LAN communication network and are able to memorize the trends of the process variables in a special memory for a time not exceeding 5 hours [1]. The controllers are equipped with a LCD graphic display (128 x 320 pixels) which displays the trends of the process variables. The regulation of the variables is managed by operating on the front panel of each controller (Figure 3.3).

Figure 3.3: PLC multi-loop controller.

3.3.2 Acquisition System.

The acquisition system is designed to monitor the process variables indefinitely because the memory of the AC20 stations is able to record trends, current values, logic states and alarm states for times of no more than 5 hours. The acquisition is made through a data acquisition card of the National Instrument mod AT-MIO 16E [2]. The signals are taken from the acquisition card directly from the terminal board located on the back panel of the Ascon. Then, they are sent to the National Instrument's LabVIEW program in the computer that allows you to capture, view and record the variables of interest. The communication protocol is the ModBus (National Instrument, Industrial Automation Server, version 2.1), of the Master-Slave type. The controllers have the function of Slaves and, therefore, respond to the commands sent by the supervision system. LabVIEW (Laboratory Virtual Instrument Engineering Workbench) is an operating environment based on the graphical programming language G.

The difference compared to the common programming languages (ex: C, basic, ...) is the possibility of operating in a graphic environment no longer based on a textual type code. This allows the realization of an efficient acquisition system even by users with modest experience in the field of programming by working through an iconic language. LabVIEW is equipped with specific function libraries specifically designed to carry out operations of interest. The graphical interface is that of a virtual instrumentation (front panel) through which it is possible to interact directly from the keyboard. In particular, this interface shows a simplified scheme of the plant (Appendix B). The graphical interface also shows the trends of the operating variables of interest. In particular, the temperatures of the catalyst and of the three zones of the oven are displayed, the pressure, the inlet and outlet gas flows from the reactor.

The variables are also recorded on a text file. The text file is updated every 20 seconds.

3.3.3 Interlock Procedures.

The interlock procedures are implemented in cases of emergency or in cases of power failure.

The power failure represents a critical situation since the plant is not equipped with an emergency generator. From the point of view of the experimental test, the blackout compromises the activity of the catalyst because the oven switches off and the temperatures cools down to the room temperature and the reactor is filled with nitrogen.

In this case, the solenoid valves present on the syngas/hydrogen feed line are 'fail close' type, i.e. they close instantaneously in the absence of electricity. Vice versa, the solenoid valve located on the nitrogen bypass line is 'fail open' type and opens automatically in the absence of electricity.

These valves operate thanks to the presence of an instrument air supply circuit managed by solenoid valves.

An appropriate gas sensor is located close to the plant to monitor escapes of CO and H_2. Interlocking procedures are activated if the gas sensor signals a concentration of CO or H_2 higher than 50 ppm. The emergency procedures are activated also if the pressure/temperature of the plant increases for some unknown reasons. All the alarms are set/reset on Ascon.

The procedures implemented are summarized by the following Table 3.1.

Table 3.1: Summary of security procedures

Alarm	Procedure
High T of catalytic bed	Force to zero the power supply signal of the electrical resistances of the three zones of the oven until the variable falls below the alarm threshold
Very high T of catalytic bed	Closes the interception valve of CO / syngas and H_2
Interception valves of N_2 line	Closes the interception valve of CO / syngas and H_2
High T in the upper oven	Force to zero the power supply signal of the electrical resistances of the upper zone of the oven until the variable falls below the alarm threshold
High T in the middle oven	Force to zero the power supply signal of the electrical resistances of the central zone of the oven until the variable falls below the alarm threshold
High T in the lower oven	Force to zero the power supply signal of the electrical resistances of the lower zone of the oven until the variable falls below the alarm threshold
High T heating tape	Force to zero the power supply signal of the electrical resistances of the heating tape until the variable falls below the alarm threshold
High P	Closes the interception valve of CO / syngas and H_2
Very high P	Opens the system's head and tail vent valves
Failed draft of the suction hood	Closes the interception valve of CO / syngas and H_2
CO leakage	Closes the interception valve of CO / syngas and H_2. Opens the actuation valve of N_2
H_2 leakage	Closes the interception valve of CO / syngas and H_2. Force to zero the power supply signal of the electrical resistances of all the heating tapes and of the oven.

3.3.4 Temperature control

The temperature control of the catalyst is a cascade control. Consider the complete jacketed mixing reactor shown in Figure 3.4., the exothermic reaction A → B occurs and the reaction heat is removed by the coolant which circulates in the jacket [3].

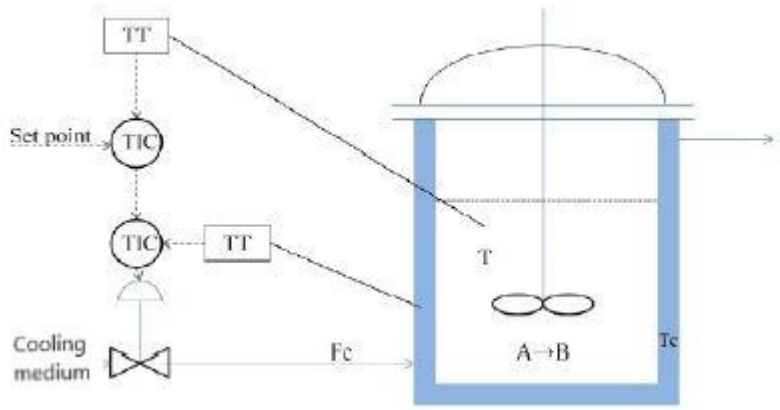

Figure 3.4: Cascade temperature control for a CSTR reactor.

To improve the system's response to a change of the temperature of the refrigerant Tc, the cascade control can be implemented. In this case there are two adjustment rings: a primary regulation ring which operates on the controlled variable temperature T and which uses a set point value supplied directly from the outside and a secondary regulation ring that measures Tc and uses the regulator output as the set point value for the secondary regulator. The two regulation rings operate on two different variables, T and Tc, and share the manipulated variable Fc (refrigerant flow rate). This configuration makes it possible to adjust the Fc so as to compensate for any changes of Tc before it can influence the reaction temperature T.

The reaction system used in the FBR-PoliMi is controlled in the same way. The reaction temperature is regulated thanks to the heat supplied by a resistor placed on the inner wall of the central area of the oven, powered by current I. The supplied power is controlled by Ascon.

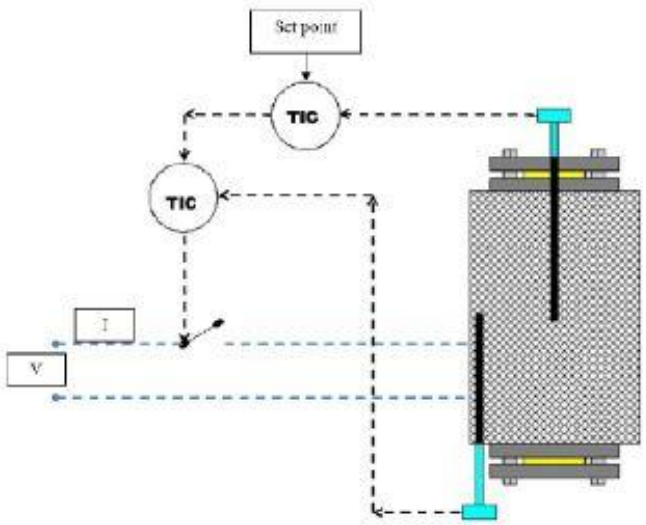

Figure 3.5: Cascade temperature control for FBR-PoliMi reactor.

In this case there are two adjustment rings: a primary regulation ring that operates on the controlled variable temperature inside the reactor and that uses a set point value supplied directly from the outside and a secondary regulation ring that measures the temperature in the central area of the furnace, outside the reactor, and near the resistances, which uses the output of the primary regulator as the set point value for the secondary regulator. The two regulation rings operate on two different variables: the internal temperature of the reactor and the temperature of the center of the oven. They share the variable manipulated that is the power supplied to the resistance of the center of the oven. This control configuration enables to intervene on the power supplied to the resistance located in the central part of the oven, i.e. at the position of the catalyst, so as to compensate for any variations in temperature of the central part of the oven before they can influence the temperature inside the reactor.

In general terms, the cascade control configuration allows to correct the effects that occur within the secondary regulation ring before they can influence the controlled variable. Furthermore, the secondary loop allows a more precise intervention on the manipulated variable. Consequently, both the readiness and the precision of the regulation are improved.

Because of the above it is necessary that the dynamics of the secondary regulation ring is faster than that of the primary regulation. A primary regulator P + I + D is adopted with parameters of the controller BP = 20 τi = 400 and τd = 100, while the secondary controller P has parameters BP = 0.5.

3.4 Analysis of the reaction products

The multiplicity of the species present in the reaction products leads to the formation of three different phases under ambient conditions (solid waxes, hydrocarbon organic phase and aqueous phase containing liquid alcohols). The analysis of the products is a fundamental operation because it allows the quantification of the reaction products and of the unreacted gases, thus leading to the evaluation of important process parameters, such as the conversion of the reagents, the productivity, the yield and the selectivity to the reaction products. The reaction products in the gas phase and the unreacted gases are analyzed through a gas chromatograph placed on line (HP model 6890). The condensable products are instead analyzed with an off-line gas chromatograph.

3.4.1 Online analysis.

The reaction products in the gas phase and the unreacted gases are sent to the online gas chromatograph (HP model 6890) through a system of six-way sampling valves that will be described in the following. The columns of the gas chromatograph are:

- Molecular sieve column. The column consists of a 1/8 inch and 3 m long steel tube wrapped around itself and a filling of 5 Å molecular sieves. The column is heated with a heating tape kept at 80 ° C since it is not inserted in the gas chromatograph oven;

- Al_2O_3-plot column. The capillary column consists of a 0.53 mm and a 30 m long tube internally filled with deactivated alumina. This column is inserted inside the gas chromatograph oven;
- Porapak column. The column has a length of 3 m and characteristics similar to the molecular sieves except for the filling, that is the Porapak Q type. This column is inserted in the gas chromatograph oven. In Table 3.2 are shown the operating conditions used for each column and the species that can separate.

Table 3.2: Operating conditions for the gas chromatograph columns

Molecular sieve column	
Detector T [°C]	250
Column T [°C]	80 (isothermal)
Upper column P [kPa]	290
Species separated inside the column	H_2, CO, Ar, N_2, CH_4
Al_2O_3 – plot column	
Injector T [°C]	200
Detector T [°C]	250
Column T [°C]	See scheduled Al_2O_3 – plot, Porapak
Upper column P [kPa]	30
Species separated inside the column	Hydrocarbons from C_1 to C_9
Porapak column	
Injector T [°C]	200
Detector T [°C]	250
Column T [°C]	See scheduled Al_2O_3 – plot, Porapak
Upper column P [kPa]	130
Species separated inside the column	Hydrocarbons from C_1 to C_4 and CO + N_2, CO_2

The columns Al_2O_3-plot and Porapak are both placed inside the gas chromatograph oven. To allow better separation of the products, the operating conditions of the oven are optimized by introducing a temperature ramp (Figure 3.6). Obviously both the columns, being placed in the same oven, are subjected to the same thermal profile, thus allowing to carry out the two analyzes simultaneously.

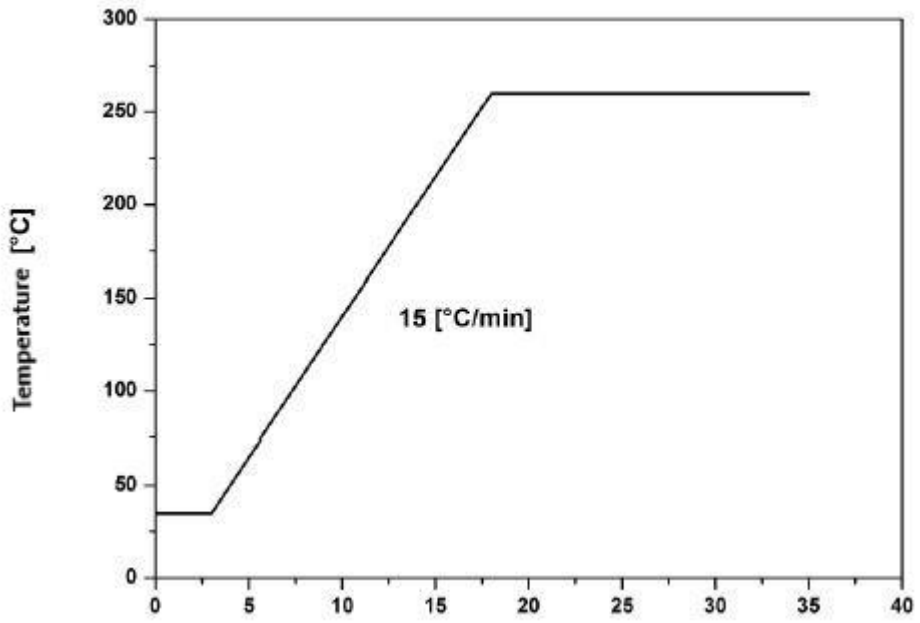

Figure 3.6: Temperature ramp during the on-line analysis with the columns plot and porapak.

Although the Porapak column allows the separation of several species, it is only used to detect CO_2 and CH_4. The molecular sieve column holds all the compounds that are not separated and for this must be subjected to periodic regeneration (T = 300 ° C, P-He = 3 bar for at least 12 hours). The gas chromatograph is equipped with a flame ionization detector (FID, Flame Ionization Detector) and a thermoconductive detector (TCD, Thermoconductive Detector). The molecular sieve columns and the Porapak column are connected to the TCD detector while only the Al_2O_3-plot column is connected to the FID.

The following are the standard chromatograms obtained with the three analysis columns (Figure 3.7).

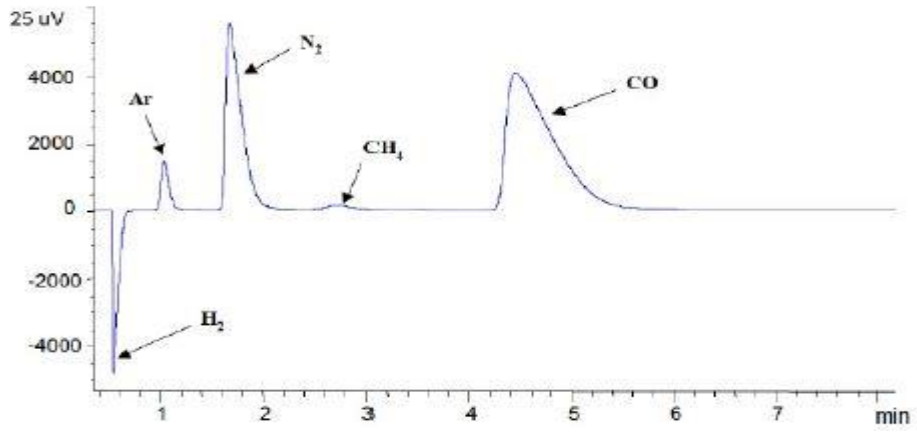

(a) Chromatogram obtained with the sieve column

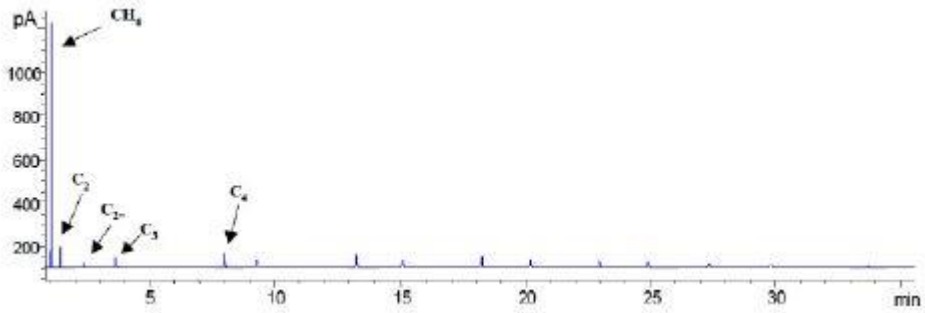

(b) Chromatogram obtained with the capillary column

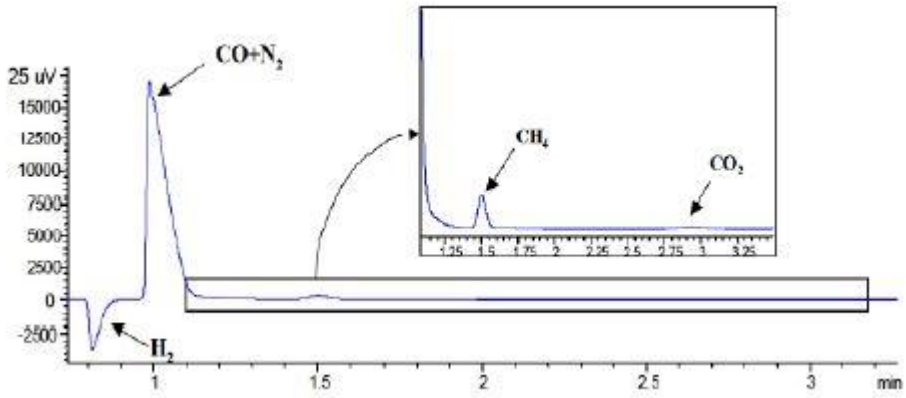

(c) Chromatogram obtained with the porapak column

Figure 3.7: Chromatograms obtained from different online analysis

As anticipated before, the reaction products in the gas phase and the unreacted gases are sent to the online gas chromatograph (HP model 6890) through a system of six-way sampling valves (Figure 3.8). The gas reaches the sampling valve A and then be sorted to the other three devices. The valves marked with the letters A, B and C are equipped with a calibrated charge coil, which allows to take a fixed quantity of gas to be analyzed equal to about 1 ml. During the analysis, the gas flows from valve A to B and then to C. The gas enters in each valve through the inlet marked with 1 and exits through the route marked with 2. The outlet of the valve C is connected to the totalizer. When the gas is sampled, the coil is charged by putting the way 1 in communication with the way 6. When the sampled gas is analyzed, the valve returns to the analysis position: the carrier gas (He) entering from the way 5 pushes the sampled gas through the way 4 and then goes into the column.

The valve D has the purpose of managing the flows eluted from the sieve and porapak columns by sending the desired column output to the TCD detector.

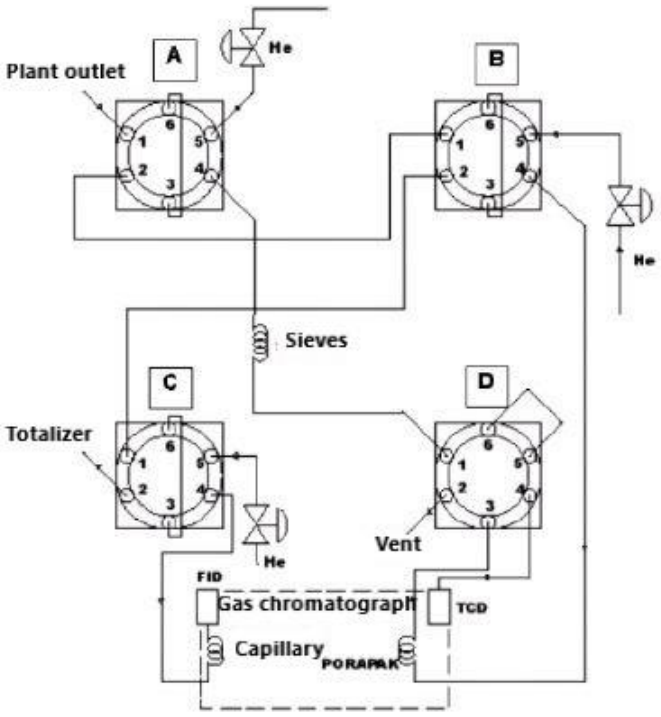

Figure 3.8: 6-way sampler valve.

3.4.2 Offline Analysis.

The liquid products are analyzed in an offline gas chromatograph (HP model 6890) equipped with two capillary columns HP 5 cross-linked 5% PH ME Siloxane with a length of 30 m, diameter 0.32 mm inside and active phase thickness equal to 0.25 μm. The columns are inserted inside the gas chromatograph oven and are subjected to a specific programmed temperature ramp. Injection of the samples in the column is carried out with an autosampler. The two columns are equipped with an on-column injector and a split / splitless injector respectively. The column equipped with an on-column injector is used for the waxes analysis, while the column with a split / splitless injector is used for the analysis of the aqueous and organic phases. Although both columns are inside the same oven, the analysis are not performed at the same time as each phase (aqueous, organic and wax) is analyzed with a different temperature ramp.

Table 3.3 shows the gas chromatograph operating conditions adopted for the analysis of the three phases.

Table 3.3: Gas chromatograph operating conditions for the three phases

Aqueous phase analysis	
Injector T [°C]	270
Column T [°C]	See scheduled for aqueous phase (3.9)
Upper column P [kPa]	170
Detector T [°C]	250
Organic phase analysis	
Injector T [°C]	270
Detector T [°C]	250
Column T [°C]	See scheduled for organic phase (3.10)
Upper column P [kPa]	170
Waxes analysis	
Injector T [°C]	270
Detector T [°C]	250
Column T [°C]	See scheduled for waxes (3.11)
Upper column P [kPa]	40

The temperature ramps adopted to analyze each phase are shown below.

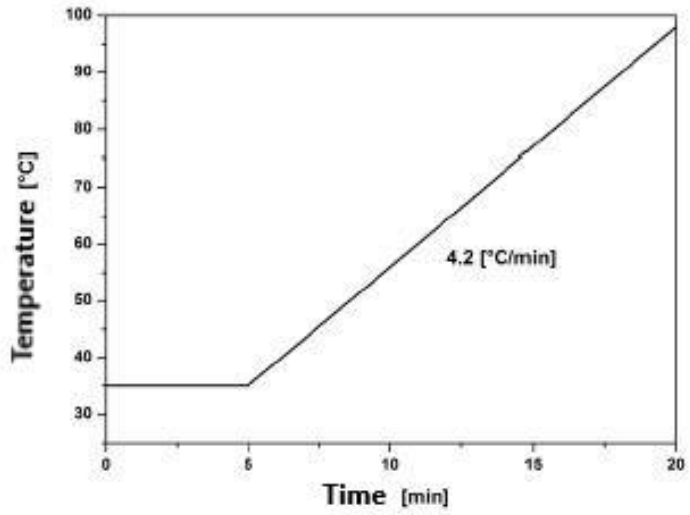

Figure 3.9: Temperature ramp set during the off-line analysis of the aqueous phase.

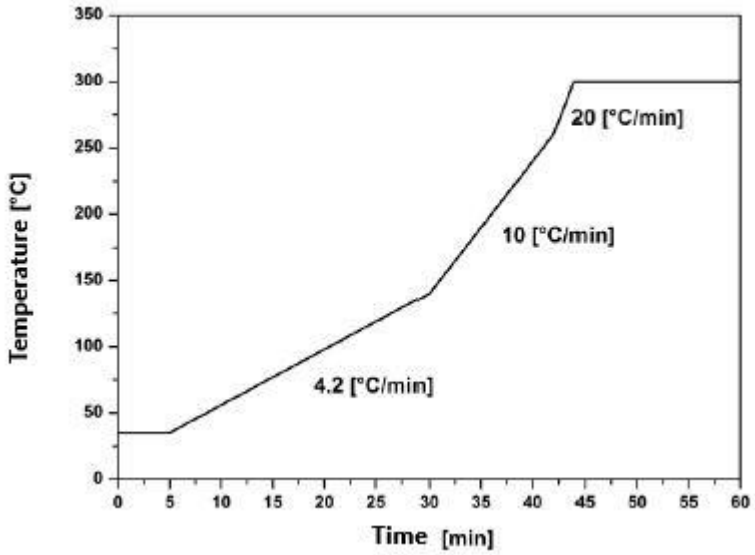

Figure 3.10: Temperature ramp set during the off-line analysis of the organic phase.

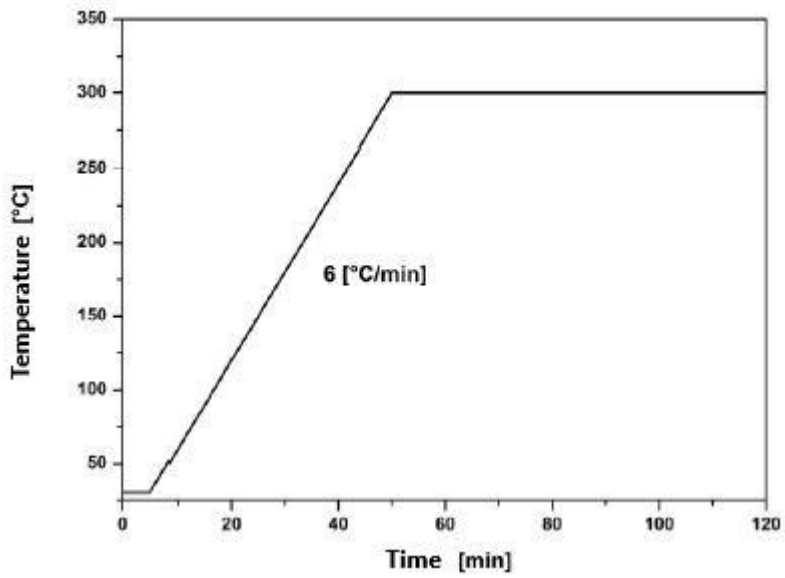

Figure 3.11: Temperature ramp set during the off-line analysis for the waxes.

The samples are prepared for the analysis according to the following procedure:

- Aqueous phase: The aqueous phase consists of alcohols dispersed in aqueous matrix. Since the water is not identifiable with an FID-type detector, it is necessary to prepare the sample by introducing an internal standard. The standard used is acetonitrile (CH3CN) as it generates an easily integrable peaks and does not interfere with alcohols. Then CH3CN is added in a quantity of 2 µl / g of aqueous solution to be analyzed and 1.4 µl of the solution obtained in the column is injected.
- Organic Phase: About 1 µl of solution is injected into the column and it is not necessary to introduce a standard. All the compounds present in this phase (paraffins, olefins and alcohols) are in fact identified by FID.
- Waxes: Once they have been extracted, they appear in solid phase which must then be dissolved in order to be injected. The procedure involves the dissolution of the sample (0.02 g) in carbon disulphide (CS2) (5 ml) and the injection of 0.5 µl of solution. The type chromatograms obtained with the three analysis columns are shown below (Figure 3.12)

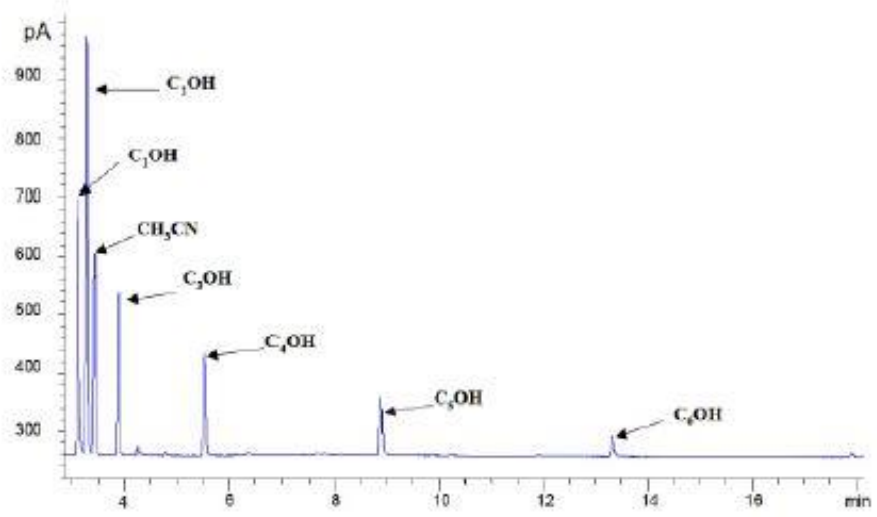

(a) Chromatogram obtained by analyzing the aqueous phase

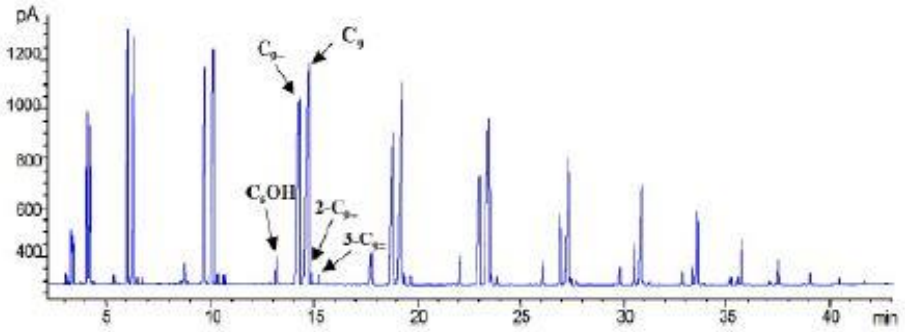

(b) Chromatogram obtained by analyzing the organic phase

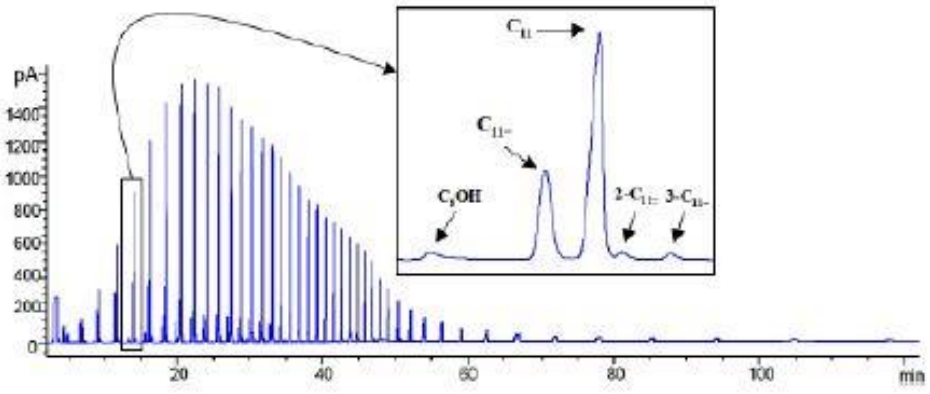

(c) Chromatogram obtained by analyzing the wax phase

Figure 3.12: Off-line analysis chromatograms for the individual phases

The species identified in the gas, liquid and solid phase are summarized in the Table 3.4.

Table 3.4: Identified species in gas, liquid, solid phase.

Phase	α - olefins	β – olefins	Paraffins	Alcohols	Others
Tail gases	C_1 - C_{20}	-	C_1 - C_9	-	CO,CO_2,H_2,N_2,Ar
Organic liquid	C_4 - C_{20}	C_6 - C_{12}	C_4 - C_{20}	C_3 - C_{14}	-
Aqueous liquid	-	-	-	C_1 - C_7	-
Waxes	C_6 - C_{17}	-	C_6 - C_{50}	C_7 - C_{22}	-

3.5 Start-up procedure.

Prior to the start-up of the plant, the reactor is loaded with the catalyst and the inert filling materials. This procedure is described in detail in Chapter 4.

Once the reactor is connected to the plant, it is necessary to check the tightness of the entire equipment, since it works under pressure and with toxic and flammable gases. The leak test is carried out at pressures higher than those used for the experimental run for more than 24 h.

Starting from the standstill conditions (electrical panel switched on, system at atmospheric pressure, cylinders closed, all valves closed), the operations adopted to turn on the plant are listed in Table 3.5.

Table 3.5: Start up procedure; valves numeration refers to P&I (Appendix A, Figure B.1)

Operation N.	Description
1	Opening of the instrumental area
2	Opening of CO / syngas, H_2, N_2tanks
3	Regulation of the delivery pressure at 40 bar for the tanks of CO / syngas, H_2, N_2
4	Opening of manual on-off valves V1, V9, V15 and V16
5	Positioning of the three-way valves implemented V26 and V27 on the main line (line of the B1 and B2 barrels)
6	Opening of the implemented on-off valves V3, V8, V11, V13, V47 and V48
7	Positioning of the manual three-way valves V54 towards the barrel B4, V24 towards the reactor and V57 towards the totalizer
8	Opening of manual on-off valves V53, V55, V51, V33 and V30
9	Opening of manual on-off valves V40, V41, V61 and V52
10	Switching on the cryostat (set-point 2 ° C, circulation speed of the maximum refrigerant fluid
11	Ignition of the control unit of the flow and back-pressure controllers and setting of the 'Remote set-point' mode in volts (this operation allows to set the set-point and acquire the instantaneous value of the individual variables directly from the controller placed in control room)
12	Switching on programmable multi-loop controllers

Once the plant is started, the reduction of the catalyst is performed. Indeed, the catalyst as it is prepared is in the oxide form, which is not active in the FTS. The reduction procedure is carried out with hydrogen at atmospheric pressure and at high temperature (400 ° C). The details are shown in Table 3.6. In particular, 5 $Nl/h/g_{cat}$ of hydrogen and 2.97 $Nl/h/g_{cat}$ of nitrogen are fed into the reactor and the temperature is increased up to 300°C with a heating ramp of 2°C / min. Once reached 300°C, the N2 flow is decreased up to a value of 1.5 $Nl/h/g_{cat}$ in 1 h. Then, the temperature is raised up to 400°C. The flow of nitrogen is gradually brought to zero and the temperature of 400°C kept constant for 17h 20min. After

this period of time, the system is returned to 160°C. Cooling from 400°C to 160°C is carried out under a flow of 3.33 Nl/h/g_{cat} of Nitrogen and 5 Nl/h/g_{cat} of hydrogen.

Table 3.6: Catalyst reduction steps.

Initial T [°C]	Final T [°C]	Slop-up [°C/min]	H_2 flux [Nl/h/g_{cat}]	N_2 flux [Nl/h/g_{cat}]	Time
20	300	2	5	2.97	2h 20’
300	300	-	5	1.5	1h
300	400	2	5	1.5	50’
400	400	-	5	0	17h20’
400	160	-	5	3.33	-

Once the catalyst is reduced, the procedures necessary to bring the reactor into FT running conditions begin:

1. The hydrogen flow is stopped;
2. The syngas flow (5 Nl/h/g_{cat}) is fed, very slowly (5 h);
3. The plant is pressurized up to a value of 25 bar (7 h).;
4. The temperature of the catalyst is increased up to 180°C with an heating ramp of 2 ° C/h
5. The N_2 flow is gradually lowered until it reaches 1.41 Nl/h/g_{cat} (7 h).

During the experimental runs, different temperatures or other process variables, such as pressure or gas hourly space velocity can be investigated.

3.6 References

[1] Ascon. *Manuale d'uso e di installazione stazioni serie AC10 - AC20 - AC30*. 1996

[2] National Instrument. *LabVIEW user manual*. 1996

[3] L. Lietti P. Forzatti. *Strumentazione industriale chimica, elementi di regolazione*. Vol. 1. Milano: CUSL, 2000

[4] F. Fiore. *Sintesi di Fischer-Tropsch su catalizzatori a base di Co supportato su allumina: studio di reattività e meccanismo di reazione*. Vol. Tesi di dottorato. Politecnico di Milano, 2005

Chapter 4

Intensification of heat transfer in Fischer-Tropsch reactors through the adoption of Al packed-foam

4.1 Introduction

The low-temperature Fischer-Tropsch synthesis (FTS) is the well-known catalytic reaction that involves the hydrogenation of carbon monoxide over cobalt metal centers and the formation of long-chain hydrocarbons and water [1]. In the last decade, the interest in the FTS was considerably renewed in view of exploiting both associated and remote natural gas fields to produce liquid fuels [2].

The FTS is a highly exothermic reaction with a standard reaction enthalpy of -165 kJ/mol. The heat removal from the reactor is thus a key issue for the development of an intensified reactor technology [3]. The local reaction temperature, in particular, is critical in controlling the process selectivity: it is well known that the methanation reaction has a high activation energy and becomes dominant at high temperatures. Accordingly, the FTS over cobalt- based catalysts can be safely carried out only at temperatures lower than 240°C. Besides, moderate temperatures are crucial to extend the catalyst life time and prevent thermal runaways. [3]

Both fixed-bed and slurry reactors are commonly used for the FTS at the industrial scale [3]. In slurry bubble column reactors (SBCRs), the well-mixed liquid phase results in nearly isothermal operation that allows running the process at higher CO conversions per pass. However, catalyst particles for these reactors must be optimized to resist mechanical stress

and attrition. An efficient filtration system must be also provided for the separation of the liquid products from the catalyst particles [3,4]. Furthermore, the SBCR technology has a low specific productivity, which makes it convenient only at a huge scale.

The multitubular fixed-bed reactor (MTFBR) configuration is also used at the industrial scale [5] since it has several advantages, such as concentration in plug flow, high catalyst holdup, no need for catalyst separation and easier scale-up. However, weaknesses related to mass and heat transfer and pressure drop need to be addressed in view of the process intensification [3,4,6]. Mass transfer limitations may occur since big catalyst particles should be used to limit pressure drop across the catalyst bed [7,8]. The eggshell catalyst configuration may represent a promising solution even if the volumetric active density in the reactor is reduced with respect to the adoption of uniformly impregnated catalyst pellets [7,8].

Concerning the heat removal issue, the dominant pathway of the heat transfer in a MTFBR is fluid-phase convection. Heat transfer by thermal conduction is, indeed, insignificant since only contact points are present among the catalyst particles and between the particles and the reactor walls [4]. This results in a non-isothermal operation of the reactor with the presence of hot-spots and strong axial and radial gradients along the catalyst bed. This, in turn, may lead to the worsening of the catalyst selectivity, to a fast catalyst deactivation, and in the worst case to the thermal runaway of the reactor [4].

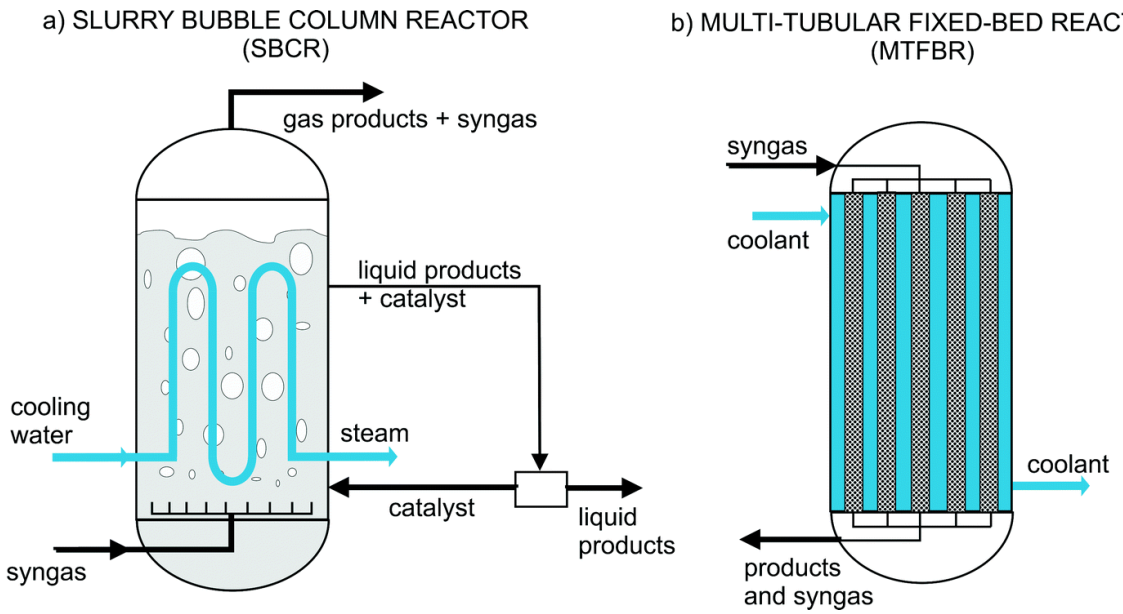

Fig. 4.1: Large scale Slurry-bubble column and Packed-bed LTFT reactors. [26]

At the industrial scale, such an issue is overcome by limiting the CO conversion per pass and recycling the unconverted syngas as well as a considerable fraction of the liquid reaction products at high flow rates. However, this increases pressure drops and makes the reactor less flexible to be scaled [6]. Concerning the latter issue, it has to be noted that the superficial velocity of the liquid phase trickling down the reactor is the key parameter governing the removal of the reaction heat and for this reason it has to be kept above a certain value to guarantee the reactor operability. As a consequence, scaling down the reactor by decreasing the tube length (e.g. in view of the development of compact scale FT reactors for off-shore applications) would require to keep the amount of recirculated liquid phase almost unchanged, thus making the process potentially unfeasible. [3]

Nowadays, several research groups are focusing on the development of structured reactors with an improved thermal management suitable for small-scale GTL applications for remote or stranded gas sources [4,6,9-17].

In this regard, microchannel-based FT reactors are now commercially offered by Velocys [18]. The reactor is demonstrated to deliver approximately 175 barrels of FTS products per

day [18]. The microchannel-design requires that the catalyst is housed within wave-like fin structures. The reaction heat is efficiently removed by the pressurized water coolant flowing within cross-flow microchannels [18]. A major issue of the microchannel system is the fact that it introduces a totally new reactor technology, which is intrinsically more complex and expensive in comparison to the conventional multitubular fixed-bed reactor, a proven workhorse of the Chemical and Process Industry for the last several decades.

Fig. 4.2: Segment of a microchannel (left) and a three microchannels FT reactor within a pressure vessel (right) with Velocys approach. [27]

To date, different conductive structured catalysts with different geometries were proposed as viable alternatives for the MTFBR applications [4,6,9-17]. In this regard, promising results are obtained when the catalytic material is no longer randomly packed but rather washcoated onto a spatially structured support made of conductive materials [4,6,9-15]. This enables more isothermal operation of the reactor, thus reducing the presence of hot spots and its consequences.

Different metallic supports with different geometries, such as Al-foams and honeycomb monoliths with different cell densities and made of both Fecralloy and Al, were widely

studied for the FTS by Montes and coworkers at the University of the Basque Country [4,9,10].

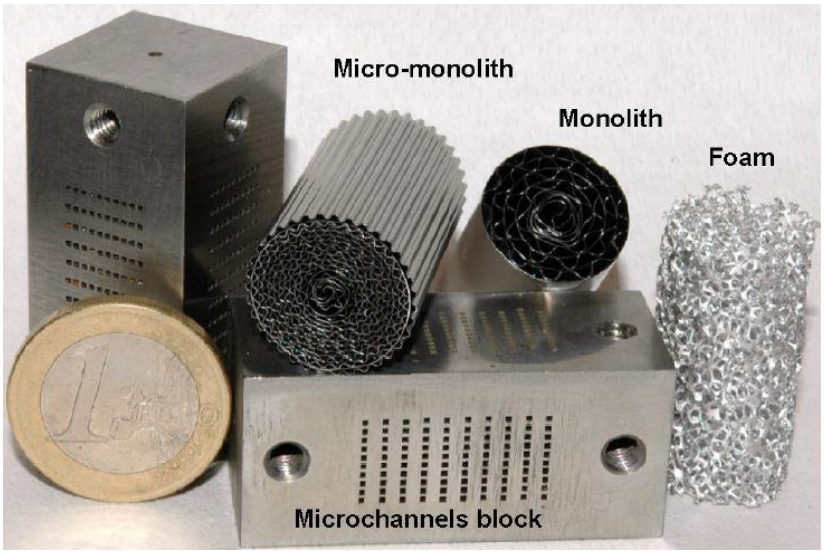

Fig. 4.3: Microstructured support studied at the University of Basque Country. [10]

These monoliths are composed by alternated flat and corrugated foils and were in-house made, while foams were provided by ERG aerospace. They found that, regardless of the geometry, the adoption of metallic supports enables better performances than the corresponding powdered catalyst.

Structured support	Monolith	Micromonolith	Foam	Microchannels block
				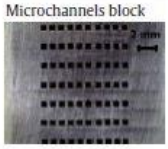
Geometric surf. (cm^2)	258	510	140	56
Hydraulic diameter (μm)	835	373	700	700
Porosity (%)	89	79	95	–
ppi (pores/$in.^2$)	–	–	40	–
cpi (cells/$in.^2$)	350	1180	–	–
Dimension				
⌀ (mm)	16	16	16	–
L (mm)	30	30	25	20

Fig. 4.4: Geometric characteristics of the different supports investigated. [9]

Among the structures, monoliths with high thermal conductivity (made of Al) and high cell density (2300 cpsi) show improved heat exchange capabilities, thus representing the most promising alternative to traditional packed-bed reactors [4]. On the contrary, the adoption of waschcoated foams seems to be less feasible with respect to the other substrates. This is mainly due to the several difficulties encountered during the coating process of the active phase onto these cellular structures. Furthermore, due to their low geometrical surface areas, very thick coatings are required to reach sufficient catalyst loadings. As a result of the coating process, some catalytic material may be retained, partially blocking the macropores of the foam [9].

The potential of coated conductive monoliths in the FTS was actively investigated in our group at Politecnico di Milano [3,6,19]. Visconti et al. [3] demonstrated through numerical simulations the ability of these substrates to manage the heat removal issue of the FTS and to guarantee an excellent temperature control. The heat transfer is strongly enhanced because the primary radial heat exchange mechanism is changed from convection to conduction within the thermally connected solid matrix of the honeycomb monolith [3,19].

Another alternative concept of catalyst structures with enhanced heat transfer characteristics is represented by the conductive micro-fibrous entrapped catalysts (MFEC) developed by the Tatarchuk group at Auburn University, USA.

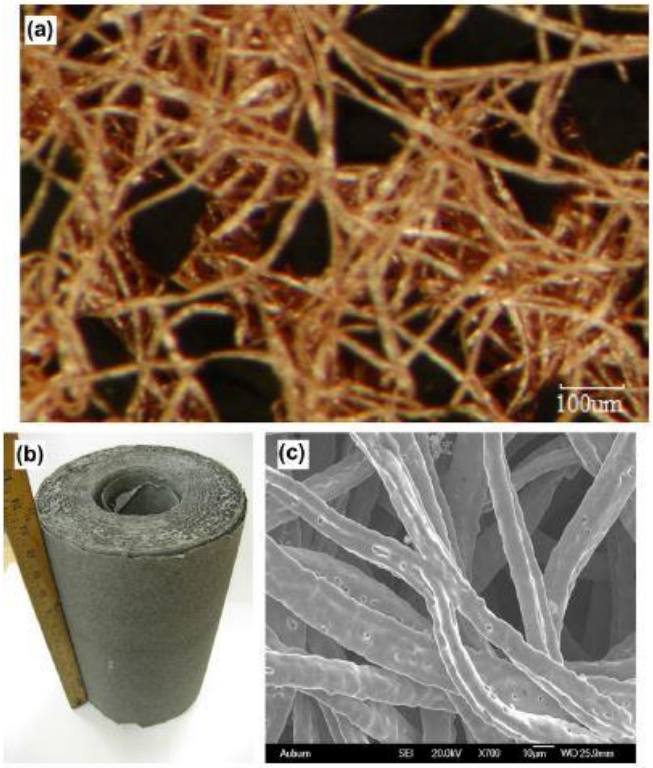

Fig. 4.5: Pictures of MFECs; (a) 12-lm Cu MFEC with FTS catalyst particles, (b) nickel MFEC roll by paper-making machine, (c) bonding junctions of copper fibers in sample (a). [13]

They consist of sintered micron-sized metal fibers entrapping small catalyst particles [12,13]. Flow heat transfer experiments over such micro-fibrous entrapped catalysts made of conductive metals provide much greater effective thermal conductivities and wall heat transfer coefficients than comparative runs over conventional packed beds of particles. The adoption of MFEC allows running the FTS at CO conversion levels of 50-80% [12,13].

A micro-structured reactor technology composed by eight parallel catalyst sections sandwiched between cross-flow oil channels for heat exchange was also proposed by Myrstad et al. [11] at NTNU, Norway. Each catalyst section is made of two foils with an etched deep pillar structure. The foils are stacked opposite to each other giving 800 μm channel height. The authors show the capability of this system to efficiently remove the heat generated by a

highly active Co-based catalyst working under severe FTS conditions (high CO conversion levels ≈ high reaction heats) [11].

In view of the development of compact and intensified Fischer–Tropsch reactors, packed closed cross flow structures (CCFS) were recently proposed by Kapteijn and coworkers in Delft [16,17]. CCFS consist of superimposed inclined corrugated sheets separated by flat sheets. It was numerically shown that the structured flow paths of the fluids through the packing roughly double the overall heat transfer properties of a randomly packed bed reactor. Furthermore, despite of a lower catalyst hold-up, the packed CCFS has a 25% higher C_{5+} productivity per reactor volume than the packed-bed [16,17].

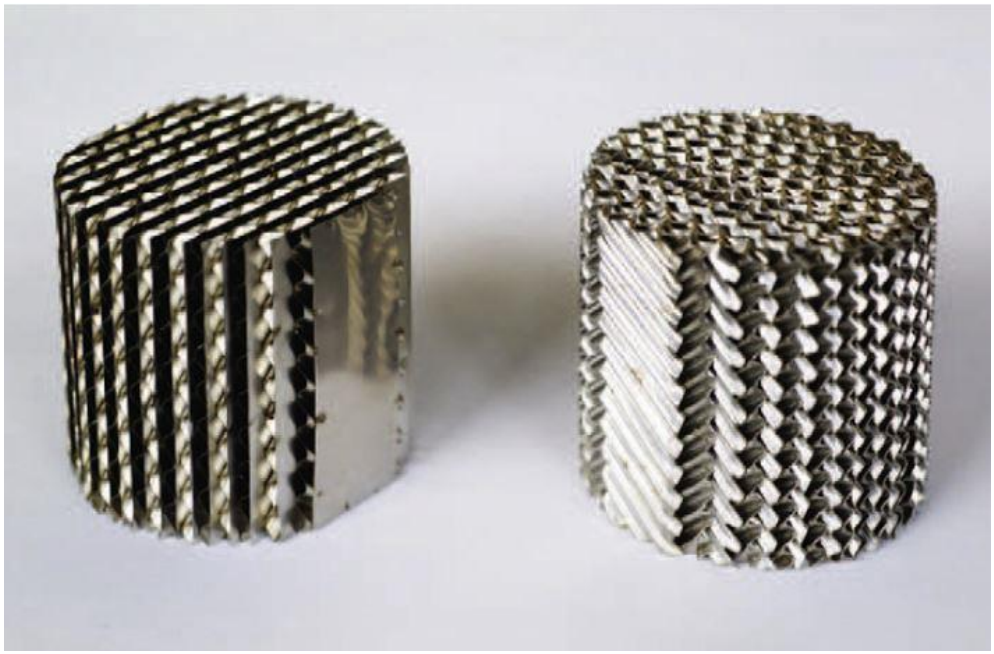

Fig. 4.6: Closed Cross Flow Structured (CCFS) packing used in Delft. [16]

In this thesis work, we propose to enhance the heat transport properties of a FTS fixed bed reactor through the adoption of highly conductive open-cell metal foams packed with catalyst pellets. These materials have been recently proposed by our group as a strategy to intensify heat transfer in strongly endo- and exo-thermic catalytic processes in tubular reactors [20-22].

Open-cell metal foams are particularly attractive structures since they have high porosity, low density, high mechanical strength and large surface area. They can be made of highly thermal conductive metals, such as Al or Cu. Combined with their continuous thermally connected structure, this may offer a good potential for the improvement of the heat transfer properties of a FTS packed-bed reactor [20-22]. Open-cell foams in fact exploit the same conductive heat transfer mechanism of the monolithic substrates but, in addition, they have the advantage of enabling radial mixing within their structure, thus enhancing both the heat transfer and the flow uniformity [20-22].

While the adoption of conductive open-cell foams for the FTS has been proposed already [14, 23], the peculiarity of our concept, claimed in [20] and described for the first time in [21], is the adoption of open-cell foams "packed" with catalyst pellets. In particular, this is the first time in the scientific literature, to our knowledge, that activity tests over a catalyst in the form of small pellets randomly packed in the voids of a cellular foam are reported. The adoption of the packed-foam configuration also overcomes the inherently limited catalyst inventory of the washcoated structured reactors proposed so far. This allows boosting the productivity per reactor volume of the FT reaction.

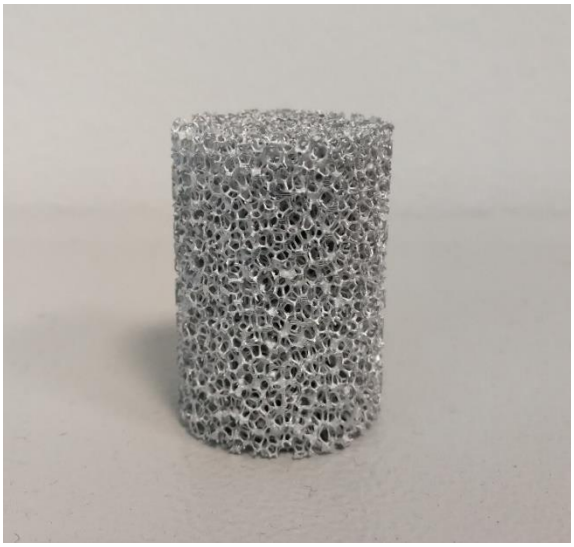

Fig. 4.7: Al highly conductive open-cell metal foam used in this thesis work.

4.2 Experimental

4.2.1 Catalyst preparation and characterization

A home-made $Co/Pt/Al_2O_3$ catalyst containing 18wt.% of Co and 0.1wt.% of Pt (nominal loadings) is prepared by following the procedure proposed by some of us in a recent publication [24]. The catalyst is supported on γ-Al_2O_3 microspheres (Sasol Puralox®, S_{BET}=145 m^2/g, V_{pore}= 0.45 cm^3/g) with an average pellets diameter of 300 μm. This pellet size is a rational compromise to prevent the onset of strong mass transfer limitations while granting low pressure drops at the same time [7-8]. The first step of the preparation method adopted is the stabilization of the γ-Al_2O_3 support with inactive cobalt aluminate species [2]. Then, Pt is impregnated on the stabilized support in a single incipient wetness impregnation (IWI) step. After that, the obtained material is impregnated four times with an aqueous solution of $Co(NO_3)_2 \cdot 6H_2O$ (Sigma Aldrich, 98.0 wt%), so to reach a Co loading of 18wt.%. Both the Pt and Co impregnation steps are followed by drying in static air at 120 °C for 2 h (heating rate 2 °C/min) and calcination at 500 °C for 4 h (heating rate 2 °C/min) [24].

The main properties of the $Co/Pt/Al_2O_3$ catalyst are here summarized in Table 1.

Table 4.1: Properties of $Co/Pt/Al_2O_3$ catalyst

BET area [m^2/g]	Pore volume [cm^3/g]	Co loading [wt.%]	Pt loading [wt.%]	dCo_3O_4 [nm]	dCo^0 [nm]	DOR [%]
59	0.20	22.80 ± 0.59	0.110 ± 0.002	21	9	100

Briefly, the BET area and pore volume of the calcined catalyst are 59 m^2/g and 0.20 cm^3/g, respectively. The effective catalyst composition obtained by ICP-MS analysis is in good

agreement with the nominal Co and Pt loadings of the catalyst. The average size of Co oxides and Co metal crystallites, determined by in-situ X-ray spectroscopy, are 21 and 9 nm, respectively. The degree of reduction (DOR) of the catalyst, monitored via in-situ magnetic measurements, is found to be 100% [24].

A deep characterization of the Co/Pt/Al_2O_3 catalyst obtained after calcination and during the reduction step carried out at the same process conditions used prior to the reactivity test (400°C for 17 h with a heating ramp of 2 °C/min using 5000 cm^3(STP)/h/g_{cat} of pure H_2) is shown in [24].

4.2.2 Packed-foam reactor with a catalyst density of 0.63 g/cm^3 (exp. a)

The open-cell aluminum foam with a nominal pore density of 40 ppi (ε_{foam}≈ 0.906; d_{cell}≈ 2 mm) was purchased from ERG Aerospace. As shown in Fig. 4.8, the shape of the foam is cylindrical with a length of 4 cm and a diameter of 2.78 cm, with tolerances of ± 0.030 cm. Notably, the diameter of the foam coincides with the internal diameter (I.D) of the stainless steel FT reactor used in the activity tests, so to ensure good contact and avoid dead space ("gap") between the tube and the cellular structure.

One axial through hole of 0.32 cm diameter is located at the centerline of the structure for the insertion of the stainless steel thermowell (1/8'' O.D.), protecting sliding J-type thermocouple (0.5 mm O.D.) (Figs. 4.8 and 4.10a).

Once the foam is loaded in the tubular reactor (Fig. 4.9) and the thermowell is put in place, the foam is packed as schematically shown in Fig. 4.11a. Initially, 5 g of α-Al_2O_3 pellets (d_{pellet}= 300 μm) are poured into the foam, thus filling 1 cm of the structure. Then, 7.2 g of Co/Pt/Al_2O_3 catalyst diluted with a very small amount of α-Al_2O_3 (catalyst:α-Al_2O_3 = 6:1 w/w) with the same granulometry are poured into the foam, reaching a length of the catalyst

bed of 2 cm. Eventually, 5 g of α-Al_2O_3 pellets (d_{pellet}= 300 μm) are packed into the foam so to fill the last 1 cm of the structure. The resulting catalyst volumetric density, calculated as ratio between the catalyst weight (7.2 g) and the reactor volume occupied by the foam (11.4 cm^3), is 0.63 g/cm^3.

The total amount of pellets loaded into the foam corresponds exactly to the amounts of pellets in a packed-bed with the same volume of the voids (cells) of the foam and ε_{PB} of 0.38. This clearly indicates that, probably due to the high dcell/dpellet ratio, the small pellets can uniformly fill the voids of the foam structure and negligible effects on the packing effectiveness are given by the presence of the struts of the foam.

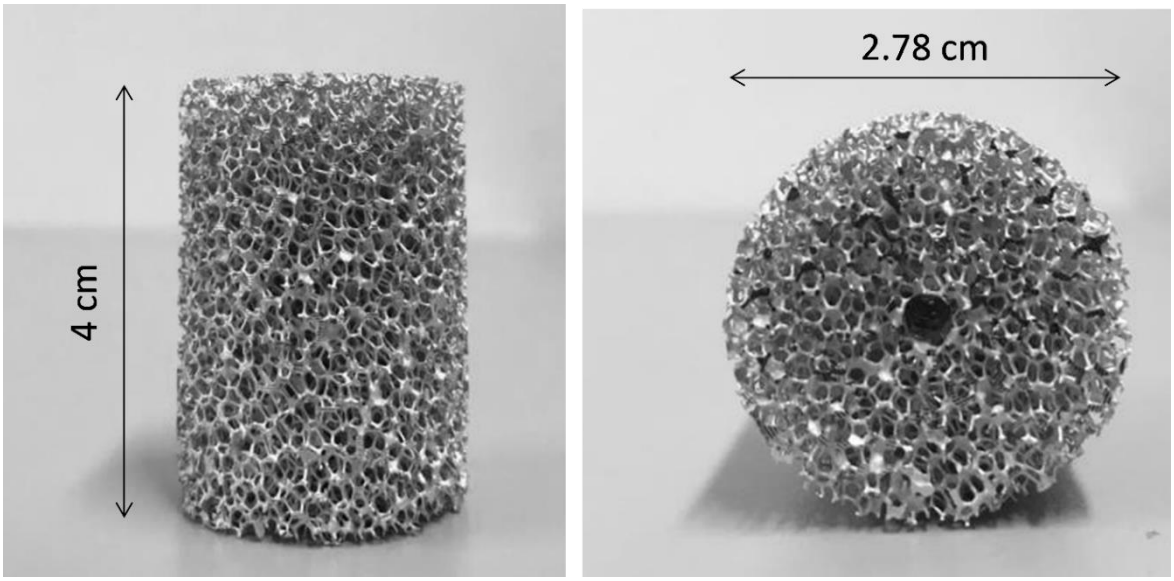

Fig. 4.8: Images of the open-cell aluminium foam used in exp a.

Fig. 4.9: Foam loading into the reactor.

4.2.3 Packed-foam reactor with a catalyst density of 0.75 g/cm^3 (exp b)

Open-cell aluminum foam with a nominal pore density of 40 ppi ($\varepsilon_{foam} \approx 0.888$; $d_{cell} \approx 2$ mm) is provided by ERG Aerospace. As shown in Fig. 4.10, the shape of the foam is cylindrical with a length of 2 cm and a diameter of 2.78 cm. (già detto sopra)

One axial through hole of 0.32 cm diameter is located at the centerline of the structure for the insertion of the stainless steel thermowell (1/8'' O.D.), protecting sliding J-type thermocouple (0.5-mm) (Figs. 4.10 and 4.11b).

Once the foam is loaded in the tubular reactor and the thermowell is put in place, the foam is packed as schematically shown in Fig. 4.11b. In particular, 9.0 g of pure Co/Pt/Al_2O_3 catalyst are poured into the foam, ensuring the complete filling of the 2 cm length of the foam. The obtained catalyst volumetric density is 0.75 g/cm^3.

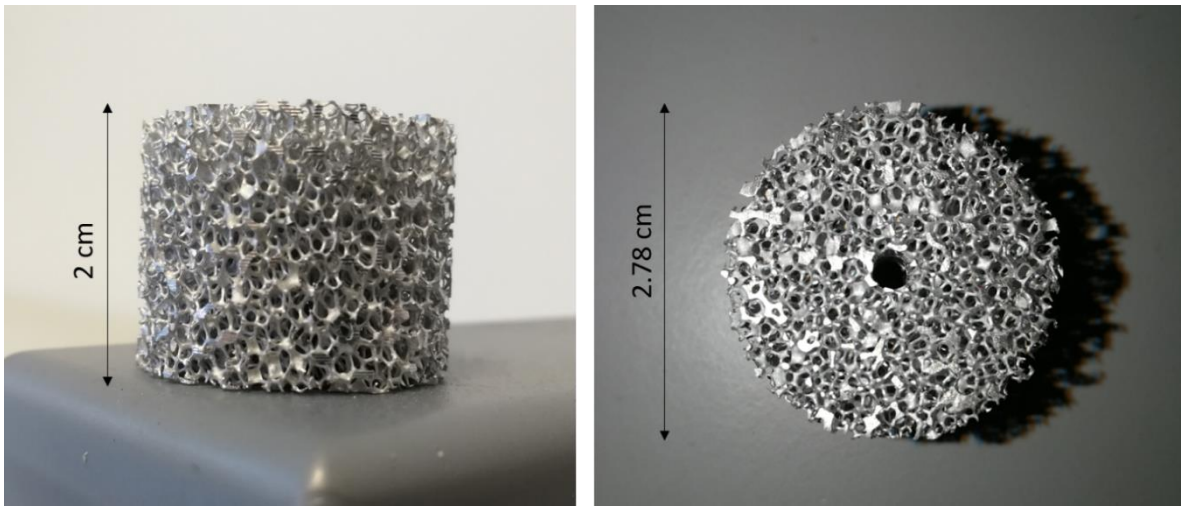

Fig. 4.10: Image of the open-cell aluminium foam used in exp b.

4.2.4 Packed-bed reactor

In the case of the packed-bed reactor, 7.2 g of Co/Pt/Al_2O_3 catalyst are randomly packed in the same reactor used for the foam but diluting with a large amount of α-Al_2O_3 (catalyst:α-Al_2O_3 = 1:1.7 w/w) pellets with the same granulometry (d_{pellet}= 300 μm). In this way, looking at the Fig. 4.11c it is possible to notice that the length of the catalyst bed is kept equal to the length of the foam (≈ 4 cm), while the catalyst volumetric density is halved (≈ 0.29 g/cm^3) if compared with that of the packed-foam reactor, so to operate under milder process conditions.

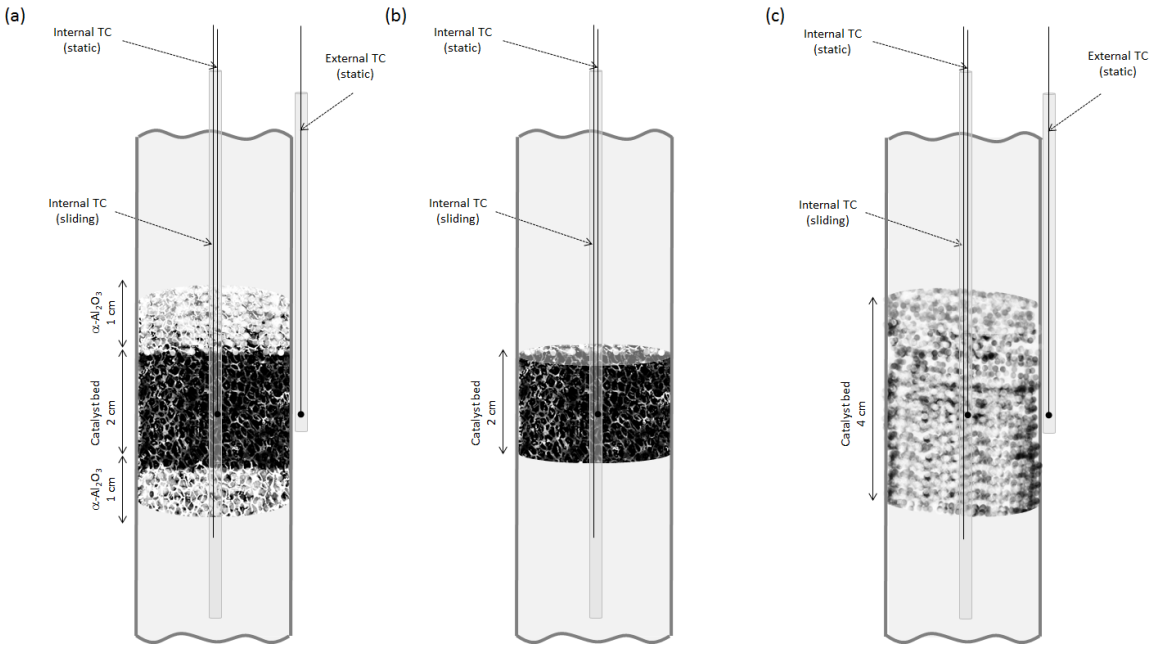

Fig. 4.11: Scheme of the reactor packed with foams (a) exp. a, (b) exp. b and (c) the randomly packed-bed reactor (TC= thermocouple)

4.2.5 Catalytic tests

The structured catalysts and the packed-bed are tested in the FTS in a fully automated lab-scale rig [25] equipped with a stainless-steel tubular fixed-bed reactor 2.78 cm I.D., 85 cm long inserted in a three-zone split tube furnace (Carbolite, TVS/600).

Downstream the reactor the unreacted reactants and the reaction products pass a first vessel kept at 150 °C for waxes condensation and a second vessel cooled at 1 °C for the separation of liquid aqueous and organic products.

Incondensable gases leaving the vessels are periodically analyzed by an on-line GC (HP 6890) equipped with three columns and two detectors for the analysis of C_1–C_9 hydrocarbons (Al_2O_3-plot capillary column connected to a FID), of H_2, CH_4 and CO (molecular sieve column connected to a TCD) and of CO_2 (Porapak Q column connected to the same TCD detector). Condensable reaction products are periodically analyzed by an off-line GC (HP

6890) equipped with two FIDs and two HP-5 crosslinked 5% PH ME Siloxane capillary columns. This analytical procedure allows the detection of C_1–C_{49} hydrocarbons.

FTS runs were carried out at 180-240 °C, 25 bar, H_2/CO inlet molar ratio= 2.0, GHSV= 6410 cm^3(STP)/h/g_{cat}, inerts (N_2+ Ar) in the feed= 24 vol.% for more than 1000 h on stream.

Prior to exposing the sample to syngas, the catalyst is reduced in situ at 400 °C (heating ramp= 2 °C/min) for 17 h using 5000 cm^3(STP)/h/g_{cat} of H_2 (Sapio, 99.995 mol.%) at atmospheric pressure.

Process conditions are never changed before steady-state conditions are reached for both the catalysts activity and selectivity. In order to verify the achievement of steady state conditions, multiple data at the same experimental condition are collected for more than 24 consecutive hours.

The reactant conversion and the C_1–C_{49} products distribution (C_1–C_{49} paraffins, C_2–C_{17} olefins, CO_2) are periodically monitored during the experiments. Data are considered steady when the CO conversion (X_{CO}[%], eq. (4.1)) and the selectivity (S_i[%], eq. (4.2)) to the main FTS products varied within less than 5% in 24 h.

The catalyst stability is verified by comparing the catalyst performances measured at 200 °C, 25 bar, H_2/CO inlet molar ratio = 2, GHSV = 6410 cm^3(STP)/h/g_{cat}, inerts (N_2 + Ar) in the feed = 24 vol.%) at different Time on Stream (T.o.S.). These process conditions are defined as "standard conditions".

Carbon balances, calculated as moles of C contained in the reaction products divided by the moles of CO converted, always close within ±10%, being typically within ±5%.

$$X_{CO}\,[\%] = 1 - \frac{F_{CO}^{out}}{F_{CO}^{in}} \cdot 100 \qquad [4.1]$$

$$S_i\,[\%] = \frac{F_i^{out} \cdot n_i}{\sum_i^{NP}(F_i^{out} \cdot n_i) + F_{CO2}^{out}} \cdot 100 \qquad [4.2]$$

F_i^{out} is the molar productivity of the ith hydrocarbon species, F_{CO}^{in} is the flowrate of CO sent to the reactor, n_i is the carbon atom number of the ith species and NP (= 49) is the number of carbon atoms in the heaviest hydrocarbon identified at the reactor outlet. The selectivity to carbon dioxide was calculated as in eq. (4.3):

$$S_{CO2}\,[\%] = \frac{F_{CO2}^{out}}{F_{CO}^{in} - F_{CO}^{out}} \cdot 100 \qquad [4.3]$$

The specific productivity for C_{5+} hydrocarbons (Y_{C5+}) is calculated as in eq. (4.4), where MW_i is the molecular weight of the ith species and w_{cat} the catalyst weight:

$$Y_{C5+}\,[g/h/g_{cat}] = \frac{\sum_{i\geq5}^{NP}(F_i^{out}\,MW_i)}{w_{cat}} \qquad [4.4]$$

The reaction heat released during FTS per surface of the foam (Q) is calculated according to eq. (4.5):

$$Q\,[W/m^2] = \frac{\Delta H_R^0 \cdot F_{CO}^{in} \cdot X_{CO}}{A_{foam}} = \frac{\Delta H_R^0 \cdot F_{CO}^{in} \cdot X_{CO}}{\pi \cdot d_{foam} \cdot h_{foam}} \qquad [4.5]$$

where ΔH_R^0 is the standard reaction enthalpy set to -165 kJ/mol and A_{foam} is the foam surface area.

Axial temperature profiles along the catalyst bed are measured by sliding the thermocouple inserted into the corresponding thermowell located at the centerline of the reactor, i.e. centerline of the catalyst bed (Fig. 4.11). The axial temperature gradient (ΔT_{cat}) is defined as the difference between the maximum and the minimum temperature recorded along the

catalyst bed. Another stainless steel thermowell (1/8'' O.D.), protecting a static J-type thermocouple (0.5 mm O.D.), is located at the outer wall of the reactor tube (T_{ext}), in correspondence of the center of the catalyst bed (Fig. 4.11). The external temperature gradient (ΔT_{ext}) is defined as the difference between T_{ext} and the temperature reading at the center of the catalyst bed.

Prior to the activity tests, a blank test was carried out at 200 °C, 25 bar, H_2/CO inlet molar ratio= 2, GHSV= 6410 cm^3(STP)/h/g_{cat} and inerts (N_2 + Ar) in the feed = 24 vol.%, so to identify the isothermal zone of the tubular reactor where locating the catalyst. To this end, the reactor was loaded with inert α-Al_2O_3 pellets and axial temperature profiles were measured along the reactor. A temperature difference lower than of 0.5 °C was obtained in 10 cm of the tube. Furthermore, no differences were noted between T_{ext} and the temperature reading at the center of the reactor (i.e. $\Delta T_{ext} \approx 0$ °C).

4.3 Results and discussion

4.3.1 Packed-foam reactor with a catalyst density of 0.63 g/cm^3 (exp a)

The performances of the packed-foam reactor loaded as schematically shown in Fig. 4.11 (a) are shown in terms of CO conversion (Fig. 4.12) and selectivity to the main FTS products (Table 4.2). Concerning the latter, no information about the products distribution is obtained at 180, 190, 215, 230 and 240 °C because more than 24 h are needed to collect representative liquid products.

All the results are reported as a function of the time on stream (T.o.S.). The catalyst activity is investigated for several hours (≈ 800 h) in a wide range of reaction temperatures between 180

and 240 °C. When the temperature is varied, the other operating conditions are kept constant: P= 25 bar, H_2/CO^{in} = 2 mol/mol, GHSV= 6410 cm^3(STP)/h/g_{cat}, inerts= 24 vol.%.

As shown in Fig. 4.12, the catalyst is already active at temperatures lower than those conventionally used for the FTS (< 200 °C). In particular, the CO conversion measured at 180 and 190 °C was 3.7 and 7.8%, respectively, while it reached 12.1% at 195 °C. This clearly indicates the high activity of the adopted Pt-promoted catalyst. When the standard conditions were reached (T= 200 °C), the CO conversion was 16.5% (Fig. 4.12). The selectivities to CH_4, CO_2, C_2-C_4 and C_{5+} at 200 °C were 10.9, 0.6, 13.8 and 70.6%, respectively (Table 4.2).

Upon increasing the temperature from 205 to 210 and then to 215 °C, the CO conversion grew from 21.2 to 28.1 and then to 33.5% (Fig. 4.12). The CH_4 selectivity increased in the same T-range from 14.6 to 17.3 and to 19.6% (Table 4.2).

High CO conversions were obtained at temperatures above 215 °C: the catalyst reached 44.7% of CO conversion at 220 °C, and 50.3 and 54.5% at 225 and 230 °C, respectively. At 240 °C, it reached 67.5% (Fig. 4.12). The CH_4 selectivity followed the same trend with values of 21.0, 23.5, 27.5 and 33.3% at 220, 225, 230 and 240 °C, respectively (Table 4.2).

The selectivity to CO_2 increased by increasing temperature, going from a negligible value of 0.5% calculated at 195 °C to a high value of 7.1% estimated at 240 °C. This can be explained with the increase of the WGS activity of the catalyst at high CO conversion and hence at high-water concentration levels. Indeed, water is the most abundant reaction product as oxygen atoms of CO are predominantly rejected in this form.

The selectivity to C_2-C_4 and C_{5+} hydrocarbons, as well as the selectivity to C_2-C_{17} olefins, was also significantly influenced by the reaction temperature (Table 4.2).

The selectivity to C_2-C_4 increased from 11.5 to 16.0% when the temperature was increased from 195 to 225°C (Table 4.2).

The selectivity to C_{5+} hydrocarbons decreased upon increasing the temperature, going from 67.4 and 65.2% calculated at 205 and 210°C, respectively, to 59.3 and 56.3% estimated at 220 and 225°C (Table 4.2). These results are confirmed in Fig. 4.13, showing the typical Anderson–Schulz–Flory plot calculated at different temperatures. The ASF distributions has the typical positive and negative deviations for methane and C_2 hydrocarbons, respectively, and a change of slope for a carbon number around 8. The chain growth probability (α_{C15+}), estimated by considering the hydrocarbons with more than 15 carbon atoms, followed the same trend of the C_{5+} selectivity. In particular, α_{C15+} was 0.88 at 195 °C and around 0.87 at 200, 205 and 210 °C, and dropped to 0.84 at 220 and 225 °C (Fig. 4.13).

The olefin content in the products decreased upon increasing temperature. Accordingly, the selectivity to C_2-C_{17} olefins strongly decreased from 19.2 to 4.6%, increasing the temperature from 195 to 225 °C. In line with this result, the propylene to propane ($C_3^{//}/C_3$) ratio decreased from 1.2 to 0.2 by increasing temperature from 195 to 225 °C (Table 4.2).

These results are a clear evidence that high temperatures result in high catalyst activity. However, the increase of the temperature has a negative effect on the FTS products distribution since it results shifted to the undesired light hydrocarbons. This can be explained with the fact that the hydrogenation rate is favored by increasing temperatures, thus favoring the termination step rather than the growth step in the FTS chain growth mechanism [2].

The productivity of C_{5+} hydrocarbons (Y_{C5+}) is plotted in Fig. 4.14 as a function of the reaction temperature. It grows upon increasing the temperature, indicating that the positive effect of the reaction temperature on the catalyst activity prevails on the observed negative effect on the products selectivity.

The reaction heat released (Q) per surface of the foam during the test increases with temperature (Table 2), since it is strictly linked to the CO conversion. It starts from 276.4 W/m^2 obtained at 180 °C, up to a very high value of around 4664.6 W/m^2 at 240°C. Notably,

the reaction heat released at 230-240 °C may even be underestimated since the process selectivity is more shifted towards light hydrocarbons, especially CH_4 (S_{CH4}= 27.5-33.3%). This results in an underestimation of the standard reaction enthalpy used in the calculation of Q.

To our knowledge, this is the first time in the scientific literature that such high-values of the FTS reaction heat are reached in a lab-scale apparatus.

Fig. 4.15 shows the axial temperature profiles measured on the packed-foam at different temperatures (180-240°C). Limited T-profiles along the catalyst bed are obtained at all the temperatures investigated, thus resulting in very small T-gradients. In this regard, the ΔT_{cat} is negligible at 180 and 190°C, in line with the very low catalyst activity. Also in the T-range 195- 205 °C, it is small ($\Delta T_{cat} \approx 1$ °C) although the CO conversion level increases up to 22%. Increasing the reaction temperature up to 210 and then to 215 °C, the T-gradients result only slightly affected, with a ΔT_{cat} of 2 and 3°C, respectively. We recall that the CO conversion values at these temperatures are 28 and 33%, respectively. At 220 and 225 °C with significant CO conversions of 44 and 50%, the ΔT_{cat} is still small and equals 4 and 4.5 °C, respectively. The most significant effect on the ΔT_{cat} is obtained at 230 and 240 °C when the CO conversion reaches the highest values (55 and 67.5%). Accordingly, the ΔT_{cat} is 5 and 6 °C, respectively.

Also the external temperature gradient (ΔT_{ext}) increases almost linearly with the increase of the reaction heat release (Fig. 4.16). This is in line with the exothermicity of the reaction.

All the results shown in this work are a clear evidence of the efficacy of the highly conductive packed-foam configuration in removing the heat generated by the strongly exothermic FTS. These results clearly indicate that also under severe conditions (i.e. high reaction heat release) the adoption of the packed-foam reactor allows running the process with an outstanding temperature control.

Noteworthy, although the catalyst was tested for several hours (≈ 800 h), which is unusual for lab-scale catalyst activity tests and frequently varying the process conditions, it was found to be very stable with the Time on Stream (T.o.S.) (Fig. 4.12). Accordingly, the CO conversion measured by replicating the standard conditions at different T.o.S. (200, 520 and 760 h) was always around 16%. This is particularly interesting since the catalyst worked under severe conditions (i.e. high P_{H2O}/P_{H2} in particular in the second half of the catalyst bed [2]) for more than 200 h.

We believe that this is a further indication of the excellent heat transfer properties of the packed foam reactor, which prevents the deactivation of the catalyst by avoiding strong temperature gradients along the catalyst bed.

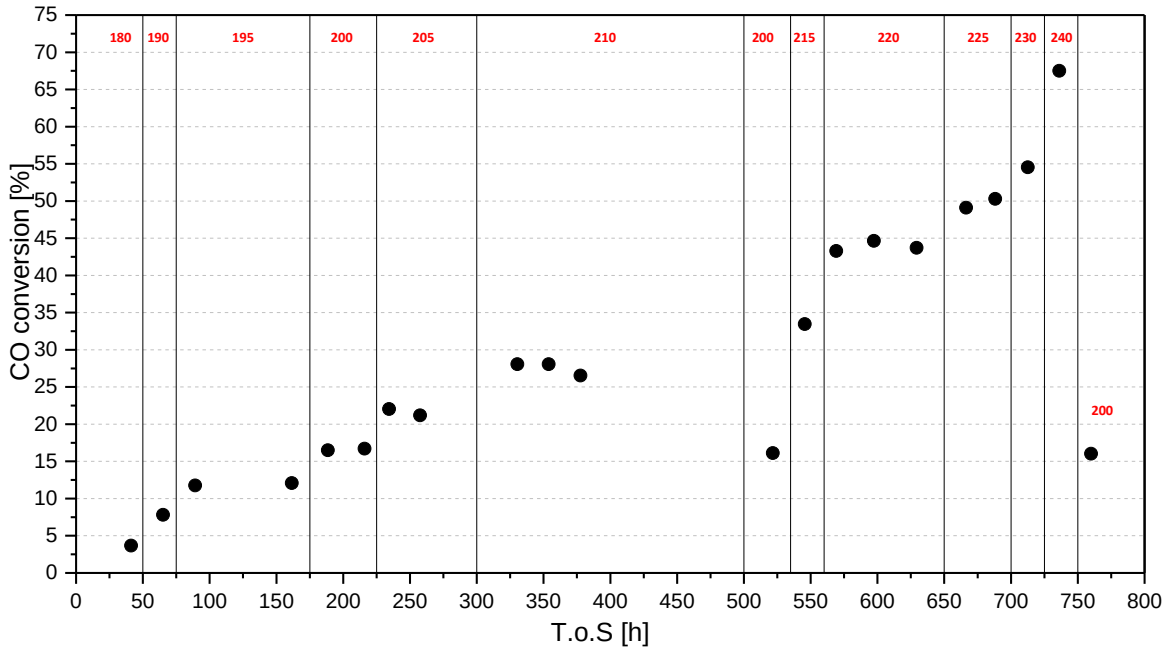

Fig. 4.12: Evolution of the CO conversion with time on stream (T.o.S.) at different temperatures (marked in red on the top of the graph).

P= 25 bar, H_2/CO^{in}= 2 mol/mol, GHSV= 6410 cm^3(STP)/h/g_{cat}, inerts= 24 vol.%.

Table 4.2: Main FTS Products at different temperatures.

P= 25 bar, H_2/CO^{in}= 2 mol/mol, GHSV= 6410 cm^3(STP)/h/g_{cat}, inerts= 24 vol.%.

T.o.S. [h]	T [°C]	X_{CO} [%]	S_{CH4} [%]	S_{CO2} [%]	S_{C2-C4} [%]	S_{C5+} [%]	$S^{olefins}$ (C_2-C_{17}) [%]	$C_3^{//}$ / C_3 [-]	Q [W/m^2]
162	195	12.1	8.4	0.5	11.5	76.6	19.2	1.2	836.2
216	200	16.5	10.9	0.6	13.8	71.6	15.1	0.8	1140.2
258	205	21.2	14.6	0.8	14.2	67.4	12.0	0.6	1465.0
378	210	28.1	17.3	1.0	14.5	65.2	8.4	0.4	1941.9
546	215	33.5	19.6	1.4	-	-	-	-	2315.0
597	220	44.7	21.0	2.0	15.4	59.3	6.0	0.3	3089.0
688	225	50.3	23.5	2.8	16.0	56.3	4.6	0.2	3476.0
713	230	54.5	27.5	3.8	-	-	-	-	3766.2
736	240	67.5	33.3	7.1	-	-	-	-	4664.6

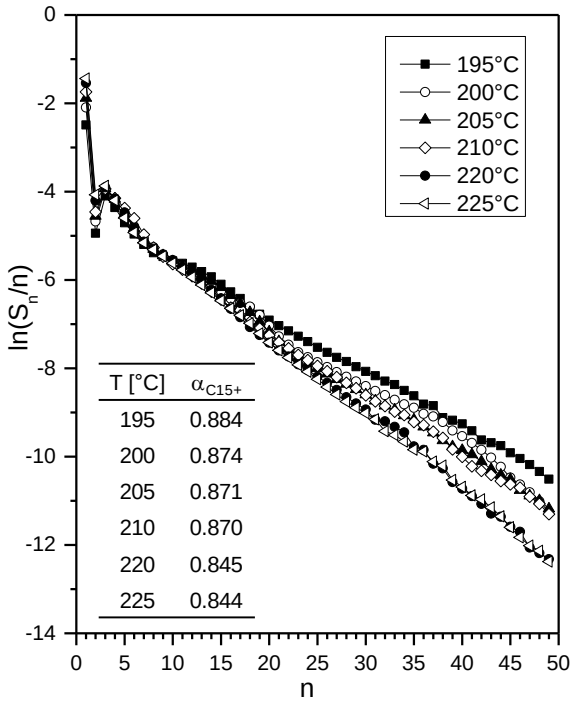

Fig. 4.13: Hydrocarbons ASF plots and α_{C15+} calculated at 195, 200, 205, 210, 220 and 225 °C.

P= 25 bar, H_2/CO^{in}= 2 mol/mol, GHSV= 6410 cm^3(STP)/h/g_{cat}, inerts= 24 vol.%.

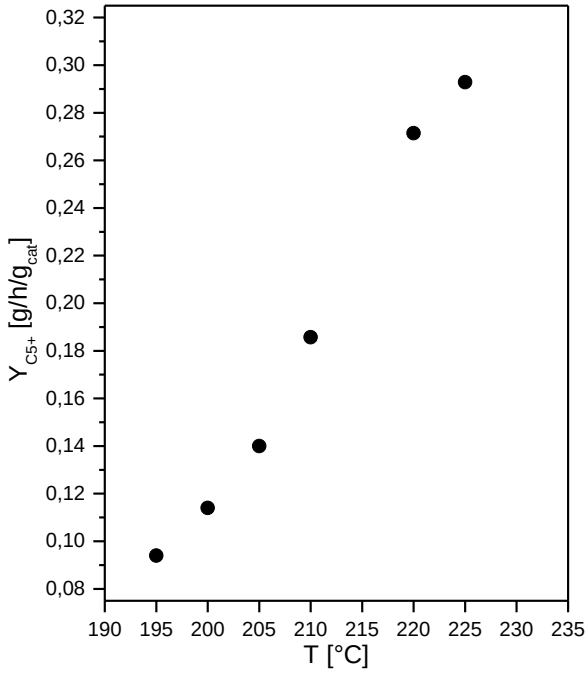

Fig. 4.14: Productivity of C_{5+} hydrocarbons as a function of the reaction temperature.

P= 25 bar, H_2/CO^{in}= 2 mol/mol, GHSV= 6410 cm^3(STP)/h/g_{cat}, inerts= 24 vol.%.

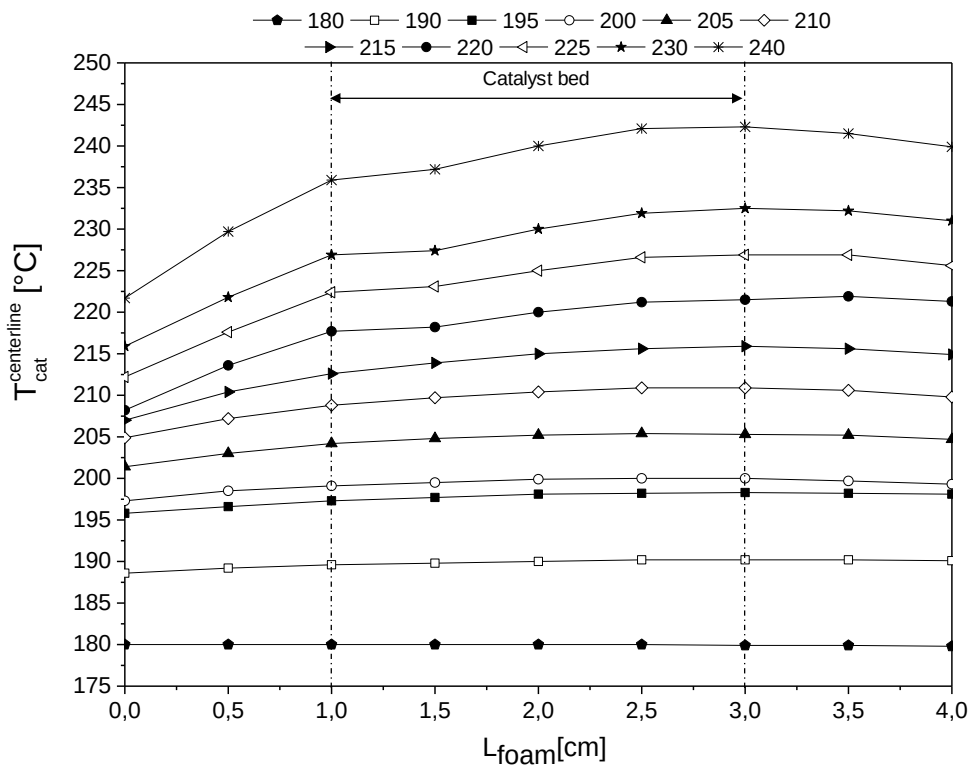

Fig. 4.15: Axial temperature profiles measured at different temperatures (T= 180, 190, 195, 200, 205, 210, 215, 220, 225, 230 and 240°C) of the packed foam(a) reactor. The catalyst bed length is also shown.

P= 25 bar, H_2/CO^{in}= 2 mol/mol, GHSV= 6410 cm^3(STP)/h/g_{cat}, inerts= 24 vol.%.

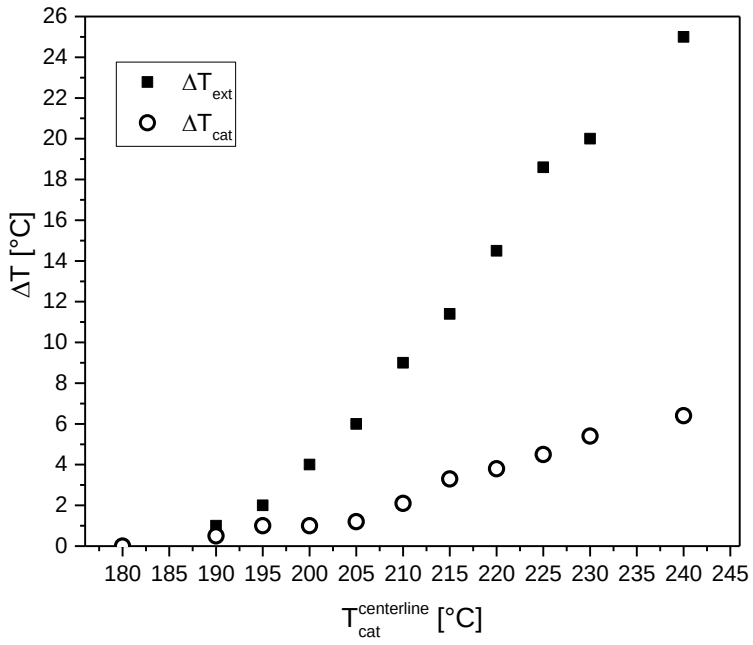

Fig. 4.16: Temperature gradients during FTS experiment.

P= 25 bar, H_2/CO^{in}= 2 mol/mol, GHSV= 6410 cm^3(STP)/h/g_{cat}, inerts= 24 vol.%.

4.3.2 Packed-foam reactor with a catalyst density of 0.75 g/cm^3 (exp a)

The performances of the packed-foam reactor loaded as schematically shown in Fig. 4.11 (b) are shown in terms of CO conversion (Fig. 4.17). All the results are reported as a function of the time on stream (T.o.S.). The catalyst activity is investigated for several hours (≈ 150 h) in a range of reaction temperatures between 180 and 200 °C. When the temperature is varied, the other operating conditions are kept constant: P= 25 bar, H_2/CO^{in} = 2 mol/mol, GHSV= 6410 cm^3(STP)/h/g_{cat}, inerts= 24 vol.%.

The CO conversion measured at 180 and 190 °C was 5.4 and 9.8%, respectively, while it reached 13.9% at 195 °C. When the standard conditions were reached (T= 200 °C), the CO conversion was 16.5% (Fig. 4.17). The fact that the CO conversion values are similar to those obtained in exp (a) (section 4.3.1) is a clear indication of the reproducibility of our

experimental runs. The selectivities to CH_4 and CO_2 at 200 °C were 14.0 and 0.6%, respectively (Table 4.3).

The reaction heat released (Q) during the test increases with temperature (Table 4.3), since it is strictly linked to the CO conversion. It starts from 909.7 W/m^2 obtained at 180 °C, up to a very high value of around 2776.4 W/m^2 already at 200°C. Comparing these values with those reported in Table 4.2, it is possible to notice that higher reaction heats are obtained at lower temperatures. This is due to the higher catalyst density, which is 0.75 g/cm^3 instead of 0.63 g/cm^3.

Fig. 4.18 shows the axial temperature profiles measured on the packed-foam at different temperatures (180-200°C). Limited T-profiles along the catalyst bed are obtained at all the temperatures investigated, thus resulting in very small T-gradients. In this regard, the ΔT_{cat} is negligible at 180 and 190°C ($\Delta T_{cat} \approx 1$ °C), and it reaches values of 2.7 and 3.7°C at 195 and 200°C respectively.

These results are again really close to those obtained in the previous case, confirming the outstanding heat transfer properties of the packed foam reactor configuration. However, during the temperature ramp from 200 to 205°C, a thermal runaway occurs (Fig. 4.19). At a temperature of 205 °C, the reaction heat released would have been around 3578.2 W/m^2, which is a value close to that obtained at around 225 °C with the packed-foam of exp. a. Due to the fact that the major difference between these foams is their surface area (i.e. the length of the foam of exp. (b) is half with respect to that of exp. (a)), this result may indicate that the heat removal is favored in the presence of a bigger solid matrix. The heat transfer seems to be managed not only in correspondence of the catalyst length but also along all the axial direction of the structure.

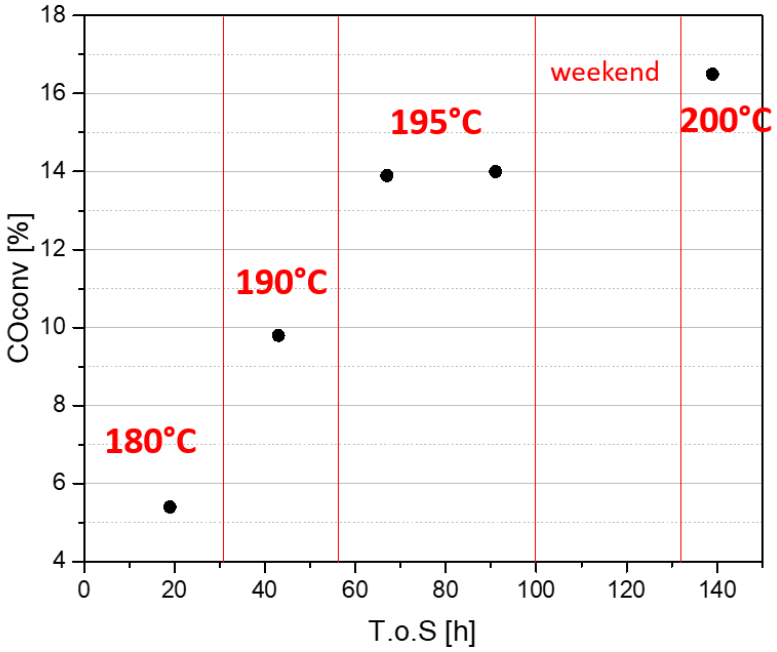

Fig. 4.17: Evolution of the CO conversion with time on stream (T.o.S.) at different temperatures.

P= 25 bar, H_2/CO^{in}= 2 mol/mol, GHSV= 6410 cm^3(STP)/h/g_{cat}, inerts= 24 vol.%.

Table 4.3: Main FTS Products at different temperatures.

P= 25 bar, H_2/CO^{in}= 2 mol/mol, GHSV= 6410 cm^3(STP)/h/g_{cat}, inerts= 24 vol.%.

T.o.S. [h]	T [°C]	X_{CO} [%]	S_{CH4} [%]	S_{CO2} [%]	Q [W/m^2]
19	180	5.4	7.0	0.2	909.7
43	190	9.8	8.7	0.3	1650.7
67	195	13.9	9.6	0.3	2342.7
139	200	16.5	14.0	0.6	2776.4

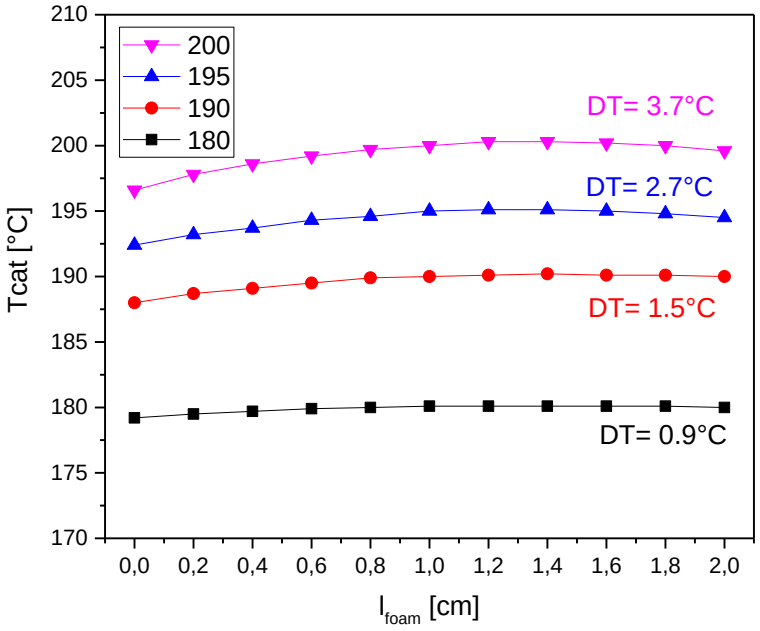

Fig. 4.18: Axial temperature profiles measured at different temperatures (T= 180, 190, 195, 200°C) of the packed foam(b) reactor.

P= 25 bar, H_2/CO^{in}= 2 mol/mol, GHSV= 6410 cm^3(STP)/h/g_{cat}, inerts= 24 vol.%.

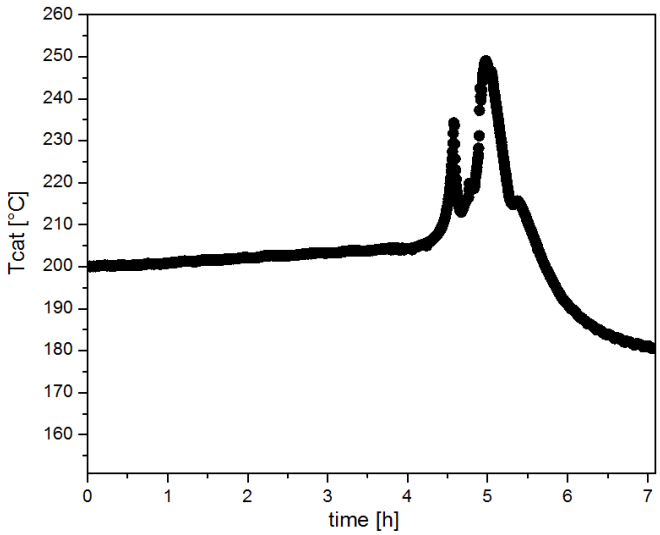

Fig. 4.19: Temperature profile of the catalytic bed during the thermal runaway occurred.

P= 25 bar, H_2/CO^{in}= 2 mol/mol, GHSV= 6410 cm^3(STP)/h/g_{cat}, inerts= 24 vol.%.

4.3.3 Packed-bed reactor

The CO conversion values measured at 180 and 190 °C were the same obtained with the packed-foam reactor. The catalyst performances were recorded only at these low temperatures since a thermal runaway occurred once the catalyst reached 195°C. As shown in Fig. 4.20, in fact, the catalyst temperature becomes unstable even during the temperature ramp from 190 to 195°C, with fluctuations that increase gradually up to the onset of the thermal runaway. These fluctuations are due to the interactions between the reaction kinetics and the PID controller of the adopted oven. More specifically, the reaction system is controlled with a cascade temperature control (Chapter 3), which allows to maintain the temperature of the catalyst (internal TC static in Fig. 4.11c) to the setpoint by regulating the power supplied from the oven. The temperature of the catalyst measured in the packed-foam reactor configuration is flat due to the presence of the highly conductive foam which strongly favors the reaction heat removal (Fig.4.15 and 4.18). On the contrary, in the case of the packed-bed configuration, the temperature of the catalyst oscillates because of the fact the heat removal is only managed by the oven. In line with these observations, the catalyst bed in the packed-bed reactor configuration resulted strongly not isothermal with axial temperature gradients along the catalyst bed (ΔT_{cat}) of 5 °C (at 180 °C) and 9 °C (at 190 °C).

Noteworthy is also the fact that the packed bed reactor works under milder process conditions (the catalyst volumetric density is halved) if compared with the packed-foam reactor.

The comparison with the experiment in the packed foam, therefore, clearly emphasizes the strongly positive effect of the conductive cellular foam structure in effectively controlling the strong exothermicity of the Fischer-Tropsch synthesis in tubular reactors, already at the laboratory scale.

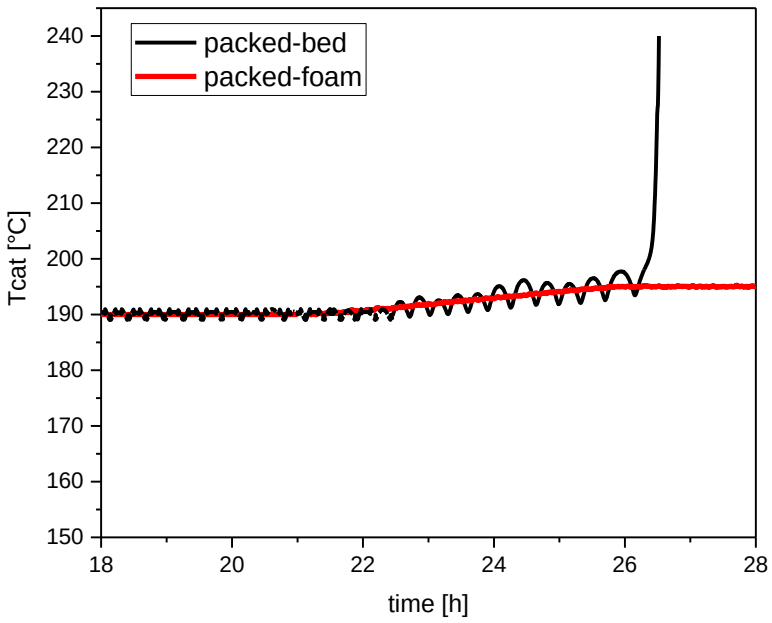

Fig. 4.20: Temperature profiles during the T-ramp from 190 to 195°C of the packed foam (red line) and of the packed-bed reactor (black line).

P= 25 bar, H_2/CO^{in}= 2 mol/mol, GHSV= 6410 cm^3(STP)/h/g_{cat}, inerts= 24 vol.%.

4.3.4 Unloading of the structured catalysts

Catalyst loading and unloading in the tubular reactor are known to be particularly critical in washcoated structured reactor technologies. This is due to the fact that the methods for loading, packing, sealing and unloading structured catalysts in the reactors are different from those well established for randomly packed catalysts, and cannot be directly derived from the experience made in stationary environmental installations [21]. In addition, the possibility of replacing the spent catalyst is infeasible in the washcoated reactors and requires the development of dedicated technologies [21].

With the innovative concept of the packed-foam these problems may be overcome. Indeed, the unloading operations (Fig. 4.21) shows that is possible to completely pull the foam out the reactor and consecutively the catalyst from the foam, thus leading to the possibility of

completely regenerate and replace a new catalyst. Future work would be needed to deepen this aspect.

Fig. 4.21: Foam and spent catalyst removed from the reactor.

4.4 Conclusions

The temperature management is a key challenge for the intensification of the Fischer-Tropsch process in multitubular fixed-bed reactors. In this regard, herein we show for the first time that the adoption of open-cell foams made of a thermally conductive material as reactor internals can be an effective solution to enhance the overall heat transfer performances of packed-bed FTS reactors. Our data confirm that, thanks to the adoption of the conductive foams, the mean temperature inside the reactor can be controlled much better providing new operating windows not accessible using the conventional packed-bed reactor technology. The conductive packed-foams enable in fact running the FT reaction under severe conditions (i.e.

high CO conversion and large reaction heat release) with an intensified temperature control. Indeed, in a crucial comparative experiment using the conventional packed-bed reactor, although it was operated under milder conditions (i.e. the catalyst volumetric density was halved with respect to the foam), thermal runaway occurred already at very low temperatures, i.e. with limited release of reaction heat. These results are a direct indication that the heat exchange is significantly enhanced thanks to the structured conductive substrate of the foam.

In more general terms, highly conductive packed-foams also represent an innovative solution to increase the catalyst inventory in structured tubular reactors, since the catalyst load which can be packed in the open-cell foam is much greater than the amount which can be loaded by washcoating the same foam. In this way, the productivity per reactor volume can be boosted. In addition, "packing" the foam means overcoming all the problems linked to the coating process, to the catalyst loading and unloading in the reactor, and to the replacement of the spent catalyst. Furthermore, the packed-bed configuration allows to exploit the most effective heat transfer mechanism available, i.e. conduction within the highly conductive structured substrate in the bulk of the bed and the local mixing of the packed bed at the boundary between the bed and the tube wall.

Accordingly, the concept of conductive packed foams may provide an effective design strategy in the case of compact tubular reactor units for strongly exothermic processes. The results obtained in this work clearly prove that the adoption of highly conductive packed-foams is an innovative strategy to boost the productivity per reactor volume of the reactions under kinetic control, while granting at the same time enhanced heat transfer performances within the reactor.

Notably, the same concept can also be exploited for lab-scale kinetic studies of strongly exothermic catalytic reactions, as it enables an excellent temperature control even under

severe operating conditions which would not be otherwise accessible, thus extending the range of possible reaction parameters.

4.5 References

[1] M. E. Dry, Catalysis Today 71 (2002) 227–241

[2] L. Fratalocchi, C. G. Visconti, L. Lietti, G. Groppi, E. Tronconi, E. Roccaro, R. Zennaro, Catalysis Science & Technology 6 (2016) 6431-6440

[3] C. G. Visconti, E. Tronconi, G. Groppi, L. Lietti, M. Iovane, S. Rossini, R. Zennaro, Chemical Engineering Journal 171 (2011) 1294-1307

[4] D. Merino, O. Sanz, M. Montes, Chemical Engineering Journal 327 (2017) 1033-1042

[5] S. T. Sie, M. M. G. Senden, H. M. H. Van Wechem, Catalysis Today 8 (1991) 371-394

[6] C. G. Visconti, E. Tronconi, L. Lietti, G. Groppi, P. Forzatti, C. Cristiani, R. Zennaro, S. Rossini, Applied Catalysis A: General 370 (2009) 93-101

[7] L. Fratalocchi, C. G. Visconti, L. Lietti, E. Tronconi, U. Cornaro, S. Rossini, Catalysis Today 246 (2015) 125-132

[8] L. Fratalocchi, C. G. Visconti, L. Lietti, E. Tronconi, S. Rossini, Applied Catalysis A: General 512 (2016) 36-42

[9] L. C. Almeida, F. J. Echave, O. Sanz, M. A. Centeno, G. Arzamendi, L. M. Gandìa, E. F. Sousa-Aguiar, J. A. Odriozola, M. Montes, Chemical Engineering Journal 167 (2011) 536-544

[10] L. C. Almeida, O. Sanz, D. Merino, G. Arzamendi, L. M. Gandìa, M. Montes, Catalysis Today 215 (2013) 103-111

[11] R. Mystrad, S. Eri, P. Pfeifer, E. Rytter, A. Holmen, catalysis Today 147S (2009) S301-S304

[12] M. Sheng, H. Yang, D. R. Cahela, W. R. Yantz Jr., C. F. Gonzales, B. J. Tatarchuck, Applied Catalysis A: General 445-446 (2012) 143-152

[13] M. Sheng, H. Yang, D. R. Cahela, B. J. Tatarchuck, Journal of Catalysis 281 (2011) 254-262

[14] M. Lacroix, L. Dreibine, B. de Tymowski, F. Vigneron, D. Edouard, D. Begin, P. Nguyen, C. Pham, S. Savin-Poncet, F. Luck, M. J. Ledoux, C. Pham-Huu, Applied Catalysis A: General 397 (2011) 62-72

[15] I. Graf, A. K. Ruhl, B. Kraushaar-Czarnetzki, Chemical Engineering Journal 244 (2014) 234-242

[16] N. Hooshyar, D. Vervloet, F. Kapteijn, P.J. Hamersma, R. F. Mudde, J. R. van Ommen, Chemical Engineering Journal 207-208 (2012) 865-870

[17] B. Kaskes, D. Vervloet, F. Kapteijn, J. R. van Ommen, Chemical Engineering Journal 283 (2016) 1465-1483

[18] R. J. Kee, C. Karakaya, H. Zhu, Proceedings of the Combustion Institute 36 (2017) 51-76

[19] M. Iovane, R. Zennaro, P. Forzatti, G. Groppi, L. Lietti, E. Tronconi, C. G. Visconti, S. Rossini, E. Mignone, Pat. Appl. WO/2010/130399

[20] G. Groppi. E. Tronconi, C.G. Visconti, A. Tasso, R. Zennaro, Pat. Appl. WO/2015/033266

[21] C. G. Visconti, G. Groppi, E. Tronconi, Catalysis Today 273 (2016) 178-186

[22] E. Tronconi, G. Groppi, C. G. Visconti, Current Opinion in Chemical Engineering 5 (2014) 55-67

[23] C. Pham-Huu, B. Madani, M. Lacroix, L. Dreibine, M. J. Ledoux, S. Savin-Poncet, J. Bousquet, D. Schweich, Int. Pat. Appl. WO 2007/000506 A1, 2007

[24] G. Zanchi, "Analisi di reattività di catalizzatori Co/γ-Al_2O_3 attivi nella sintesi di Fischer-Tropsch", Tesi Magistrale in Ingegneria Chimica, Politecnico di Milano (2016).

[25] C.G. Visconti, L. Lietti, P. Forzatti, R. Zennaro, Applied Catalysis A: General 330 (2007) 49–56.

[26] B. Todić, V. V. Ordomsky, N. M. Nikačević, A. Y. Khodakovc, D. B. Bukur, Catalysis Science and Technology 5 (2015) 1400-1411

[27] https://www.velocys.com/news/image-library/

Appendix A

Spreadsheet

Response factors

Input:

x_i xi mole fraction of the i-th compound in feed;

A_i area of the i-th compound computed from the gaschromatographic analysis.

The i-th response factor is calculated using CH4 as a reference:

$$f_i^{CH_4} = \frac{x_i \cdot A_{CH_4}}{x_{CH_4} \cdot A_i}$$

Outgoing molar flows

Input:

A_i area of the i-th compound computed from the gaschromatographic analysis;

F_{Ar}^{in} incoming flow of Ar, equal to the outgoing one (in Nl / h);

w_{CH3CN} weight of acetonotrile added to the analyzed aqueous phase sample (in grams), multiplied by the weight ratio between the amount of aqueous phase collected and the quantity analyzed;

w_{org} weight of the collected organic phase sample (in grams);

w_{cere} weight of the collected wax sample (in grams).

For the gas phases, the outgoing flow of the i-th compound is calculated differently for the various analyzes:

- molecular sieve column: using Ar as an internal standard

$$F_i^{out} = \frac{A_i \cdot f_i^{CH_4}}{A_{Ar} \cdot f_{Ar}^{CH_4}} \cdot f_{Ar}^{in} \quad [\text{Nl/h}]$$

- porapack column: using the CH_4 area measured in the analysis itself as an internal standard, note the flow of CH_4 coming out from the analysis of the gaseous products, using the molecular sieve column

$$F_i^{out} = \frac{A_i \cdot f_i^{CH_4}}{A_{CH_4} \cdot f_{CH_4}^{CH_4}} \cdot f_{CH_4}^{in} \quad [\text{Nl/h}]$$

- capillary column: using the CH_4 area measured in the analysis itself as an internal standard, note the flow of CH_4 coming out from the analysis of the gaseous products, using the molecular sieve column

$$F_i^{out} = \frac{A_i \cdot f_i^{CH_4}}{A_{CH_4} \cdot f_{CH_4}^{CH_4}} \cdot f_{CH_4}^{out} \quad [\text{Nl/h}]$$

Also for the condensed phases, the weight of i-th compound is calculated differently for the various analyzes:

- aqueous phase: using the weight of CH_3CN added to the sample as an internal standard

$$w_i^{out} = \frac{A_i \cdot f_i}{A_{CH_3CN} \cdot f_{CH_3CN}} \cdot w_{CH_3CN} \quad [\text{g}]$$

- organic: using the weight of the organic phase collected during the test

$$w_i^{out} = \frac{A_i \cdot f_i}{\sum_i^{org} A_i \cdot f_i} \cdot w_{org} \quad [\text{g}]$$

- waxes: using the weight of the waxes collected during the test

$$w_i^{out} = \frac{A_i \cdot f_i}{\sum_i^{wax} A_i \cdot f_i} \cdot w_{wax} \quad [\text{g}]$$

The data thus calculated are converted in terms of molar flow rates (mol / h) through the molecular weight of the i-th compounds and of the duration of the daily test.

CO conversion

The CO conversion is calculated from the incoming and outgoing molar flow rates of CO:

$$X_{CO} = (1 - \frac{n_{CO}^{in}}{n_{CO}^{out}}) \cdot 100 \quad [\%]$$

Carbon balance

The carbon balance is calculated from the ratio of the sum of the C atoms of all the i-th species produced and those converted (coming from the atomic balances):

$$Cbalance = \frac{\sum_i n_i^{C_{prod}}}{\sum_i n_i^{C_{conv}}}$$

Specific Productivity

The productivity of each species is calculated from its outgoing molar flow, its molecular weight and the weight of catalyst loaded into the reactor:

$$\hat{W}_i = \frac{n_i^{out} \cdot PM_i \cdot 10^6}{w_{cat}} \quad [\mu g/h/g_{cat}]$$

Selectivity

The selectivity of the system towards each individual species is calculated by the C produced by the reaction for the same species (in mol / h), calculated from the atomic balances on the single species:

$$S_i = \frac{C_i^{prod}}{\sum_i C_i^{Prod}} \cdot 100 \quad [\%]$$

ASF distribution of reaction products

The ASF distribution of products, depending on the number of carbon atoms of the individual species, can be calculated both in terms of selectivity and productivity. For the i-th species:

$$ASF_i^{SEL} = \ln(\frac{S_i \div 100}{n_i})$$

$$ASF_i^{PROD} = \ln(\frac{W_i \div 100}{n_i})$$

It is possible to evaluate the slope m of the line that interpolates the points of the distribution of C_{15+} products; note this, it is easy to calculate the alpha parameter (probability of growth) related to the specific distribution: α= exp(m).

Appendix B

FBR Polimi plant P&I

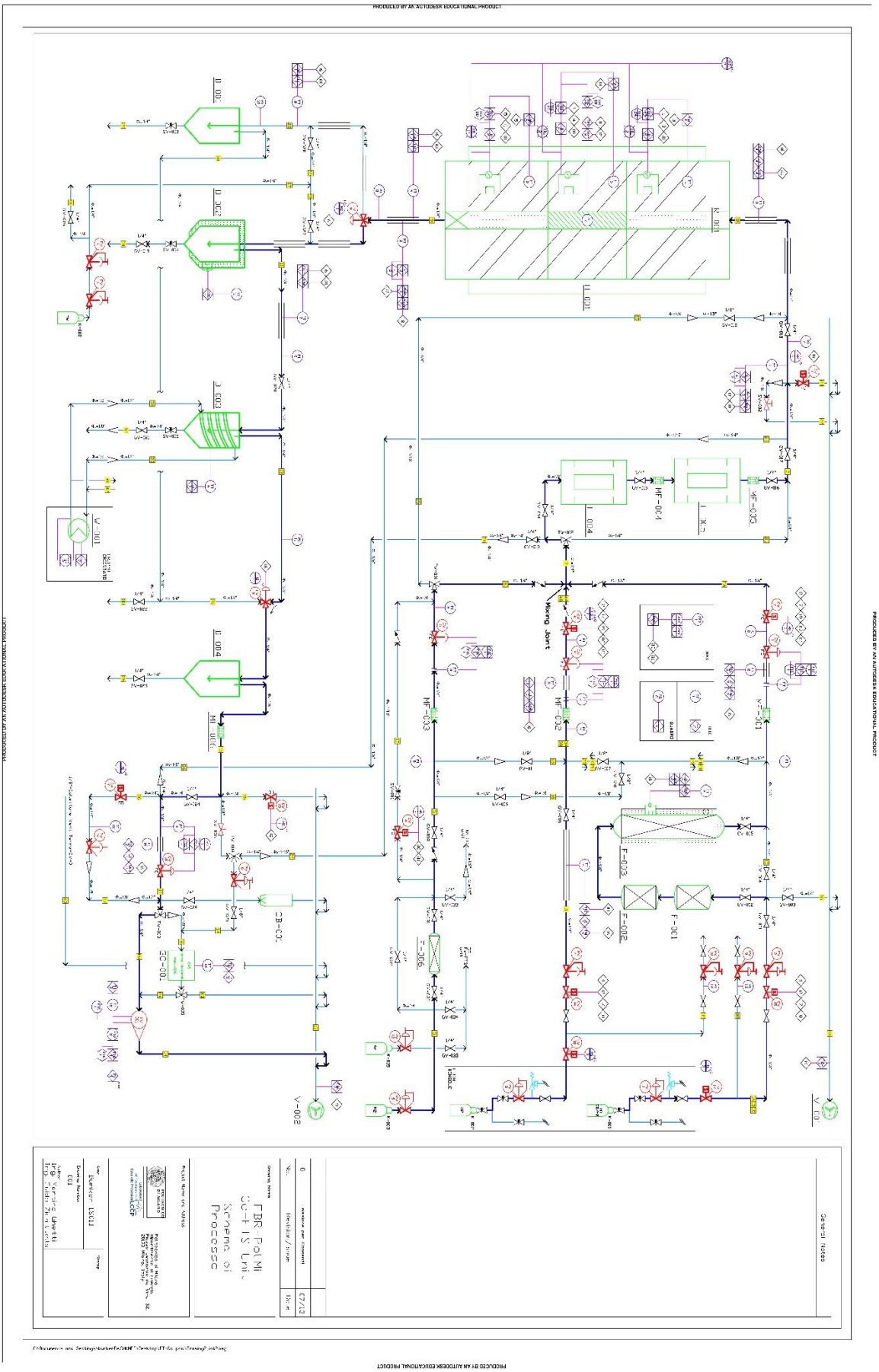
PRODUCED BY AN AUTODESK EDUCATIONAL PRODUCT
Mixing Joint
FBR PoliMi
CO-HTS Unit
Scheme of
Process

Appendix C

National Instrument LabVIEW: front panel

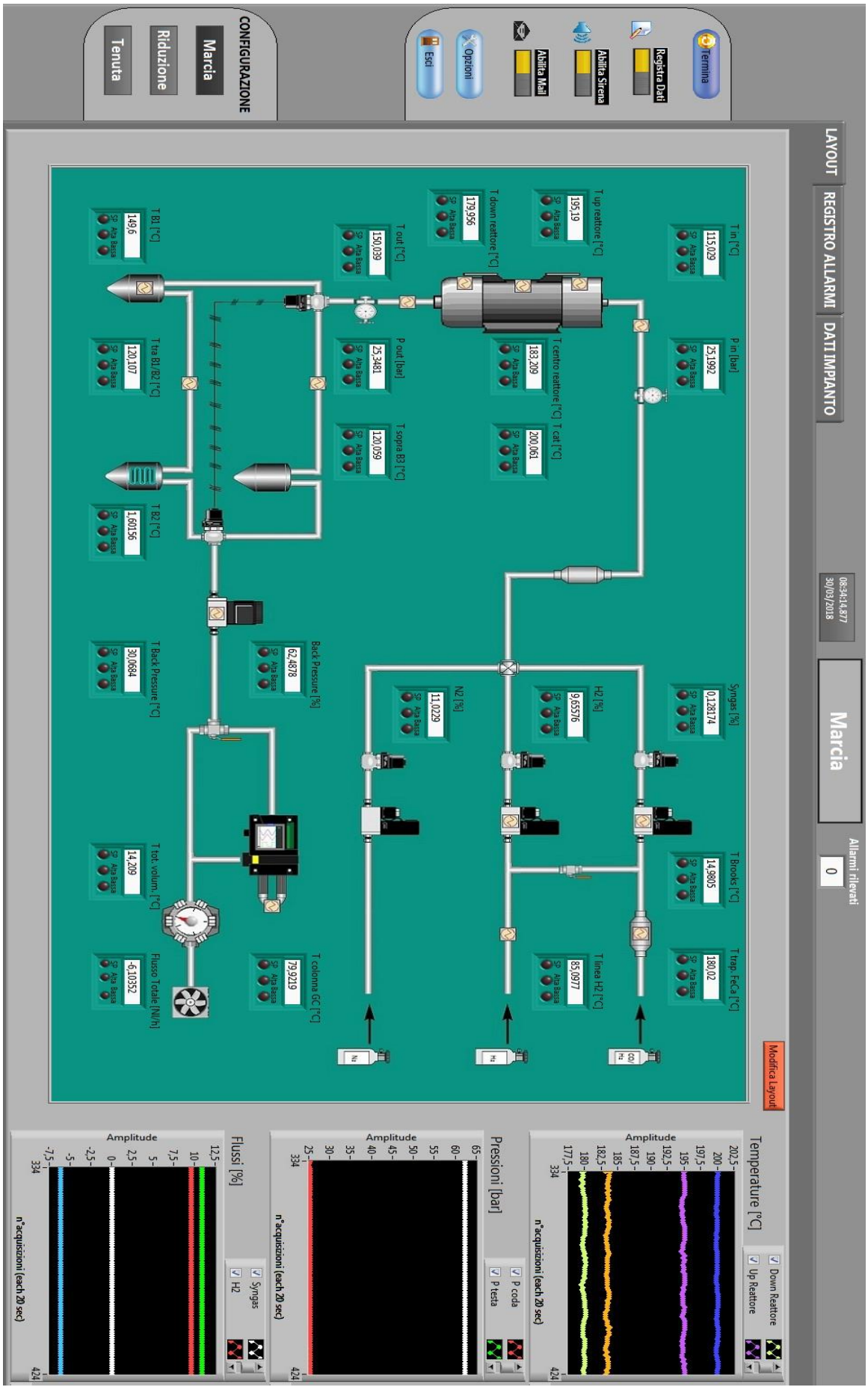
LAYOUT
REGISTRO ALLARMI
DATI IMPIANTO
08:34:14.877
30/03/2018
Marcia
Allarmi rilevati
0
Termina
Registra Dati
Abilita Sirena
Abilita Mail
Opzioni
Esci
CONFIGURAZIONE
Marcia
Riduzione
Tenuta
Modifica Layout
T in [°C]
115,029
P in [bar]
25,1992
T up reattore [°C]
195,19
T down reattore [°C]
179,956
T centro reattore [°C]
183,209
T cat [°C]
200,061
T out [°C]
150,039
P out [bar]
25,3481
T sopra B3 [°C]
120,059
T B1 [°C]
149,6
T tra B1-B2 [°C]
120,107
T B2 [°C]
1,60156
Syngas [%]
0,128174
H2 [%]
9,65576
N2 [%]
11,0229
T Brooks [°C]
14,9805
T trap. FeCa [°C]
180,02
T linea H2 [°C]
85,0977
T colonna GC [°C]
79,9219
Back Pressure [%]
62,4878
T Back Pressure [°C]
30,0684
T tot. volum. [°C]
14,209
Flusso Totale [Nl/h]
-6,10352
Temperature [°C]
Down Reattore
Up Reattore
Amplitude
n°acquisizioni (each 20 sec)
Pressioni [bar]
P coda
P testa
Flussi [%]
Syngas
H2